

NASA Contractor Report 3084

NASA
CR
3084
c.1

LOAN COPY: RETURN
AFWL TECHNICAL LIB
KIRTLAND AFB, NM

TECH LIBRARY KAFB, NM
0061888

Studies of Vorticity Imbalance
and Stability, Moisture Budget,
Atmospheric Energetics, and
Gradients of Meteorological
Parameters During AVE III

CONTRACT NAS8-31773
DECEMBER 1978

NASA



0061888

NASA Contractor Report 3084

Studies of Vorticity Imbalance and Stability, Moisture Budget, Atmospheric Energetics, and Gradients of Meteorological Parameters During AVE III

Prepared for
George C. Marshall Space Flight Center
under Contract NAS8-31773



National Aeronautics
and Space Administration

**Scientific and Technical
Information Office**

1978

FOREWORD

This report is one of several to be published from research conducted under NASA Contract NAS8-31773 entitled, "Relationships Between Severe Storms and Their Environment." Several of these studies are referenced in this report. This effort is sponsored by the NASA Office of Applications under the direction of Marshall Space Flight Center's Atmospheric Sciences Division. The results presented in this report represent only a portion of the total research effort.

Since 1964, NASA has conducted nine Atmospheric Variability Experiments. An overall goal of the AVE program is to investigate the temporal and spatial variability of atmospheric parameters associated with synoptic and mesoscale systems normally indicated using data available at 12-h intervals. Of particular interest in many of the AVE experiments has been the determination of the interrelationships between convective storms and their synoptic-scale environment. Extensive diagnostic analyses of AVE II and AVE IV have produced results which further the understanding of these "scale interaction" processes between synoptic, mesoscale, and convective-scale systems. Since the analysis of each AVE only represents a single case study, a compilation of results from many experiments, under varying conditions, is needed to establish general relationships about the atmosphere.

This report contains four diagnostic studies of AVE III. AVE III represents a high wind speed wintertime situation, while most AVE's analyzed previously represented springtime conditions with rather low wind speeds. The general areas of analysis include the examination of budgets of vorticity, moisture, kinetic energy, and potential energy, and a synoptic and statistical study of the horizontal gradients of meteorological parameters. Conclusions are integrated with and compared to those obtained in previously analyzed experiments (mostly springtime weather situations) so as to establish a more definitive understanding of the structure and dynamics of the atmosphere under a wide range of synoptic conditions.

AUTHORS' ACKNOWLEDGMENTS

The authors express their appreciation to the many students who participated in the analysis of the data and preparation of this report. We especially thank Ms. Karen Cobbs for typing the manuscript, Ms. Doreen Westwood for preparation of most of the figures, and Mr. Kelly Hill of NASA for his encouragement and advice.

The authors gratefully acknowledge support provided under NASA Contract No. NAS8-31773. This contract is under the auspices of the Atmospheric Sciences Division, Space Sciences Laboratory, National Aeronautics and Space Administration, Marshall Space Flight Center, Alabama.

TABLE OF CONTENTS

	<u>Page</u>
FOREWORD	ii
ACKNOWLEDGMENTS	iii
TABLE OF CONTENTS	iv
LIST OF TABLES	viii
LIST OF FIGURES	ix
ABSTRACT (Chapter 1)	1
1.1 AVE III Data	2
1.1.1 <u>Rawinsonde data</u>	2
1.1.2 <u>Surface data</u>	4
1.1.3 <u>Digital radar data</u>	4
1.2 General Analytical Procedures	6
1.2.1 <u>Objective analysis and smoothing</u>	6
1.2.2 <u>Numerical evaluation of equations</u>	8
1.2.3 <u>Computation of vertical motion</u>	8
1.3 Synoptic Conditions in AVE III	9
1.4 References	12
ABSTRACT (Chapter 2)	14
2.1 Introduction	15
2.2 Analytical Methods	15
2.2.1 <u>Vorticity equation</u>	15
2.2.1.1 <u>Computational procedures</u>	16
2.2.1.2 <u>Method of presentation of results</u>	16
2.2.2 Stability	17
2.2.2.1 <u>Computational procedure</u>	17
2.2.2.2 <u>Method of presentation of results</u>	18

TABLE OF CONTENTS (CONTINUED)

	<u>Page</u>
2.2.3 <u>Thunderstorm potential indices</u>	18
2.2.3.1 <u>Rationale</u>	18
2.2.3.2 <u>Definitions</u>	19
2.2.3.3 <u>Method of presentation of results</u>	20
2.3 Results	21
2.3.1 <u>Average profiles</u>	21
2.3.1.1 <u>Stability</u>	21
2.3.1.2 <u>Vorticity budget</u>	21
2.3.2 <u>Thunderstorm potential indices</u>	29
2.3.3 <u>Apparent relationship of residual to the jet stream</u> . .	33
2.4 Conclusions	35
2.5 References	35
ABSTRACT (Chapter 3)	37
3.1 Introduction	38
3.2 Analytical Methods	38
3.2.1 <u>The moisture budget equations</u>	38
3.2.2 <u>Local changes</u>	40
3.2.3 <u>Vertical changes</u>	40
3.2.4 <u>Horizontal changes</u>	41
3.3 Results	42
3.3.1 <u>AVE III</u>	42
3.3.1.1 <u>Local changes</u>	45
3.3.1.2 <u>Vertical moisture divergence</u>	45
3.3.1.3 <u>Horizontal moisture divergence</u>	48
3.3.1.4 <u>Residual of moisture</u>	50
3.3.2 <u>Comparisons between AVE III and AVE IV</u>	52

TABLE OF CONTENTS (CONTINUED)

	<u>Page</u>
3.4 Conclusions	55
3.5 References	55
ABSTRACT (Chapter 4)	56
4.1 Introduction	57
4.2 Energy Equations	57
4.3 Analytical Procedures	59
4.4 Results	59
4.4.1 <u>Composite kinetic energy budget</u>	59
4.4.2 <u>Composite internal and potential energy budget</u>	63
4.4.3 <u>Time series profiles</u>	65
4.4.3.1 <u>Kinetic energy</u>	65
4.4.3.2 <u>Internal and potential energy</u>	72
4.4.4 <u>Energy budgets versus precipitation intensity</u>	77
4.5 Conclusions	83
4.6 References	87
ABSTRACT (Chapter 5)	89
5.1 Introduction	90
5.2 Analytical Procedures	90
5.2.1 <u>Stratification of data</u>	90
5.2.2 <u>Gradients</u>	92
5.2.3 <u>Statistical parameters</u>	92
5.3 Results for AVE III	94
5.3.1 <u>Convective versus nonconvective areas</u>	94
5.3.2 <u>Probability of magnitudes of gradients</u>	96
5.3.3 <u>Magnitudes of gradients in the vicinity of convection</u>	96
5.4 Comparison of AVE II, AVE III, and AVE IV	106

TABLE OF CONTENTS (CONTINUED)

	<u>Page</u>
5.4.1 <u>Convective and nonconvective areas</u>	106
5.4.2 <u>Magnitudes of gradients in the vicinity of convection</u> .	107
5.5 Magnitudes of Gradients versus Distance for AVE and HIPLEX Data	108
5.6 Summary and Conclusions	116
5.7 References	118
APPENDIX	119

LIST OF TABLES

<u>Table</u>		<u>Page</u>
1-1	RMS errors of thermodynamic quantities for the AVE III data	3
1-2	RMS errors of baroswitch contact wind data for the AVE IV data at elevation angles of 40° and 20°	3
1-3	Manually digitized radar (MDR) data code (Foster and Reap, 1973)	6
4-1	Average kinetic energy budget for the entire AVE III experiment. The AVE area is $49.0 \times 10^{11} \text{ m}^2$. All nine observation times are included	60
4-2	The average AVE III kinetic energy budget compared with previous results	62
4-3	Average combined internal and potential energy budget for the entire AVE III experiment. The AVE area is $49.0 \times$ 10^{11} m^2 . All nine observation times are included	64
4-4	Kinetic energy budget for the 48 grid points with MDR values between 4 and 9	81
4-5	Combined internal and potential energy budget for the 48 grid points with MDR values between 4 and 9	86
5-1	Selected statistical parameters of gradients in convective and nonconvective areas of AVE III	95
5-2	Means of gradients in AVE III over areas in which the status of convection changed	99

LIST OF FIGURES

<u>Figure</u>		<u>Page</u>
1-1	Rawinsonde stations participating in the AVE III experiment	2
1-2	Locations of surface stations for the AVE III area . . .	4
1-3	Manually Digitized Radar (MDR) grid network	5
1-4	Grid used for numerical computations	7
1-5	Synoptic conditions at 0000 GMT 6 February 1975	10
1-6	Synoptic conditions at 1200 GMT 7 February 1975	11
2-1	Averages of convective instability ($10^{-3}^{\circ}\text{C mb}^{-1}$) as function of MDR values	22
2-2	Averages of convective instability ($10^{-3}^{\circ}\text{C mb}^{-1}$) with time lags in MDR	22
2-3	Average profiles for the local derivative of vorticity	23
2-4	Average profiles of horizontal vorticity advection . . .	23
2-5	Average profiles of the divergence term	24
2-6	Average profiles of the residual	25
2-7	Average profiles of the local derivative of vorticity for time lags in MDR of 3 and 6 hours	26
2-8	Average profiles of horizontal vorticity advection for time lags in MDR of 3 and 6 hours	27
2-9	Average profiles of the divergence term for time lags in MDR of 3 and 6 hours	28
2-10	Average profiles of the residual for time lags in MDR of 3 and 6 hours	30
2-11	Analyzed fields of thunderstorm indices for 0000 GMT on 6 February 1975. (See Appendix for MDR data and thunderstorm location)	31
2-12	The residual term at 300 mb (10^{-9} s^{-2}) at (a) 0000 GMT and (b) 0600 GMT 6 February 1975 (see Appendix for MDR data)	34
3-1	Synoptic charts for 1800 GMT, 6 February 1975	43

LIST OF FIGURES (CONTINUED)

<u>Figure</u>		<u>Page</u>
3-2	Three-hour composite of MDR data at 1800 GMT on 6 February 1975	44
3-3	Vertical profiles of the local rate-of-change of moisture ($10^{-6} \text{ g cm}^{-2} \text{ s}^{-1}$) as function of MDR values . . .	45
3-4	Vertical profiles of vertical moisture divergence ($10^{-6} \text{ g cm}^{-2} \text{ s}^{-1}$) as function of MDR values	46
3-5	Analyses of vertical moisture divergence at 1800 GMT on 6 February 1975 ($10^{-6} \text{ g cm}^{-2} \text{ s}^{-1}$) within two layers .	47
3-6	Vertical profiles of horizontal moisture divergence ($10^{-6} \text{ g cm}^{-2} \text{ s}^{-1}$) as function of MDR values	48
3-7	Vertical profiles of moisture concentration due to wind divergence ($10^{-6} \text{ g cm}^{-2} \text{ s}^{-1}$) as function of MDR values .	49
3-8	Vertical profiles of moisture advection ($10^{-6} \text{ g cm}^{-2} \text{ s}^{-1}$) as function of MDR values	49
3-9	Analyses of horizontal moisture divergence at 1800 GMT on 6 February 1975 ($10^{-6} \text{ g cm}^{-2} \text{ s}^{-1}$)	51
3-10	Vertical profiles of the residual of moisture (10^{-6} g $\text{cm}^{-2} \text{ s}^{-1}$) as function of MDR values	52
3-11	Analysis of the residual of moisture in the layer from 900-450 mb at 1800 GMT on 6 February 1975 ($10^{-6} \text{ g cm}^{-2}$ s^{-1})	53
3-12	Three-hour composite of precipitation flux at 1800 GMT on 6 February 1975 obtained from rainfall rates ($10^{-6} \text{ g cm}^{-2} \text{ s}^{-1}$)	53
4-1	Time series of kinetic energy in AVE III	66
4-2	Time series of generation of kinetic energy in AVE III .	67
4-3	Time series of horizontal flux divergence of kinetic energy in AVE III	68
4-4	Time series of vertical flux divergence of kinetic energy in AVE III	69
4-5	Time series of dissipation of kinetic energy in AVE III .	70
4-6	Time series of the ratio between horizontal flux divergence of kinetic energy, dissipation of kinetic energy, and the local change of kinetic energy to the cross-contour generation of kinetic energy in the surface- to 100-mb layer	71

LIST OF FIGURES (CONTINUED)

<u>Figure</u>		<u>Page</u>
4-7	Time series of production of internal energy by diabatic effects in AVE III	73
4-8	Time series of the sum of horizontal flux divergence of internal energy and potential energy in AVE III . .	74
4-9	Time series of the sum of vertical flux divergence of internal energy and potential energy in AVE III . .	75
4-10	Time series of the pressure work term in AVE III . . .	76
4-11	Time series of the sum of the local change of internal and potential energy in AVE III	78
4-12	Vertical profiles of generation of kinetic energy for various ranges of MDR values in AVE III	79
4-13	Vertical profiles of horizontal flux divergence of kinetic energy for various ranges of MDR values in AVE III	79
4-14	Vertical profiles of vertical flux divergence of kinetic energy for various ranges of MDR values in AVE III	80
4-15	Vertical profiles of dissipation of kinetic energy for various ranges of MDR values in AVE III	82
4-16	Time series of creation of internal energy by diabatic effects in AVE III	84
4-17	Vertical profiles of the sum of horizontal flux divergence of internal energy and potential energy in AVE III	84
4-18	Vertical profiles of the sum of vertical flux divergence of internal energy and potential energy in AVE III	85
5-1	Boundaries encompassing grid points at which gradients over 315, 630, and 944 km were computed	93
5-2	Cumulative frequency distributions of geopotential height gradients	97
5-3	Cumulative frequency distributions of temperature gradients	97

LIST OF FIGURES (CONTINUED)

<u>Figure</u>		<u>Page</u>
5-4	Cumulative frequency distributions of wind speed gradients	98
5-5	Cumulative frequency distributions of mixing ratio gradients	98
5-6	Composite manually digitized radar (MDR) chart for 2100 GMT, 6 February 1975	101
5-7	Geopotential height gradient fields [$m(315\text{ km})^{-1}$] at 2100 GMT 6 February 1975	102
5-8	Temperature gradient fields [$^{\circ}C(315\text{ km})^{-1}$] at 2100 GMT 6 February 1975	103
5-9	Wind speed gradient fields [$m\text{ s}^{-1}(315\text{ km})^{-1}$] at 2100 GMT 6 February 1975	104
5-10	Mixing ratio gradient fields [$g\text{ kg}^{-1}(315\text{ km})^{-1}$] at 2100 GMT 6 February 1975.. . . .	105
5-11	Plots of selected percentile values of height gradient versus distance for different pressure levels	110
5-12	Plots of temperature gradient values versus distance for different levels	112
5-13	Plots of wind speed gradient values versus distance for different levels	114
5-14	Plots of mixing ratio gradient values versus distance for different levels	117

AVE III DATA, GENERAL ANALYTICAL PROCEDURES,
AND SYNOPTIC CONDITIONS

by

Gregory S. Wilson
Department of Meteorology
Texas A&M University
College Station, Texas 77843

ABSTRACT

This chapter contains a discussion of the AVE III data, procedures used to grid basic data, compute vertical motion, and numerically evaluate equations, and a description of synoptic conditions for AVE III.

The AVE III data are discussed in regard to station locations and approximate RMS errors. Other data considered include NWS surface data and Manually Digitized Radar (MDR) data.

The information presented in this chapter is common to the studies presented in Chapters 2-5.

CHAPTER 1. AVE III DATA, GENERAL ANALYTICAL PROCEDURES,
AND SYNOPTIC CONDITIONS

1.1 AVE III Data

1.1.1 Rawinsonde data

The forty-two rawinsonde stations participating in the AVE III experiment are shown in Fig. 1-1. Soundings were taken at nine times: 6 February at 0000 GMT, 0600 GMT, 1200 GMT, 1500 GMT, 1800 GMT, and 2100 GMT, and on 7 February at 0000 GMT, 0600 GMT, and 1200 GMT, 1975.

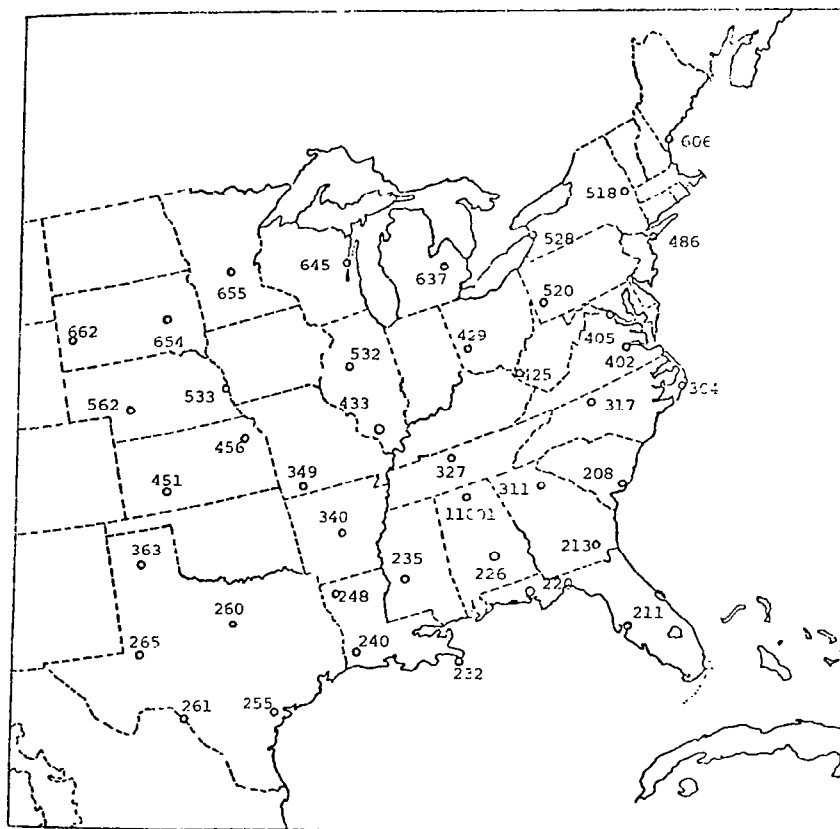


Fig. 1-1. Rawinsonde stations participating in the AVE III experiment.

Data reduction procedures used to process the AVE III rawinsonde data were designed to obtain the most accurate results possible (Fuelberg, 1974). The raw angle and ordinate data were checked for errors prior to calculating the soundings, and computed soundings then were rechecked with corrections made as required. Data were given at 25-mb intervals by Fuelberg and Turner (1975). Estimates of RMS errors of the thermodynamic quantities are given in Table 1-1 (Scoggins and Smith, 1973; Fuelberg, 1974). Recent studies have indicated that errors in the thermodynamic quantities may be even smaller than those given in Table 1-1 (Lenhard, 1973; Brousaides, 1975).

Table 1-1. RMS errors of thermodynamic quantities for the AVE III data.

Parameter	Approximate RMS error
Temperature	1°C or less
Pressure	1.3 mb surface to 400 mb 1.1 mb between 400 and 100 mb 0.7 mb between 100 and 10 mb
Humidity	10%
Pressure Altitude	10 gpm at 500 mb 20 gpm at 300 mb 50 gpm at 50 mb

An error analysis conducted by Fuelberg (1974) gave RMS errors of scalar wind speed and wind direction for the AVE III baroswitch contact data. Table 1-2 presents these RMS errors for elevation angles of 40° and 20°. RMS errors for the smoothed 25-mb data that were used in this study would be somewhat smaller.

Table 1-2. RMS errors of baroswitch contact wind data for the AVE IV data at elevation angles of 40° and 20°.

Level	Elevation Angle		Elevation Angle	
	40°	20°	40°	20°
	RMS Direction Error		RMS Speed Error	
700 mb	1.8°	3.8°	0.5 m s ⁻¹	1.0 m s ⁻¹
500 mb	2.5°	5.6°	0.8 m s ⁻¹	2.0 m s ⁻¹
300 mb	3.1°	7.5°	1.0 m s ⁻¹	3.8 m s ⁻¹
100 mb	6.2°	15.0°	2.0 m s ⁻¹	5.7 m s ⁻¹

Original strip charts from all rawinsonde soundings were checked carefully to determine if sondes entered thunderstorm updrafts or downdrafts. Under these conditions, soundings were removed from the original data set because the sondes apparently had entered violent updrafts. The potential for distorted results due to nonhydrostatic accelerations was thereby considerably reduced.

1.1.2 Surface data

All available surface data for the AVE III experiment were obtained from the National Climatic Center. Figure 1-2 shows locations of the 310 surface stations used. Vector wind, temperature, dew point temperature, and surface pressure were read, keypunched, and checked carefully for errors.



Fig. 1-2. Locations of surface stations for the AVE III area.

Hourly precipitation data were also obtained for the AVE III time period from the National Climatic Center. These data consisted of nearly 2000 raingage reports and were used in the precipitation analysis.

1.1.3 Digital radar data

Manually Digitized Radar (MDR) data were obtained from NOAA's Techniques Development Laboratory to determine accurately the intensity and position of the radar-observed convection during the AVE III experiment. The MDR grid network is shown in Fig. 1-3. MDR data are coded with a single digit from 0 to 9 to indicate areal coverage and echo intensity within blocks that are approximately 83 km on a side. Table 1-3 is an explanation of the MDR code given by Foster and Reap (1973).

Plots of the MDR data were made each hour for 3-h periods centered on each of the nine rawinsonde observation times. The three plots were then

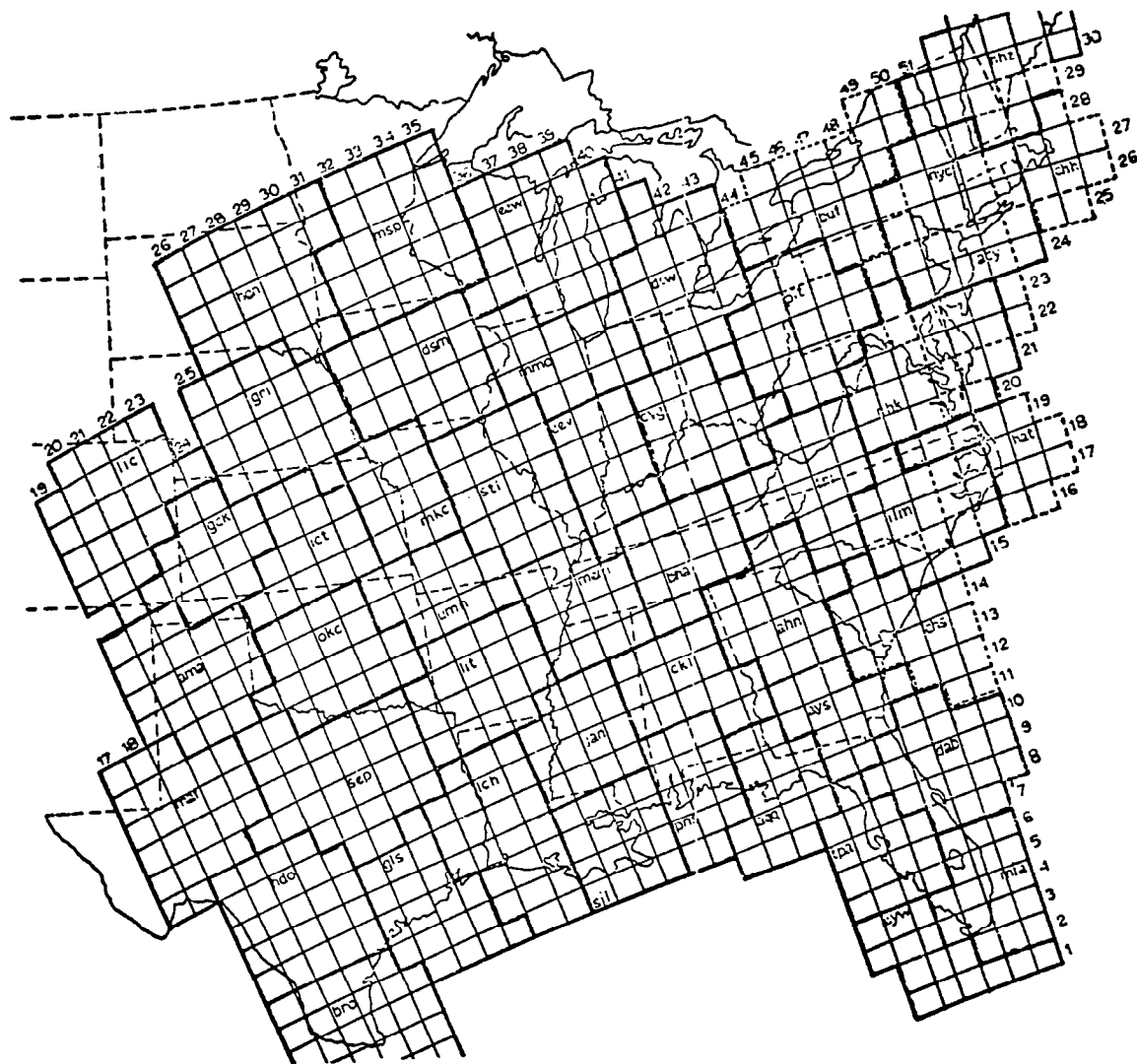


Fig. 1-3. Manually Digitized Radar (MDR) grid network.

Table 1-3. Manually digitized radar (MDR) data code (Foster and Reap, 1973).

Code No.	Maximum Observed VIP ¹ Values	Coverage In Box	Maximum Rainfall Rate (in h ⁻¹)	Intensity Category
0	No Echoes			
1	1	Any VIP1	<0.1	Weak
2	2	≤ 50% of VIP2	0.1-0.5	Moderate
3	2	> 50% of VIP2	0.5-1.0	Moderate
4	3	≤ 50% of VIP3	1.0-2.0	Strong
5	3	> 50% of VIP3	1.0-2.0	Strong
6	4	≤ 50% of VIP3 and 4	1.0-2.0	Very Strong
7	4	> 50% of VIP3, and 4	1.0-2.0	Very Strong
8	5 or 6	≤ 50% of VIP3, 4, 5, and 6	>2.0	Intense or Extreme
9	5 or 6	> 50% of VIP3, 4, 5, and 6	>2.0	Intense or Extreme

¹Video Integrator Processor

combined into a single chart for each of the nine times by using the highest coded value reported for each block (see Appendix for AVE III composite MDR charts).

1.2 General Analytical Procedures

Analytical procedures can determine the success or failure of an experiment and, therefore, must be considered carefully. This section outlines the procedures that were judged most advantageous for these studies.

1.2.1 Objective analysis and smoothing

The diagnostic analyses performed in AVE III are simplified if data are interpolated from randomly-spaced rawinsonde stations to equally-spaced grid points. The grid network used (Fig. 1-4) is centered over the AVE III data area and has a spacing of 158 km. Barr *et al.* (1971) have shown theoretically that a 169-km grid interval incorporates as much detail as is justified from the rawinsonde network over the United States.

Human analysis of data is still preferable to any objective scheme that has been devised, but the number of analyses required rendered hand

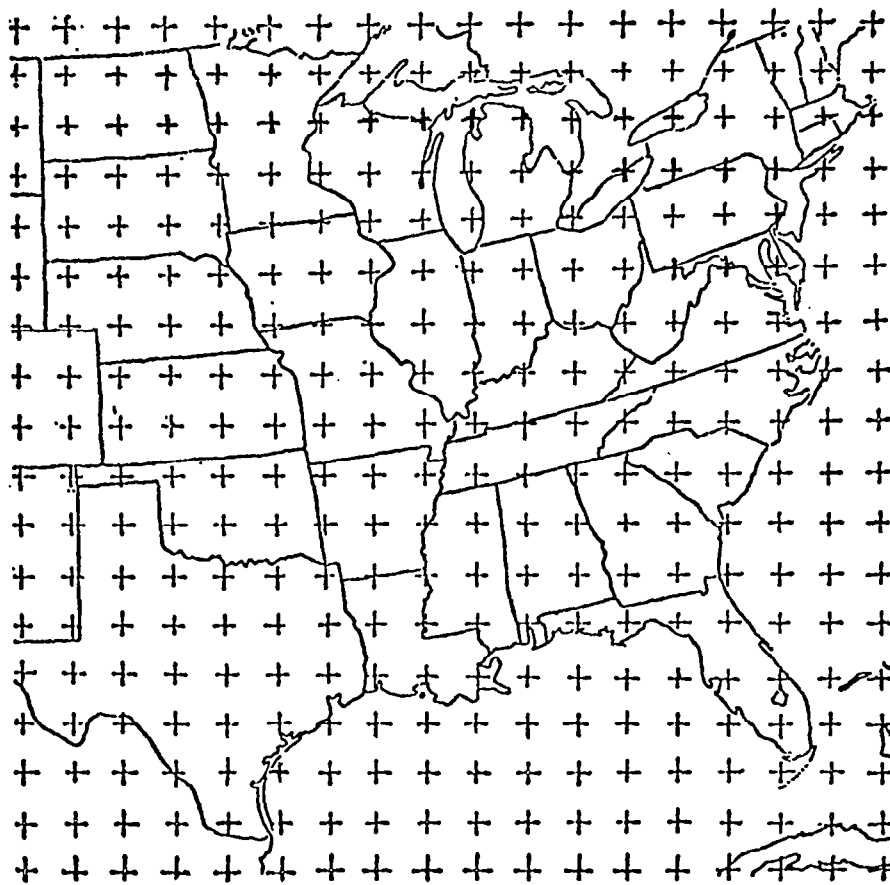


Fig. 1-4. Grid used for numerical computations.

analysis unfeasible for these studies. There were several considerations in the choice of an objective analysis and smoothing procedure from the several that are described in the literature. Such a procedure should interpolate data accurately from stations to the grid without creating fictitious waves or destroying real waves present in the data. Also, the desired results of the procedure should be considered carefully with respect to the input data density. Since the average spacing of rawinsonde stations over the eastern United States is about 350 km, features with wavelengths shorter than 1400 km can seldom be described completely by any objective analysis using this input data.

An objective analysis scheme by Barnes (1964) was used in these investigations. The procedure is commonly referred to as successive corrections to a first-guess field. Data from each rawinsonde station were allowed to influence grid points within a scan radius of three grid distances while four iterations were allowed.

To suppress small waves which cannot be tracked consistently, as well as those which might arise due to the analysis scheme and random errors,

a light nine-point filter by Shuman (1957) was applied to the analyzed fields. The final result retained approximately 90% of the amplitudes of wavelengths of 1400 km, and appeared to contain as much detail as could be justified from the input data based upon good agreement with hand analyses.

The surface data were analyzed using a scan radius of two grid units with four iterations. This produced smooth fields from the high density surface data that meshed with the larger-scale rawinsonde data.

Gridded analyses of height, temperature, wind components, and moisture content were produced at 18 levels, i.e., the surface and at 50-mb intervals from 900 mb to 100 mb, for each of the nine time periods. Winds at the 18 levels were averaged over 50 mb to reduce further random errors. These gridded values were stored on a computer disk and formed the working data set for all phases of each of the studies.

1.2.2 Numerical evaluation of equations

Centered finite differences were used in each study to compute horizontal and vertical derivatives except those at the surface where forward differences were used and at 100 mb where backward differences were used. Time derivatives also were evaluated using centered differences where possible, but forward differences at the first period and backward differences at the last period were required. Numerical evaluations were performed on the Amdahl 470V/6 computer at Texas A&M University.

1.2.3 Computation of vertical motion

Large-scale vertical motion cannot be measured directly, and no method currently available for determining vertical motion is completely accurate. The kinematic method was used in this research because it involved the least stringent assumptions and produced good results. Details of the procedures used are given by Wilson and Scoggins (1976) and Wilson (1976). Terrain-induced vertical motion was included, and a correction scheme by O'Brien (1970) was applied so the values of vertical motion at 100 mb would equal the values obtained by the adiabatic method. The adjustment factor significantly affects vertical motion in levels above about 500 mb. Application of an adjustment factor is necessary because the accuracy of wind data and resulting divergence calculations decrease with altitude. Adiabatic values at 100 mb were chosen because they are obtained independently of kinematic values and are more realistic than an assumption of zero at each grid point.

The kinematic method has been used widely in previous research. Vincent et al. (1976) suggested that it is better than the quasi-geostrophic form of the omega equation. Further support for the kinematic method has been given by such investigators as Chien and Smith (1973), Smith (1971), Fankhauser (1969), and Kung (1973). Moreover, Wilson (1976) indicated that values of kinematic vertical velocity related better to areal coverage and intensity of precipitation during the AVE IV experiment than did values of adiabatic vertical velocity.

1.3 Synoptic Conditions in AVE III

Two frontal systems were present in the AVE III area at the beginning of the experiment, 0000 GMT 6 February 1975 (Fig. 1-5). A warm front extending across Georgia and a cold front extending from the Florida panhandle southwestward into the Gulf of Mexico separated maritime tropical (mT) air from maritime polar (mP) air. The second frontal system extended southwestward from a cyclone in Pennsylvania to the Texas Gulf Coast and separated the mP air from much colder continental arctic (cA) air. Northerly flow around a surface anticyclone located in Montana sent temperatures plunging as low as -20°C in the Northern Plains States. Most of the AVE III area was covered by dense cloud cover. Rain showers and drizzle occurred along the East Coast while rain showers and a few thunderstorms were located over Florida. An extensive area of light snow was occurring in the cA air over the Midwest States and the Ohio River Valley.

A broad trough dominated the middle- and upper-tropospheric flow over North America. The jet stream with wind speeds as great as 90 m s^{-1} extended from the New England States southwestward into Texas.

Surface and upper-air systems moved slowly eastward during the AVE III period. Showers and thunderstorms occurred from Louisiana to South Carolina in association with the advancing frontal systems. By 1200 GMT 7 February the fronts were located over the Florida peninsula (Fig. 1-6). A large anticyclone, centered over East Texas, dominated the surface circulation. Light snow occurred from New England into the Appalachians, but clear skies were reported in the AVE III area west of the Mississippi River. The broad trough continued to dominate the upper-level flow pattern, but the trough axis had moved east of the center of the AVE III area.

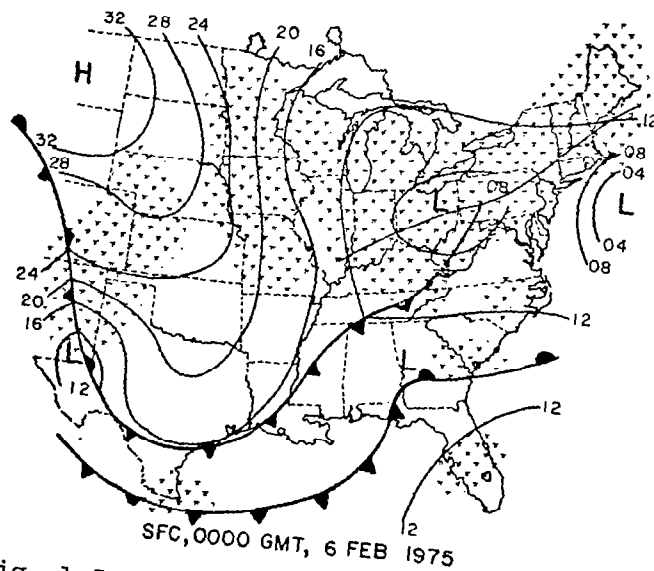
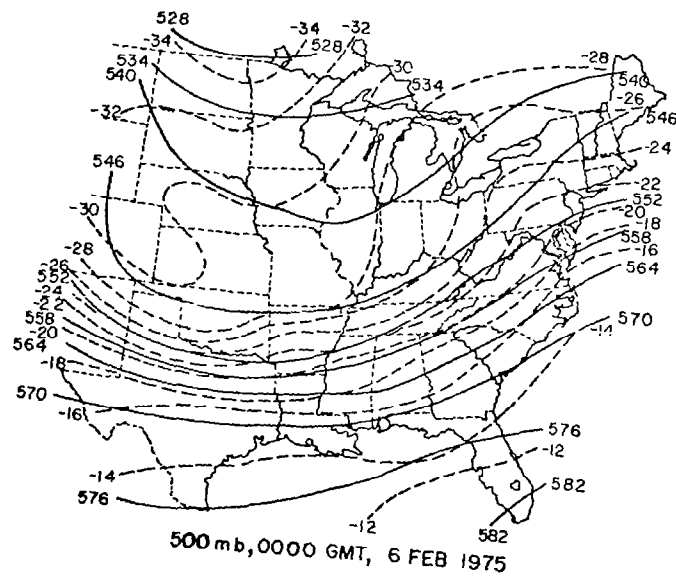
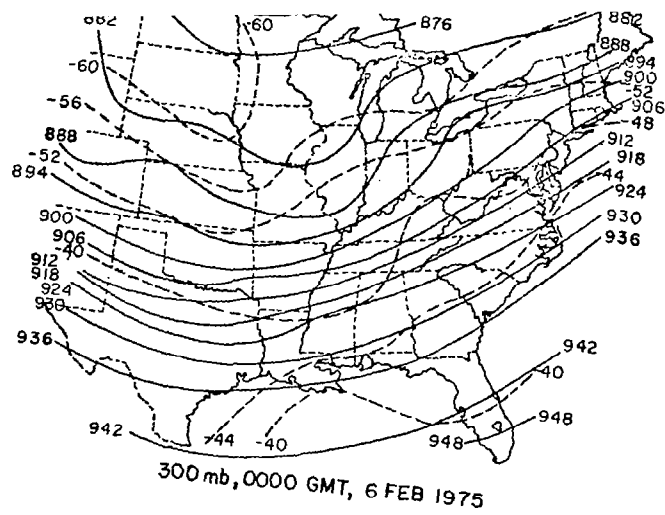


Fig. 1-5. Synoptic conditions at 0000 GMT
6 February 1975.

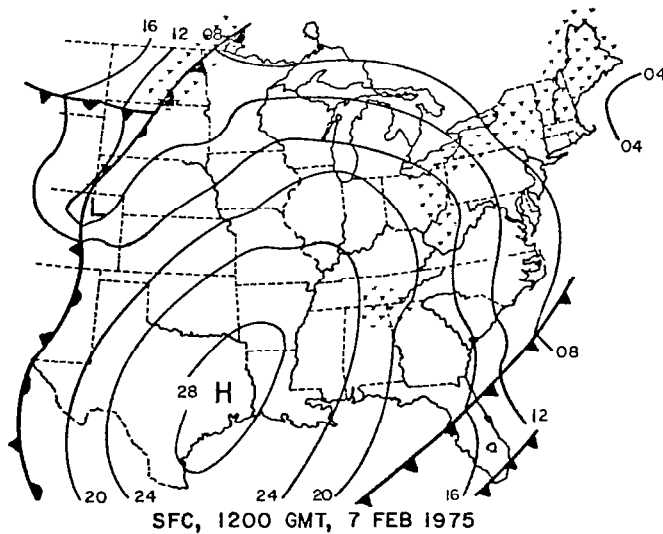
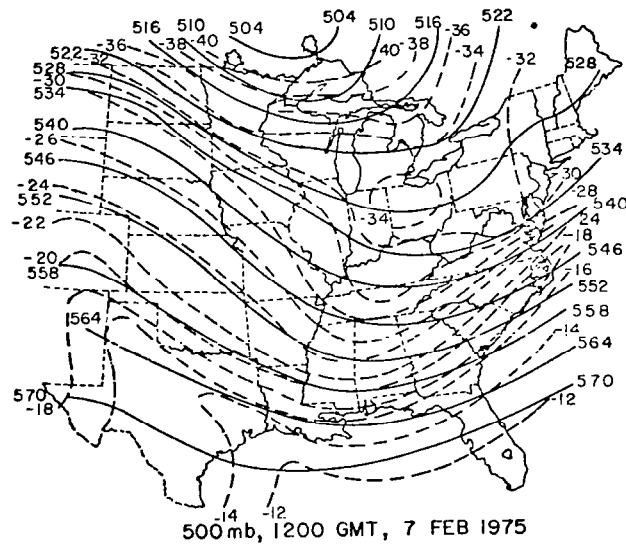
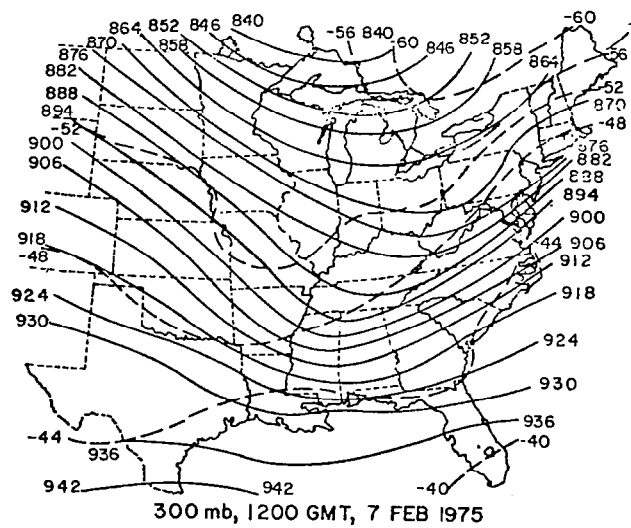


Fig. 1-6. Synoptic conditions at 1200 GMT
7 February 1975.

1.4 References

- Barnes, S. L., 1964: A technique for maximizing detail in numerical weather map analysis. J. Appl. Meteor., 3, 396-409.
- Barr, S., W. K. Widger, Jr., I. A. Miller, and R. Stanton, 1971: Objective subsynoptic upper level analysis. J. Appl. Meteor., 10, 410-417.
- Brousaides, F. J., 1975: The radiosonde hygistor and low relative humidity measurements. Bull. Amer. Meteor. Soc., 56, 229-233.
- Chien, H., and P. J. Smith, 1973: On the estimation of kinematic parameters in the atmosphere from radiosonde wind data. Mon. Wea. Rev., 101, 252-261.
- Fankhauser, J. C., 1969: Convective processes resolved by a mesoscale rawinsonde network. J. Appl. Meteorol., 8, 778-798.
- Foster, D. S., and R. M. Reap, 1973: Archiving of manually-digitized radar data, Techniques Development Laboratory Office Note 73-6, National Weather Service, Silver Springs, Md., 12 pp.
- Fuelberg, H. E., 1974: Reduction and error analysis of the AVE II pilot experiment data. NASA CR-120496, George C. Marshall Space Flight Center, Alabama, 131 pp.
- _____, and R. E. Turner, 1975: Data for NASA's AVE III experiment: 25-mb sounding data and synoptic charts. NASA TM X-64938, George C. Marshall Space Flight Center, Alabama, 462 pp.
- Kung, E. C., 1974: Note on design of an optimized computation scheme for kinematic vertical motion fields. Mon. Wea. Rev., 101, 685-690.
- Lenhard, R. W., 1973: A revised statement of radiosonde accuracy. Bull. Amer. Meteor. Soc., 54, 691-693.
- O'Brien, J. J., 1970: Alternate solutions to the classical vertical velocity problem. J. Appl. Meteorol., 9, 197-203.
- Scoggins, J. R., and O. E. Smith, 1973: Data for the first NASA atmospheric variability experiment (AVE I), Part I: Data tabulation. NASA TM X-2938, George C. Marshall Space Flight Center, Alabama, 681 pp.
- Shuman, F. G., 1957: Numerical methods in weather prediction: II. Smoothing and filtering. Mon. Wea. Rev., 85, 357-361.
- Smith, P. J., 1971: An analysis of kinematic vertical motions. Mon. Wea. Rev., 99, 715-723.

- Vincent, D. G., K. E. Bossingham, and H. J. Edmon, Jr., 1976: Comparison of large scale vertical motions computed by the kinematic method and quasi-geostrophic ω -equation. Preprints of Papers, Sixth Conf. on Weather Forecasting and Analysis, Amer. Meteor. Soc., Albany, 357-364.
- Wilson, G. S., 1976: Large-scale vertical motion calculations in the AVE IV experiment. Geophys. Res. Letters, 3, 735-738.
- _____, and J. R. Scoggins, 1976: Atmospheric structure and variability in areas of convective storms determined from 3-h rawinsonde data. NASA CR-2678, NASA Marshall Space Flight Center, Huntsville, Alabama, 118 pp.

VORTICITY IMBALANCE AND STABILITY IN AVE III

by

William L. Read*
Department of Meteorology
Texas A&M University
College Station, Texas 77843

ABSTRACT

The synoptic scale vorticity budget and an analysis of instability by the use of indices were related to convective storm development during AVE III as was done previously for AVE IV. AVE III is a wintertime case; AVE IV a springtime case. The results show that stability is a better indicator of intense convection during AVE III than during AVE IV; the kinematics associated with vorticity budget calculations show the same features in both cases; the stability indices developed from the AVE IV data outlined convective areas well in AVE III but too small values were obtained for nonconvective areas; and large imbalances in the vorticity budget reflected by the residual term show systematic, wave-like patterns along the jet stream that may be related to sub-grid scale systems.

*Presently employed by National Weather Service, San Antonio, Texas.

CHAPTER 2. VORTICITY IMBALANCE AND STABILITY IN AVE III

2.1 Introduction

This work is a second case study on determining synoptic-scale features that lead to convective precipitation. The first case study (Read and Scoggins, 1977) utilized rawinsonde and surface data taken during the AVE IV experiment. The AVE IV synoptic situation was typical of springtime severe storm cases and, therefore, provided widespread convection for study. In this second case study, an entirely different synoptic situation was used in order to investigate differences from the AVE IV case. The AVE III experiment, conducted on 6 and 7 February 1975, was a typical East Coast winter storm pattern, with intense convection confined to South Florida and non-convective precipitation occurring elsewhere.

The elements of this study are the same as in the first case. They include calculations of a vorticity budget using the complete vorticity equation, stability fields in the lower troposphere using lapse rate of equivalent potential temperature, and thunderstorm potential indices using combined fields of vorticity and stability terms. In the first case study, average profiles as a function of different intensities of convection were prepared for the various parameters above to establish general relationships. This same procedure was used for AVE III. However, due to the relatively small area of intense convection and its location, emphasis will be on comparing results in non-convective areas to those observed in AVE IV.

2.2 Analytical Methods

2.2.1 Vorticity equation

The development of synoptic-scale cyclonic circulations during the AVE III experiment was studied by use of the vorticity budget. The equation for the rate of change in the vertical component of the curl of velocity is

$$\overset{1}{\frac{\partial \zeta}{\partial t}} + \overset{2}{\vec{V}_p \cdot \vec{\nabla}_p} (\zeta + f) + \overset{3}{\omega \frac{\partial \zeta}{\partial p}} = -(\zeta + f) \overset{4}{\vec{\nabla}_p \cdot \vec{V}_p} + \overset{5}{\frac{\partial \omega}{\partial y} \frac{\partial u}{\partial p} - \frac{\partial \omega}{\partial x} \frac{\partial v}{\partial p}} + \overset{6}{\vec{k} \cdot \vec{\nabla}_x F}, \quad (2-1)$$

where term 1 is the local time rate of change of relative vorticity, term 2 the advection of absolute vorticity on isobaric surfaces, term 3 the vertical advection of vorticity, term 4 the production of absolute vorticity through

divergence, terms 5 the transfer of vorticity between horizontal and vertical axes and are called the twisting terms, and term 6 the vorticity production by friction. In this study, term 6 will be solved for as a residual and will represent imbalance between the total derivative and synoptic-scale sources of vorticity in Eq. (2-1). Terms 1-5 represent contributions by mean quantities while the residual represents a combination of perturbation quantities, viscous friction, measurement error, and computational error (truncation).

2.2.1.1 Computational procedures

The vorticity budget was computed for the surface-, 850-, 700-, 500-, and 300-mb levels. All terms in the equation were computed at each level except at the surface where terms involving ω were neglected. Terms in Eq. 2-1 were evaluated at each grid point from the analyzed fields of u and v wind components. Vertical motion was computed using the kinematic method with an adjustment technique developed by O'Brien (1970) applied to smooth the effect of errors that accumulate when integrating the continuity equation. Boundary values used were terrain-induced vertical motion at the surface and the adiabatic vertical motion at 100 mb, as given by Panofsky (1959).

The time derivative in Eq. 2-1 was approximated by centered finite differences except at the initial time, where a forward difference was applied, and the last time where a backward difference was applied. All horizontal and vertical spatial derivatives were approximated by centered finite differences. The depth interval used to approximate vertical derivatives was 200 mb.

2.2.1.2 Method of presentation of results

The error analysis indicated that individually analyzed fields of terms in the vorticity equation could contain significant error. In order to develop relationships between the terms of Eq. 2-1 and convection, and to reduce the effect of random errors, parameters were averaged over all nine times for several categories of convection.

The categories of convection were based on the MDR code with $MDR \leq 1$ representing no convection, $MDR \geq 2$ representing all convection, $MDR \geq 4$ representing thunderstorms, and $MDR \geq 8$ representing severe thunderstorms. First, grid point values of MDR data had to be determined for each time. From the composited MDR charts the maximum MDR values within a scan radius of one grid distance from each grid point was chosen to be the MDR value at that grid point. Averages of each term were then computed for each MDR

category. Averages were computed for each level and graphs were prepared showing the vertical distribution of average values of terms in the vorticity equation.

Operational 12-h sounding intervals rarely allow one to study atmospheric conditions prior to initial development of thunderstorms. With 12-h data, extrapolation of conditions over an unacceptable length of time frequently is done. The 3- and 6-h intervals in AVE III provide the opportunity to examine synoptic conditions before thunderstorms develop. To test these conditions, average values of the terms in the vorticity equation were computed for 3- and 6-h lags in MDR fields. This was done by comparing the gridded fields of terms in the vorticity equation at each time with the observed convection 3- and 6-h later. Differences between these profiles and the ones for zero lag give an indication of how long favorable conditions on the synoptic scale exist prior to the development of thunderstorms. This also indicates what large scale changes take place, if any, in areas of convection after thunderstorm development.

In order to determine the usefulness of general relationships between convection and terms in the vorticity equation, individually analyzed fields were examined. Examples are presented and discussed below.

2.2.2 Stability

2.2.2.1 Computational procedure

A convectively unstable layer of air is required for thunderstorm development. The average tornado sounding presented by Miller (1967) indicates the presence of a dry, subsidence inversion in the lower troposphere with convective instability being greatest in the layer containing the inversion. In this research three layers, one generally below the inversion, one containing the inversion, and one above the inversion, were used to compute convective instability. Stability in each layer was compared to radar-observed convective activity.

The three layers used were the surface to 850 mb, 850 to 700 mb, and 700 to 500 mb. In addition, convective instability in the layer from the surface to 500 mb was computed to see if a deep layer measurement adequately described the stability requirement. Convective instability, σ_e , was defined by $-\frac{\partial \theta_e}{\partial p}$, where θ_e is equivalent potential temperature. Grid point values of σ_e were computed at the top and bottom of each layer using gridded fields of temperature and dew point temperature. σ_e was evaluated by finite

differences from grid point values of θ_e with Δp equal to the difference between the pressures at the top and bottom of each layer.

2.2.2.2 Method of presentation of results

General relationships between convective instability and thunderstorms were developed in the same fashion as the vorticity budget. Averages for zero lag were computed to investigate synoptic-scale instability in areas of observed convective activity while averages for 3- and 6-h lags in MDR data were used to study conditions prior to thunderstorm development.

Individually analyzed fields were used to establish whether the general relationships hold for specific time periods, and to study changes in stability during the life cycle of convective systems.

2.2.3 Thunderstorm Potential Indices

2.2.3.1 Rationale

As shown in previous studies, neither stability nor kinematic parameters alone provide a very good analysis or forecast tool for severe weather. Wilson and Scoggins (1976) showed that, by combining an index of stability with vertical motion, a substantial improvement in depicting severe thunderstorms could be achieved. Statistical techniques used by the weather services combine many observed and forecast parameters in making a severe weather forecast. Endlich and Mancuso (1968) have developed indicators for severe weather by combining scaled parameters of moisture, stability, and kinematics into a single parameter. Analyzed fields of these indicators correlated better with convection than did the individual parameters that made up the indicator.

In this study an index was developed to combine, in a simple manner, the effects of moisture, stability, and vorticity development. Since this is only one case study, no attempt is made to develop exact statistical relationships of the type used by the National Weather Service (Charba, 1975). The combinations were chosen based on physical reasoning with essentially equal weight placed on each input parameter.

A direct measure of moisture was required since the vorticity equation is independent of moisture and σ_e considers only the vertical distribution of moisture. Wilson and Scoggins (1976) found boundary layer moisture to correlate best with observed thunderstorms; therefore, in this study the average mixing ratio \bar{q} from the surface to 850 mb was used as a moisture parameter.

Terms in the vorticity equation indicating development of circulation systems are expected to correlate best with areas of convection. In the

lower levels, terms involving ω and its gradients are generally negligible on the synoptic-scale. Horizontal advection should be smaller than the divergence term due mainly to smaller wind speeds. In the lower levels the dominating terms are the local derivative, divergence term, and friction. For use in an index, the divergence term was preferred since it relates to a source of vorticity in the lower layers.

In the middle and upper troposphere, the dominant terms in the vorticity equation are horizontal advection, divergence, and the local derivative of vorticity. From scale analysis, terms involving ω should be small compared to the other terms. If the equation is applied at the level of non-divergence, usually near 500 mb, development of circulation is primarily due to vorticity advection $[\vec{V}_p \cdot \vec{\nabla}_p (\zeta + f)]$. In the presence of vorticity production by convergence, such development would be enhanced. However, error analysis (Read and Scoggins, 1977) indicates that, at the upper levels, the divergence term is considerably more in error than the horizontal advection term. Hence, vorticity advection at 500 mb is the preferred vorticity development input to the index.

As stated earlier, instability is an essential criterion for thunderstorm development. The exact layer in which this instability should exist for maximum development is not known and probably varies for different cases. In many cases, boundary layer instability is probably most important, while with strong lifting, upper-level instability may be important. The depth of the layer of instability is certainly of importance and the indices developed include this as well as the instability observed in the boundary layer and aloft.

2.2.3.2 Definitions

Three initial indices were formed, two representing lower tropospheric synoptic conditions and one representing upper-level conditions. Two thunderstorm potential indices were formed by adding each of the low-level indices separately to the upper-level index.

The low-level indices (LLI) were computed using the following formulas;

$$\text{LLI 1} = [\sigma_{\text{Sfc-850}}^* + (\zeta + f) (\vec{V}_p \cdot \vec{\nabla}_p)^*] \bar{q}, \text{ and} \quad (2-2)$$

$$\text{LLI 2} = [\sigma_{\text{850-700}}^* + (\zeta + f) (\vec{V}_p \cdot \vec{\nabla}_p)^*] \bar{q}, \quad (2-3)$$

where an overbar indicates an average from the surface to 850 mb, and * indicates that the quantities have been scaled by their standard deviation as was done by Endlich and Mancuso (1968). Scaling was required due to the different orders of magnitudes of the stability and vorticity terms. In order to obtain the proper effect of moisture, average specific humidity (or mixing ratio) was used as a multiplier instead of being added to the index. Simply adding the term to the index would not effectively reduce the potential for thunderstorm development in areas where insufficient moisture was observed.

High negative values of either index indicate moist, unstable air and vorticity production occurring at the same point. Where these factors occur simultaneously, environmental conditions in the lower troposphere are excellent for thunderstorm development.

The upper level index (ULI) was defined by

$$ULI = [\sigma_{e_{700-500}}^* + \vec{V}_p \cdot \vec{V}_p (\zeta + f)^*] \bar{q}, \quad (2-4)$$

where symbols have the same meaning as for the low-level index. Since dry, low-level regions often exhibit unstable conditions between 700 and 500 mb as well as positive vorticity advection at 500 mb, the low-level average mixing ratio, \bar{q} , was used to reduce the effect of strong advection in areas of low moisture content. Again, areas that have large negative values of the upper index are areas of upper-level instability and positive vorticity advection above a moist boundary layer.

The two Thunderstorm Potential Indices (TPI) are given by

$$TPI\ 1 = LLI\ 1 + ULI, \text{ and} \quad (2-5)$$

$$TPI\ 2 = LLI\ 2 + ULI. \quad (2-6)$$

Minimum values of each occur where moist, unstable air with production of vorticity in the lower troposphere is located beneath regions of mid-tropospheric instability and positive vorticity advection.

2.2.3.3 Method of presentation of results

Fields of the low level, upper level, and thunderstorm potential indices were examined for correlation with thunderstorm activity to assess the improvements compared with the use of individual parameters of stability and vorticity production. Comparison between upper-level and lower-level indices was done to determine which was better at depicting severe weather development.

Analyzed fields are presented to show the effectiveness of the indices for outlining areas of convective activity. Subjective comparison between index fields and observed MDR values will be used to test the effectiveness of the indices.

2.3 Results

2.3.1 Average profiles

2.3.1.1 Stability

Figure 2-1 shows the average values of the four measures of σ_e for different categories of observed MDR data. This chart indicates the presence of the large stable air mass behind the cold front in AVE III. The nonconvective ($MDR \leq 1$) areas show large positive (stable) values in all layers. In areas of convection the boundary layer was unstable while upper layers were either neutral or slightly stable. In spite of the fact that only a few grid points had MDR values from 4-9, there appears to be a trend towards decreasing stability with increasing thunderstorm intensity in all layers.

In the springtime case of AVE IV, there were two major differences, viz, the nonconvective areas were unstable and convective areas exhibited greater instability in the middle and upper layers. For the springtime case, stability was deemed a poor indicator of intense convection. However, the results for AVE III indicate that stability, at least in the boundary layer, is an excellent prediction of wintertime convection.

The areas in AVE III where convection eventually developed exhibited an unstable lower troposphere both three and six hours prior to the initial development of convection (Figs. 2-2a and 2-2b). This result is similar to the results of the springtime case emphasizing the need for a trigger mechanism to release the instability.

2.3.1.2 Vorticity budget

In the AVE IV study, average profiles of the local time derivative of vorticity indicated cyclonic tendencies at all levels in areas of convection. The profiles for the AVE III case indicate that cyclonic tendencies in areas of convection were confined to the lower levels below 700 mb (Fig. 2-3). Only the MDR 2-9 category had cyclonic tendency at all levels.

Profiles for horizontal advection of vorticity for the AVE III case indicate that, in areas of convection, large negative values are confined to the upper levels (Fig. 2-4). In non-convective areas large positive values were observed. These results are essentially the same as in the AVE IV case.

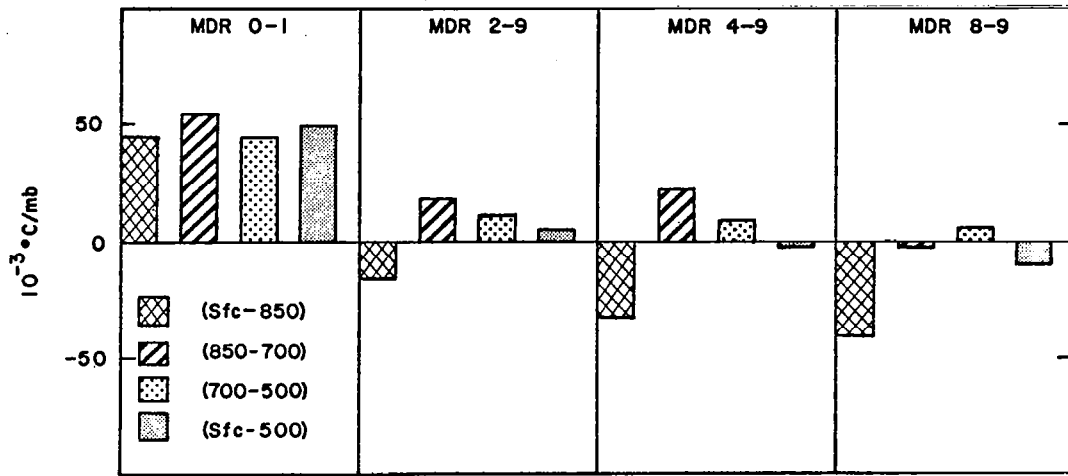
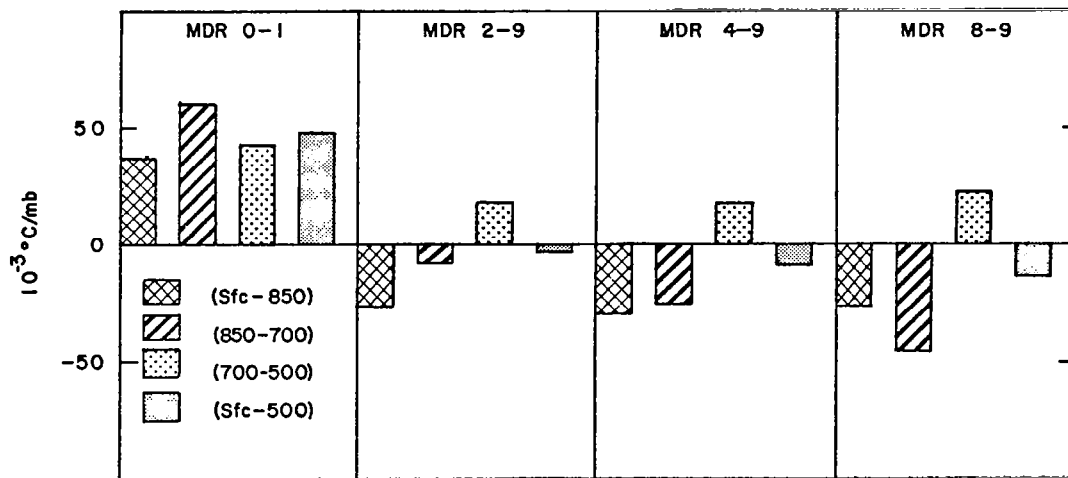
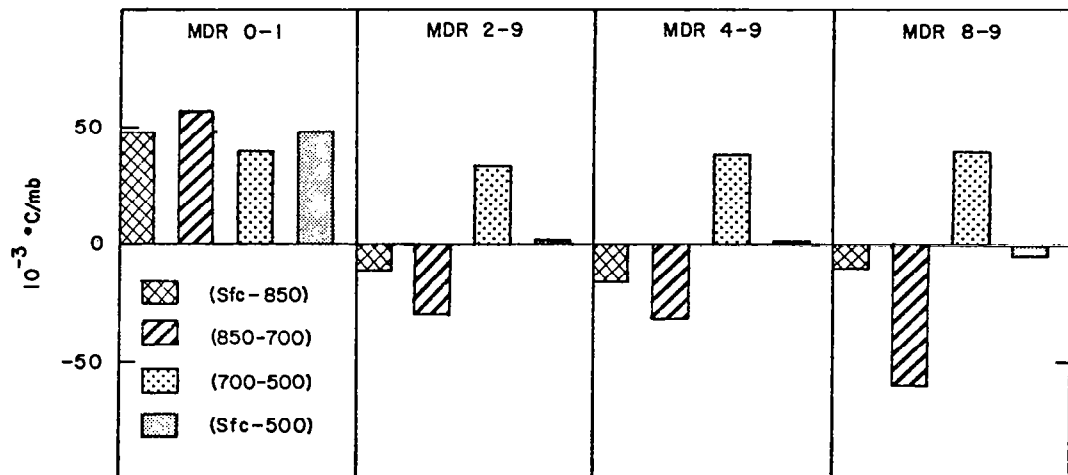


Fig. 2-1. Averages of convective instability ($10^{-3} \text{ }^{\circ}\text{C mb}^{-1}$) as function of MDR values.



(a) 3-h lag.



(b) 6-h lag.

Fig. 2-2. Averages of convective instability ($10^{-3} \text{ }^{\circ}\text{C mb}^{-1}$) with time lags in MDR.

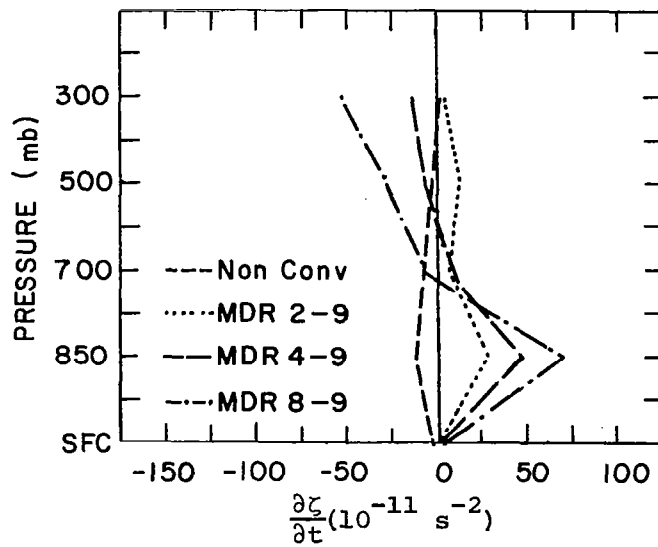


Fig. 2-3. Average profiles for the local derivative of vorticity.

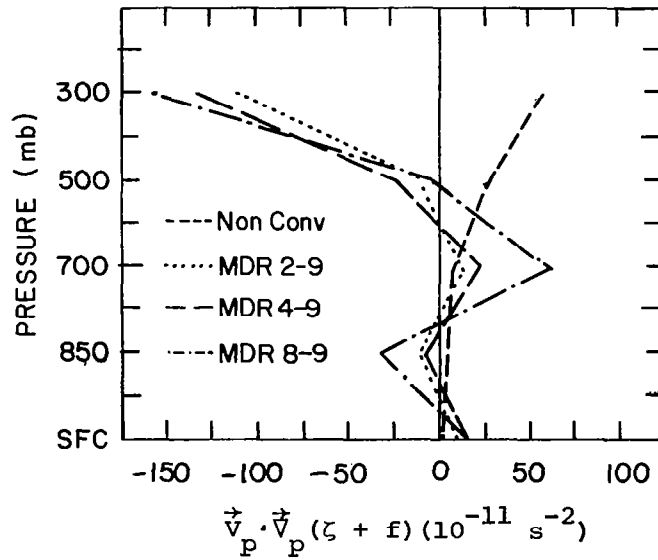


Fig. 2-4. Average profiles of horizontal vorticity advection.

Terms involving vertical motion were found to be negligible when considering the average vorticity budget in AVE IV. The same magnitudes for the vertical advection and twisting terms were found for the AVE III case (Figs. not shown).

In the springtime case, the divergence term was the dominant term both in the lower and upper troposphere in areas of convective activity. In AVE III the divergence term is dominant at the surface but is smaller than horizontal advection at 300 mb (Fig. 2-5). Non-convective areas show an opposite profile for this term for both cases. Profiles of the total derivative and sum of divergence and twisting terms for AVE III (not shown) are essentially the same as the profiles of the horizontal advection and divergence terms, respectively.

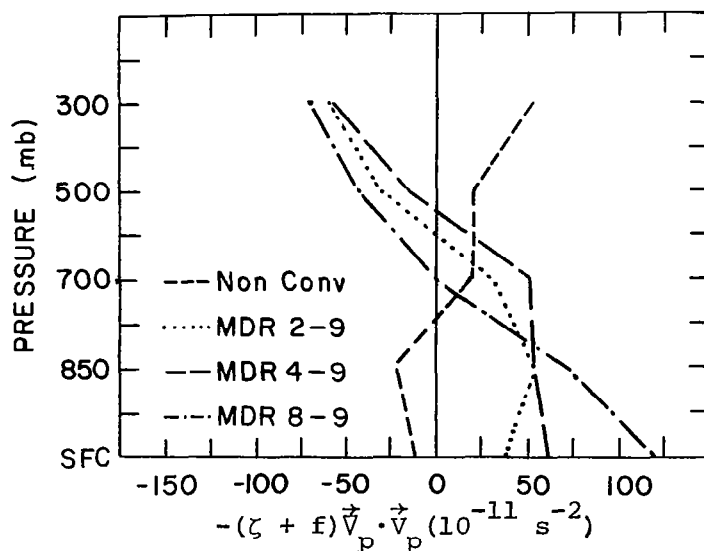


Fig. 2-5. Average profiles of the divergence term.

In AVE IV, profiles of the residual in areas of convection revealed large negative imbalances in the lower levels and large positive imbalances at 300 mb. It was concluded that the sub-grid scale processes were responsible for maintaining balance in the vorticity budget. The AVE III case study reveals that both lower and upper levels have negative residuals (Fig. 2-6). In the lower levels this represents large positive values of the divergence term not being balanced by advection or large cyclonic tendencies. The difference between AVE III and AVE IV is that more negative values of advection and less negative values of the divergence term occurred during AVE III at 300 mb. This possibly resulted because strong wind speeds

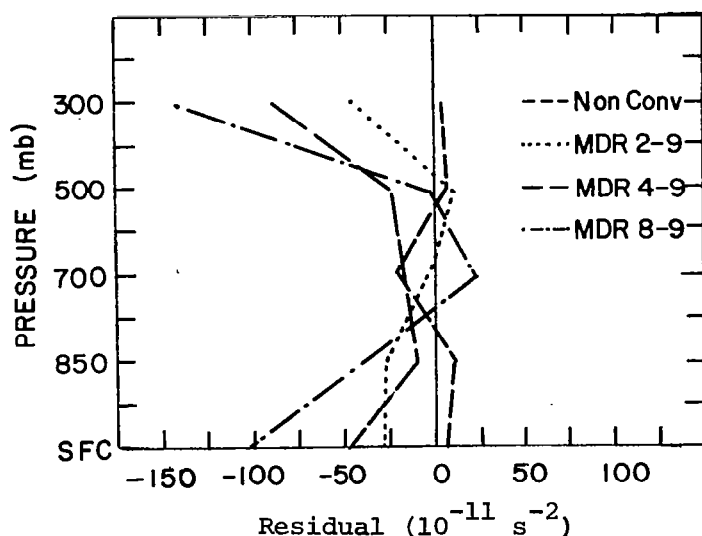


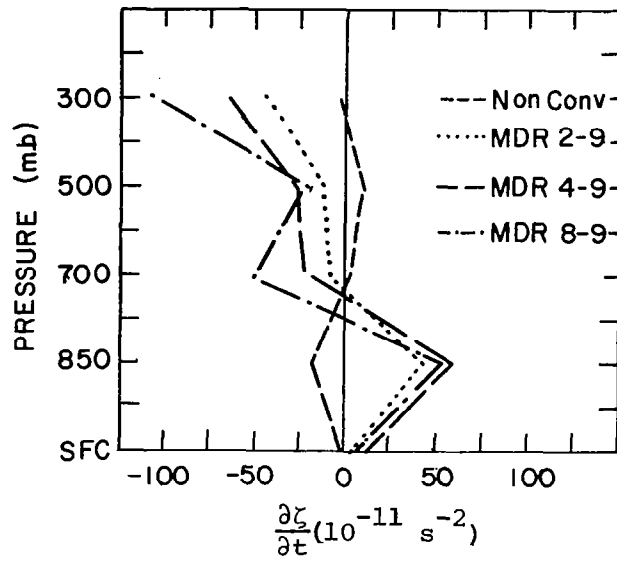
Fig. 2-6. Average profiles of the residual.

and large shears in AVE III contributed to larger values of advection without increasing the divergence term. More studies of both springtime and wintertime cases would be required to determine if this difference is significant.

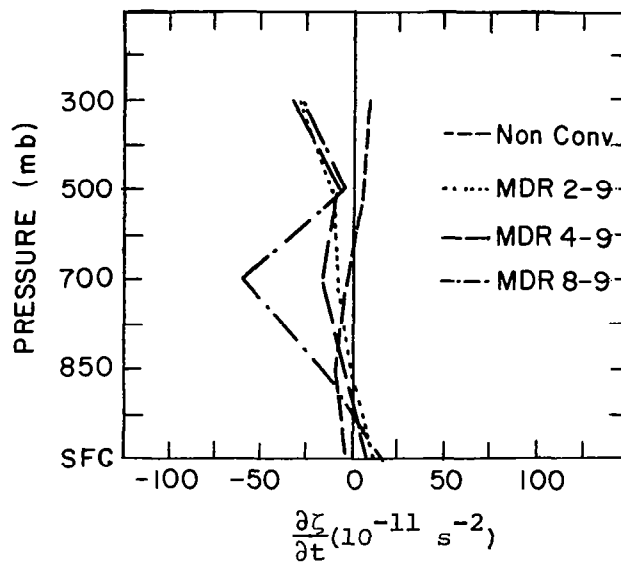
Profiles of terms in the vorticity equation three and six hours prior to initial development were prepared as in the AVE IV case. Figure 2-7 shows 3- and 6-h lag averages for the local derivative. Low-level cyclonic tendencies occur 3 h but not 6 h prior to initial development, indicating that, in the AVE III case, cyclonic development occurs shortly before initial thunderstorm development. In AVE IV cyclonic tendencies were evident both three and six hours prior to convective activity.

Profiles of horizontal vorticity advection three and six hours prior to initial convective activity closely resemble the profiles at zero lag, with slightly smaller magnitudes (Fig. 2-8). For areas of convection, only the upper levels above 500 mb experience positive vorticity advection [negative $\vec{V}_p \cdot \vec{\nabla}_p (\zeta + f)$], while the opposite is true for non-convective areas. As in the springtime case, positive upper-level advection was a maximum three hours prior to initial development. Also, the 6-h lag profiles showed no significant difference between convective and non-convective areas.

Profiles of the divergence term for AVE III three and six hours prior to thunderstorm development are shown in Fig. 2-9. There is a significant difference between convective and non-convective areas. Low-level convergence

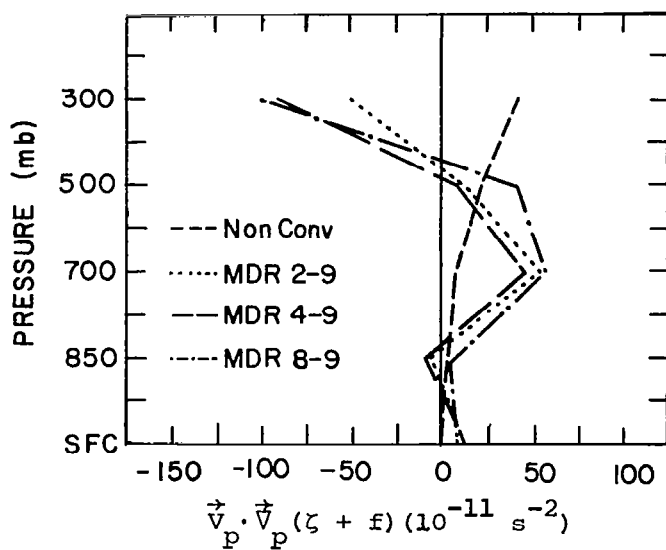


(a) 3-h lag in MDR

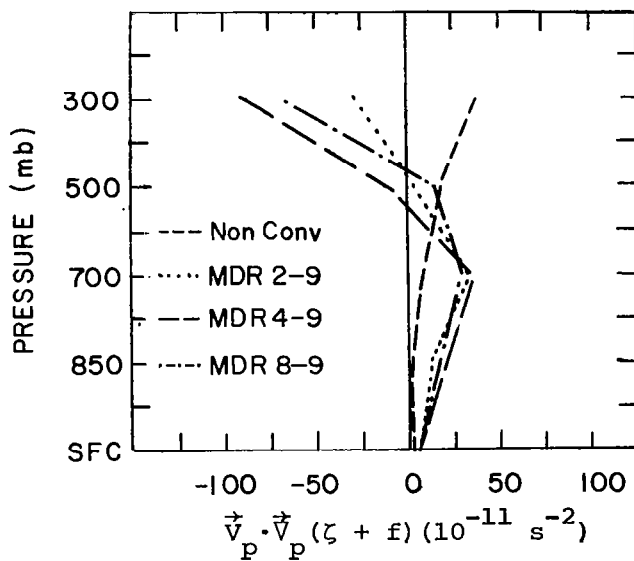


(b) 6-h lag in MDR

Fig. 2-7. Average profiles of the local derivative of vorticity for time lags in MDR of 3 and 6 hours.

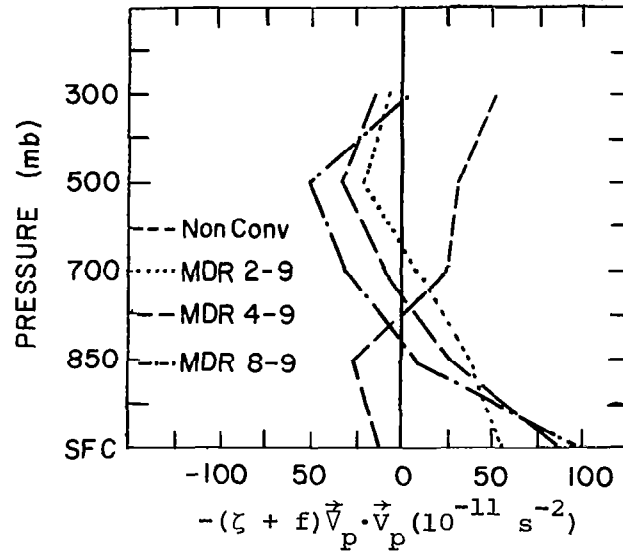


(a) 3-h lag in MDR.

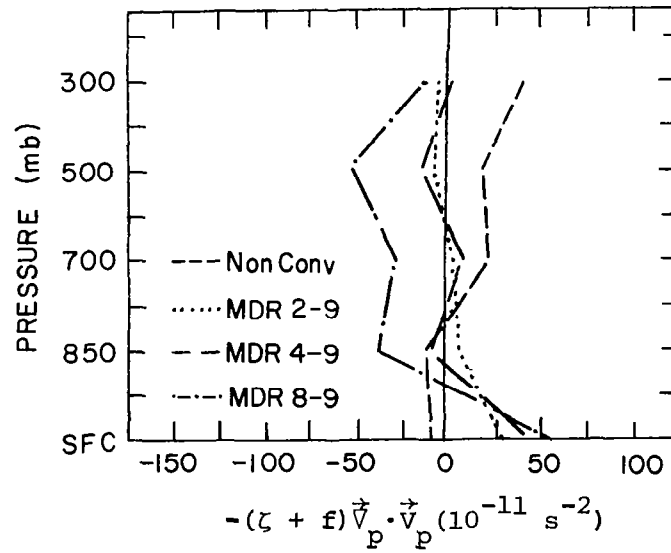


(b) 6-h lag in MDR.

Fig. 2-8. Average profiles of horizontal vorticity advection for time lags in MDR of 3 and 6 hours.



(a) 3-h lag in MDR.



(b) 6-h lag in MDR.

Fig. 2-9. Average profiles of the divergence term for time lags in MDR of 3 and 6 hours.

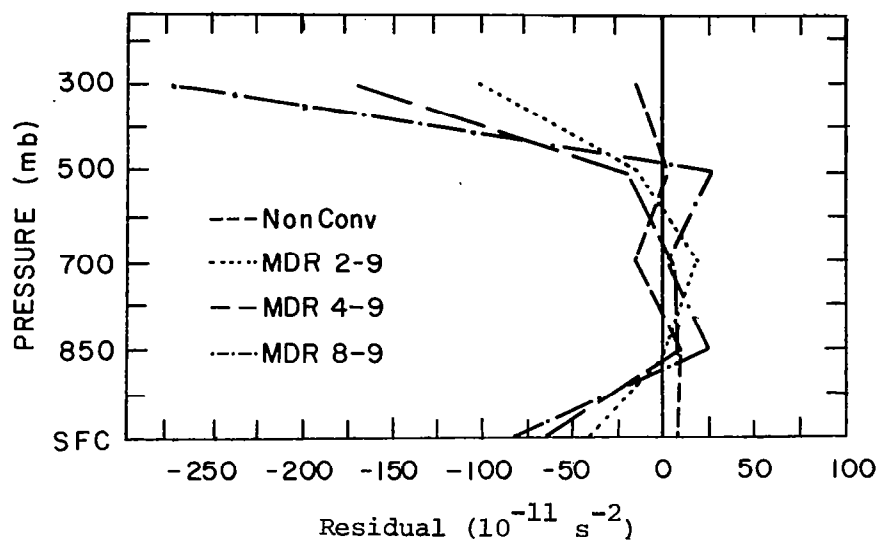
is present for convective areas up to six hours prior to initial formation while non-convective areas remain divergent. Opposite conditions exist aloft. These results are virtually the same as in AVE IV.

The 3- and 6-h lag profiles of the residual show that a systematic imbalance occurs as much as six hours prior to thunderstorm development in both the boundary (surface to 850 mb) and upper levels (Fig. 2-10). In the lower levels, large values of the divergence term are not balanced by either large-scale advection or cyclonic tendencies. Again, this is the same result as in AVE IV. The upper levels have large negative values because large values of horizontal advection are not being balanced by either cyclonic tendencies or divergence. This differs somewhat from AVE IV, when advection was smaller aloft. The more intense jet stream in the AVE III case probably is the cause of larger values of advection. Subgrid scale kinematic features may again be responsible for restoring balance, since turbulent flow has been observed within strong shear regions in the vicinity of jets.

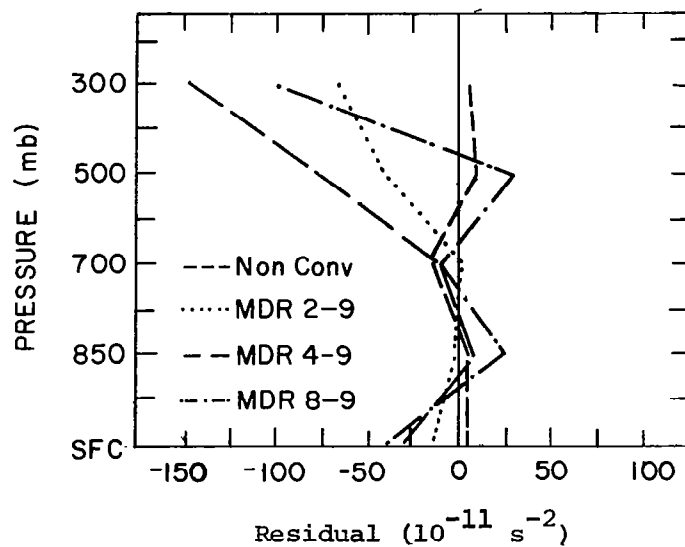
2.3.2 Thunderstorm potential indices

In the springtime case, indices were developed that combined kinematic and thermodynamic quantities. The same indices, previously described by Eqs. 2-2 through 2-6, were used in AVE III to test their applicability to a wintertime situation.

The results from AVE IV indicated that the inclusion of both upper- and lower-level effects in an index accurately depicted areas of thunderstorm development. Large negative values correlated well with areas of intense thunderstorms. In AVE III the only intense thunderstorms were over the eastern Gulf of Mexico and Florida. The only large negative values of any one of the indices was in the southeast, in fairly good agreement with observed thunderstorms. The large areas of snow in the midwest and northeast were not clearly associated with negative values except for an area of strong snow showers in western Pennsylvania. Examples of all the indices are shown in Fig. 2-11 for 0000 GMT 6 February. The large areas of small values associated with the high pressure area over the Plains States reveals a problem in attempting to use this index in winter. This area has strong low-level divergence, negative vorticity advection, and very stable air; but by multiplying the index with the average mixing ratio, which is very small, relatively small values of the final index are observed. However, in general, it appears that the indices still perform well enough to depict synoptic-scale areas favorable for intense ($MDR \geq 4$) convection.

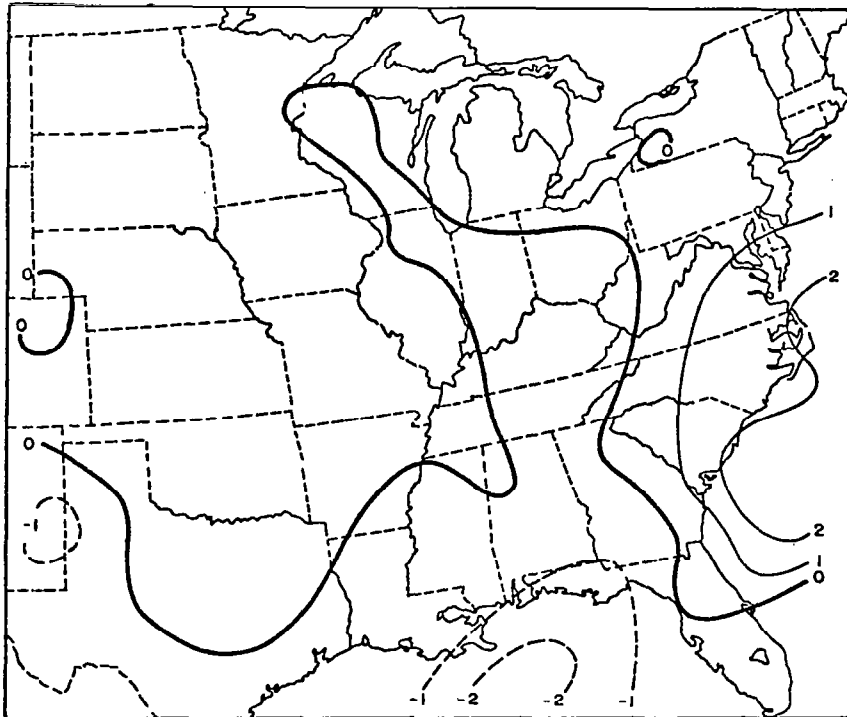


(a) 3-h lag in MDR.

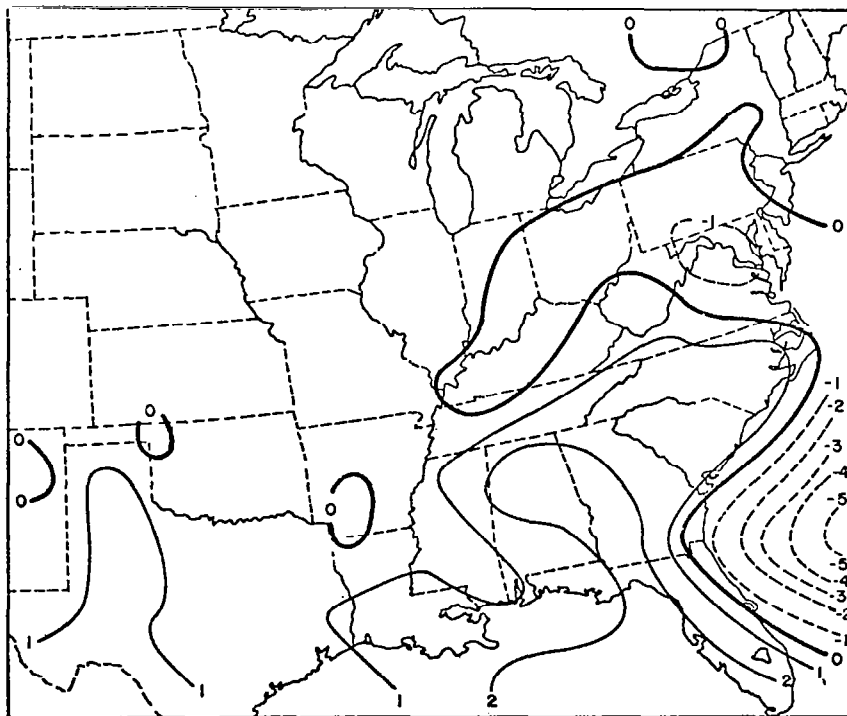


(b) 6-h lag in MDR.

Fig. 2-10. Average profiles of the residual for time lags in MDR of 3 and 6 hours.

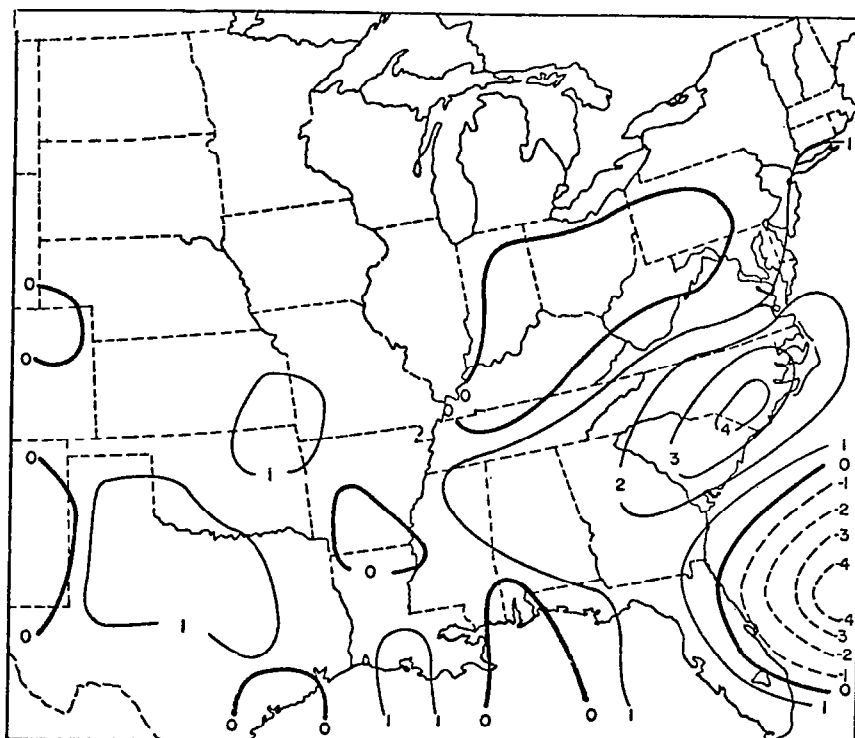


(a) LLI 1

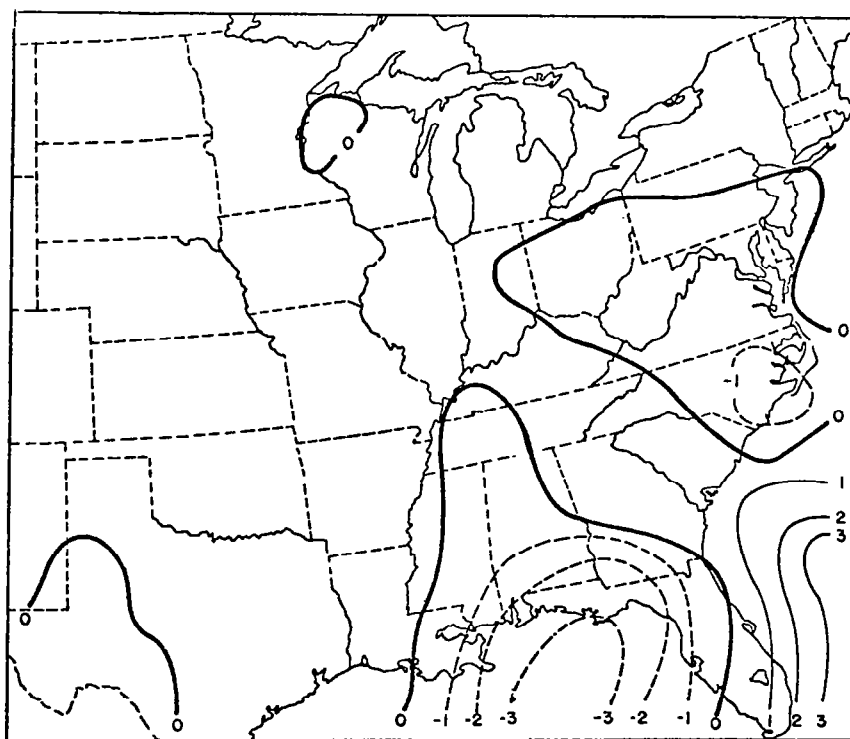


(b) ULI

Fig. 2-11. Analyzed fields of thunderstorm indices for 0000 GMT on 6 February 1975. (See Appendix for MDR data and thunderstorm location.)

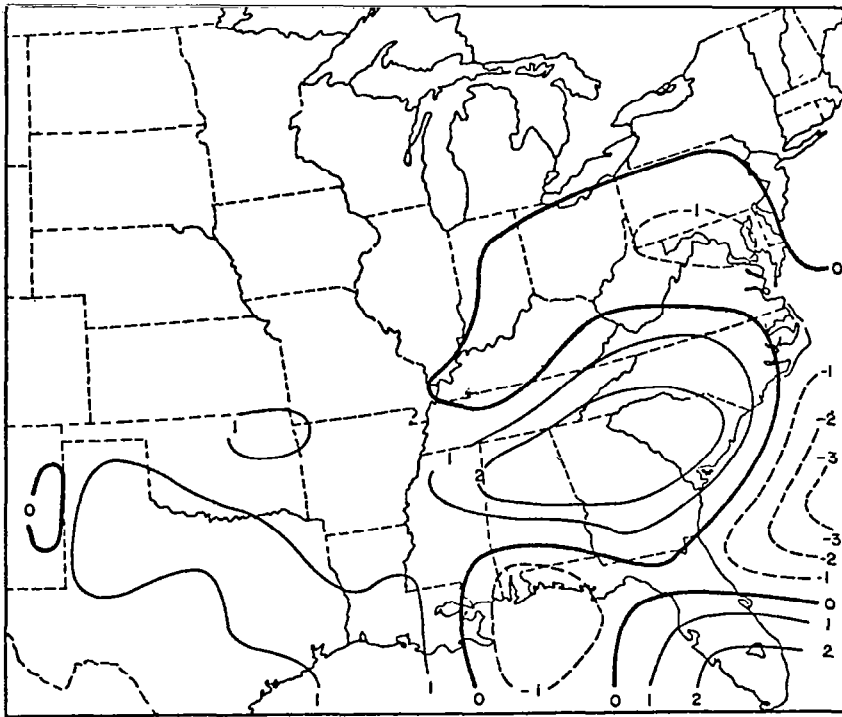


(c) TPI 1



(d) LLI 2

Fig. 2-11. (Continued).



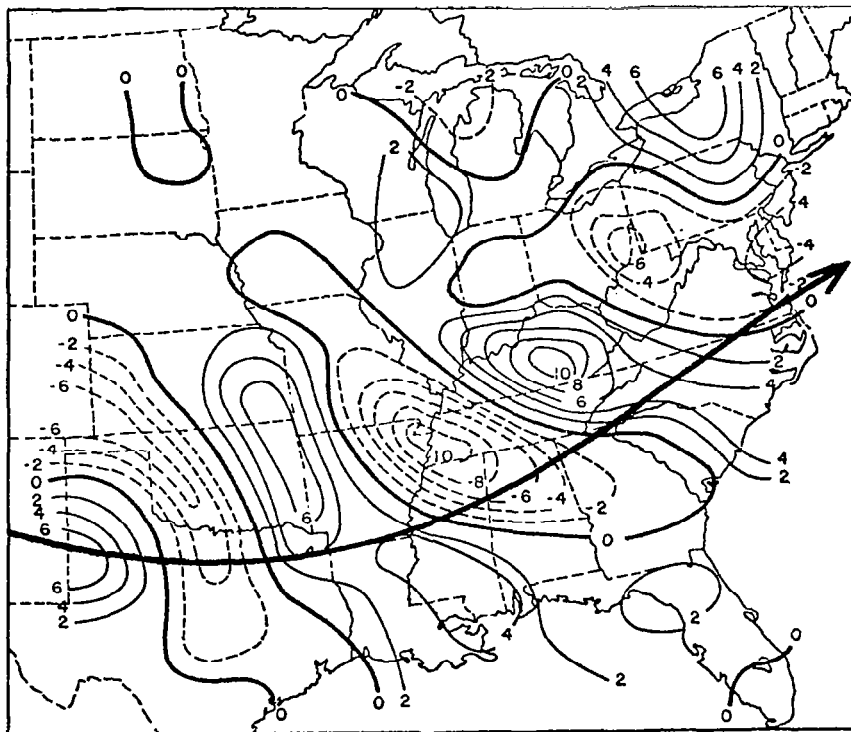
(e) TPI 2

Fig. 2-11. (Continued).

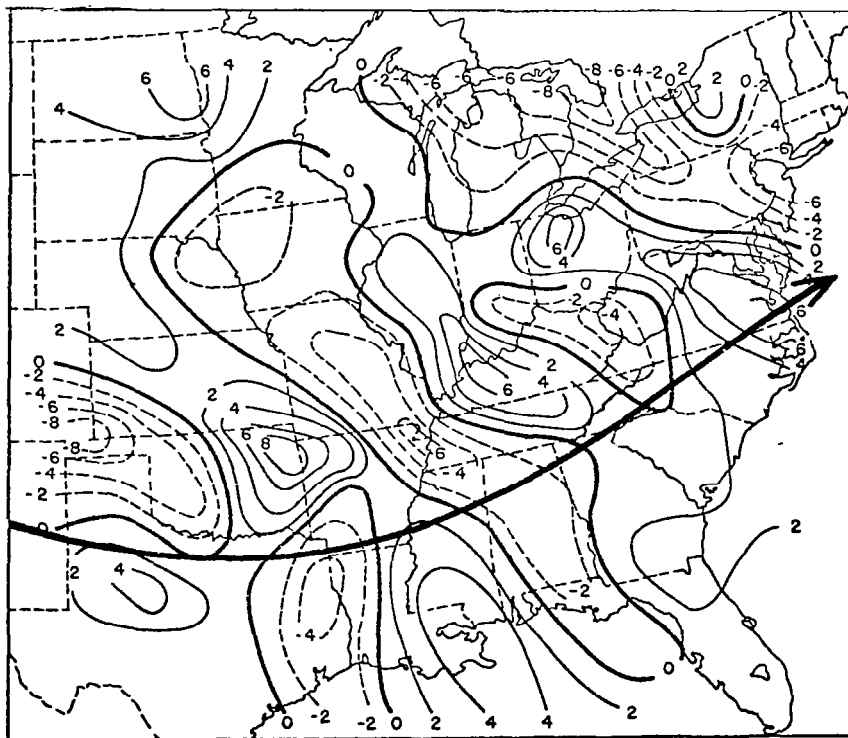
2.3.3 Apparent relationship of residual to the jet stream

In AVE IV, the average profiles of the residual term indicated a systematic imbalance among the computed terms in the vorticity equation in areas of intense convection. While the residual on the average was also systematic in AVE III, a more interesting result is observed in the analyzed fields. Figure 2-12 shows the 300-mb values of the residual at 0000 and 0600 GMT on 6 February 1975, with the jet stream at 300 mb superimposed. At both times there is a distinct pattern of maximum and minimum values for the residual along the core of the jet stream. The source of the pattern is not clear, as three different conditions were present. In some cases, large magnitudes of advection were not balanced by either a large divergence term or large local change terms. At other places, a large magnitude of the divergence term was not balanced by local change or advection. Thirdly, both advection and divergence in some cases were of equal value but opposite in sign.

It is also hard to determine exactly how much of this is an effect of measurement error. In the previous case study, an error analysis revealed that at low elevation angles (high wind speed), errors of over 100% in computed terms of the vorticity equation could be expected. However, this residual



(a) 0000 GMT 6 February 1975.



(b) 0600 GMT 6 February 1975.

Fig. 2-12. The residual term at 300 mb (10^{-9} s^{-2}) at (a) 0000 GMT and (b) 0600 GMT 6 February 1975 (see Appendix for MDR data).

pattern appears wave-like (on the order of 1000 km wavelengths), and resolution should be adequate, considering the input data, to partially define real atmospheric systems.

There are good arguments for expecting these large residuals along the jet stream to represent real effects. Many studies of clear air turbulence have shown that areas of turbulence occur along the jet streams, and satellite pictures clearly show that subsynoptic-scale wave phenomena are present along jet streams. The non-balance between synoptic scale advective and divergence effects in the vorticity equation may indicate areas favorable for subsynoptic wave development while the time continuity of these patterns lends support to the physical reality of the imbalance.

2.4 Conclusions

The following conclusions were reached based upon findings from the AVE III case study:

1. When compared to the AVE IV case, stability was a much better indicator of intense convection during the wintertime. In AVE IV large areas of unstable air had no convection.
2. Average profiles of the vorticity budget for AVE III indicate the kinematics of spring and winter convection are essentially the same.
3. The thunderstorm potential indices, although designed for spring-time convection, worked well for the AVE III case. However, the use of mixing ratio to scale down dry areas causes too small values for non-convective areas.
4. Large imbalance (residuals) in the vorticity budget show systematic, wavelike patterns along the jet stream that are possibly related to sub-grid scale systems.

2.5 References

- Charba, J. P., 1975: Operational scheme for short range forecasts of severe local weather. Preprints of Papers, Ninth Conf. on Severe Local Storms, Norman, 252-261.
- Endlich, R. M., and R. L. Mancuso, 1968: Objective analysis of environmental conditions associated with severe thunderstorms and tornadoes. Mon. Wea. Rev., 96, 342-350.

- Miller, R. C., 1967: Notes on analysis and severe storms forecasting procedures of the Air Force Global Weather Central. Air Weather Service Technical Report 200, 102 pp.
- O'Brien, J. J., 1970: Alternate solution to the classical vertical velocity problem. J. Appl. Meteorol., 9, 197-203.
- Panofsky, H. A., 1958: Introduction to Dynamic Meteorology, University Park, Pa., The Pennsylvania State University, 243 pp.
- Read, W. L., and J. R. Scoggins, 1977: Vorticity budget and stability in relation to convection. NASA CR-2819, NASA Marshall Space Flight Center, Huntsville, Alabama, 111 pp.
- Wilson, G. S., and J. R. Scoggins, 1976: Atmospheric structure and variability in areas of convective storms determined from 3-h rawinsonde data. NASA Contractor Report CR-2678, Marshall Space Flight Center, Alabama, 117 pp.

THE MOISTURE BUDGET IN AVE III

by

Robert W. Scott*
Department of Meteorology
Texas A&M University
College Station, Texas 77843

ABSTRACT

The moisture budget was evaluated for AVE III (a wintertime case) as was done previously for AVE IV (a springtime case). The results for AVE III compare closely with those for AVE IV in convective areas. In nonconvective areas in both experiments the terms were generally small in magnitude so that comparisons were difficult to make. Results from AVE III show that large amounts of moisture accumulated in convective areas through horizontal moisture divergence and that much of this moisture was transported vertically; a large negative residual was found in convective areas which was balanced by precipitation in these areas; and the accumulation of moisture occurred 3 hours in advance of cumulus development.

*Presently employed by Illinois State Water Survey, Urbana, Illinois.

CHAPTER 3. THE MOISTURE BUDGET IN AVE III

3.1 Introduction

An evaluation of the moisture budget in regions of thunderstorm activity occurring during the AVE IV experiment was performed by Scott and Scoggins (1977). The primary method of moisture accumulation during the experiment was through horizontal and vertical moisture divergence in the areas of convective storms. The purpose of this report is to investigate the moisture budget of the third AVE experiment using the methods developed for AVE IV. Comparisons of results and conclusions will be made in order to investigate similarities and differences in the two experiments.

3.2 Analytical Methods

3.2.1 The moisture budget equations

The moisture budget equation for the atmosphere has been derived by several authors (Spar, 1953; Palmen and Newton, 1969; Haltiner, 1971). A combination of the methods of Haltiner and Palmen and Newton is reproduced here.

Haltiner began with the continuity equation for water vapor in the atmosphere which is given as

$$\frac{\partial \rho_v}{\partial t} + \vec{\nabla} \cdot (\rho_v \vec{V}) = S, \quad (3-1)$$

where ρ_v is the density of water vapor in the air and $\vec{\nabla}$ and \vec{V} are the three-dimensional del operator and velocity in pressure coordinates. The term S represents sources or sinks of moisture in mass per unit volume per unit time.

The density of water vapor is defined as $\rho_v \equiv \rho q$, where ρ and q are the density and specific humidity of the air, respectively. If this definition is exchanged with ρ_v in Eq. (3-1) and an expansion is made of the resulting terms, one has

$$q \frac{\partial \rho}{\partial t} + \rho \frac{\partial q}{\partial t} + \rho q \vec{\nabla} \cdot \vec{V} + \rho \vec{V} \cdot \vec{\nabla} q + q \vec{V} \cdot \vec{\nabla} \rho = S. \quad (3-2)$$

By assuming an incompressible fluid (i.e., $\frac{d\rho}{dt} = 0$), Eq. (3-2) can be written

$$\rho \frac{\partial q}{\partial t} + \rho \vec{V} \cdot (q \vec{\nabla}) = S. \quad (3-3)$$

The remainder of the derivation follows that by Palmen and Newton in a slightly expanded form. By integrating Eq. (3-3) over a vertical column, assuming hydrostatic equilibrium, one has

$$\frac{1}{g} \int_{p_2}^{p_1} \frac{\partial q}{\partial t} dp + \frac{1}{g} \int_{p_2}^{p_1} \vec{\nabla}_2 \cdot (q \vec{V}_2) dp + \frac{1}{g} \int_{p_2}^{p_1} \frac{\partial (q\omega)}{\partial p} dp = R, \quad (3-4)$$

where the second term on the left-hand side (LHS) has been expanded into its horizontal and vertical components. The right-hand side (RHS) of Eq. (3-4), R , results from the integration of S and represents the effects of evaporation, precipitation, and condensation.

Integration of the third term on the LHS of Eq. (3-4) gives

$$\frac{1}{g} \int_{p_2}^{p_1} \frac{\partial q}{\partial t} dp + \frac{1}{g} \int_{p_2}^{p_1} \vec{\nabla}_2 \cdot (q \vec{V}_2) dp + \frac{1}{g} [(q\omega)_{p_1} - (q\omega)_{p_2}] = R. \quad (3-5)$$

which is the moisture budget equation for a unit column over each grid point. Equation (3-5) was integrated over an area, A , of three grid distances square. Previous researchers had used a similar procedure except that averages were taken over much larger regions, enclosing entire cyclones and their associated weather. Since convective systems are subsynoptic-scale phenomena, a smaller area was chosen in order to show the moisture budget in the region immediately surrounding storms. Upon integration, Eq. (3-5) becomes

$$\begin{aligned} \frac{1}{gA} \iint_{Ap_2}^{p_1} \frac{\partial q}{\partial t} dp dA + \frac{1}{gA} \iint_{Ap_2}^{p_1} \vec{\nabla}_2 \cdot (q \vec{V}_2) dp dA \\ + \frac{1}{gA} \int_A [(q\omega)_{p_1} - (q\omega)_{p_2}] dA = \frac{1}{A} \int_A R dA, \end{aligned} \quad (3-6)$$

where each term was divided by A , resulting in $g \text{ cm}^{-2} \text{ s}^{-1}$ as the final units.

The terms on the LHS of Eq. (3-6) are the local rate-of-change of moisture, the horizontal moisture divergence, and the net vertical boundary flux of moisture, respectively. By application of the divergence theorem, Eq. (3-6) becomes

$$\frac{1}{gA} \int_{Ap_2}^{p_1} \frac{\partial q}{\partial t} dp dA + \frac{1}{gA} \int_{Lp_2}^{p_1} q V_n dp dL + \frac{1}{gA} \int_A [(q\omega)_{p_1} - (q\omega)_{p_2}] dA = \frac{1}{A} \int_A R dA, \quad (3-7)$$

where V_n is defined by convention as positive outward and L is the length of the boundary around area A . Equation (3-7) is the final form of the moisture budget equation used in this research. For convenience, q is replaced in Eq. (3-7) by the mixing ratio which introduces only a small error.

3.2.2 Local changes

The local rate-of-change of moisture is represented by the first term on the LHS of Eq. (3-7). The evaluation of $\frac{\partial q}{\partial t}$ was performed at each grid point and level by use of centered finite differences using values of mixing ratio at times immediately adjacent to the one being considered. This operation was performed at each time except for the first and last time periods of the experiment when a forward difference and backward difference scheme was used, respectively.

The values found at each grid point were integrated with respect to pressure over an interval of 50 mb, utilizing a first order integration approximation. The method used was the trapezoidal rule which has the form $(f_1 + f_2) \frac{h}{2}$ where the f 's represent the values of $\frac{\partial q}{\partial t}$ at the adjacent pressure levels and $h = 50$ mb. For two values, this amounts to simple averaging. This process was continued for each layer and resulted in pressure-integrated values of the local change of moisture for 50-mb layers from 900-350 mb.

As stated previously, the area integral was evaluated over an area of three grid distances square, centered at each grid point. This was done by summing the eight adjacent grid point values with the point they surrounded. This value was multiplied by one grid distance squared, d^2 , which was the area over which the value at each grid point was assumed to be representative. The resultant amount was divided by the total area, $A = (3d)^2$, of the nine points and placed at the central grid point. Division by gravity completed the evaluation of the term.

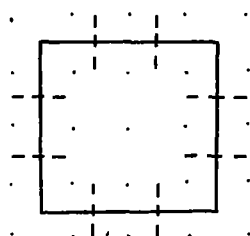
3.2.3 Vertical changes

The product of mixing ratio and vertical motion at each grid point was calculated for every 50-mb level. The net vertical boundary flux of moisture was found by subtracting the upper-level value from that of the next level below. The nine-point area-averaging routine that was described in the previous

section was utilized here. Division by A and gravity completed the evaluation of this term.

3.2.4 Horizontal changes

The initial step in evaluating the net horizontal boundary flux of moisture was to compute fields of q times the u component of velocity, and q times the v component of velocity at each grid point and level. Each of these fields was integrated separately with respect to pressure by the method described in the section concerning local changes. Using these pressure-integrated fields, the horizontal boundary flux into the area over which the local and vertical changes had been averaged was computed. This area is represented by the solid line in the schematic diagram below. Each side of the area was segmented (as shown by the dashed lines) and the flux was calculated



individually across each segment. This was done by averaging the two points on opposite sides of each segment. Each average was multiplied by the length of the segment, d , along which it was assumed constant. Care was taken in the averaging process to insure that the pressure-integrated values containing the east-west velocity component and those containing the north-south velocity component were used on their respective sides of the area boundary.

Since the net horizontal boundary flux of moisture was defined by convention as positive outward, the signs of the averaged values on the west and south sides were taken into consideration. The averages were then summed and the resultant placed at the central grid point. Evaluation of the term was completed by dividing this final value by A and gravity.

As stated previously, by use of the divergence theorem the net horizontal boundary flux can be replaced by the moisture divergence. This quantity can be expanded into two separate components, the moisture concentration due to velocity divergence of the wind, $(q\vec{V}\cdot\vec{V})$, and horizontal moisture advection, $(\vec{V}\cdot\vec{\nabla}q)$. Calculations of these two terms were made for purposes of comparison with the evaluation of the net horizontal boundary flux.

The initial step in the evaluation of $q\vec{V}\cdot\vec{V}$ was to calculate a field of divergence, using centered finite differences at every grid point. These values were multiplied by the value of q at that point. The rest of the evaluation followed the pressure and area integration method described in the section concerning local changes. Division by gravity and A completed the calculation.

Moisture advection was evaluated by first computing values of the components of $\vec{V}q$, using centered finite differences at each grid point. Values of $u\frac{\partial q}{\partial x}$ and $v\frac{\partial q}{\partial y}$ were summed for each grid point. Integrations with respect to pressure and area were performed as was described previously. Division by gravity and A completed the evaluation.

3.2.5 Combination of terms (residual)

Three-hour composites of hourly precipitation data were tabulated and plotted and analyzed manually. Values were assigned to each grid point according to the analysis. Integration with respect to area and division by A , discussed in previous sections, completed the evaluation.

3.3 Results

3.3.1 AVE III

The manner of presentation of maps and graphs shown in this report follows that used by Scott and Scoggins (1977). They related selected computed quantities of the moisture equation to MDR values at the time of convection and 3 h prior to convection in order to observe the relationships between the quantities and MDR values in convective and nonconvective areas. It should be pointed out that very little convection occurred over land during AVE III so that relationships obtained during this experiment must be considered tentative. Therefore, comparisons with the results from AVE IV can only be very general in nature. Due to extremely dry air in the upper atmosphere in AVE III, calculations were made from 900-450 mb as compared to a 900-350 mb layer used in AVE IV.

The horizontal analyses presented in the following section are at 1800 GMT on 6 February 1975, which is centered in the period of convective activity in the Gulf of Mexico. Figure (3-1) shows the surface and 700 mb features that were present at that time. Radar-observed precipitation, indicated by a 3-h composite of MDR values, is shown in Fig. (3-2) (see Appendix for all AVE III MDR charts).

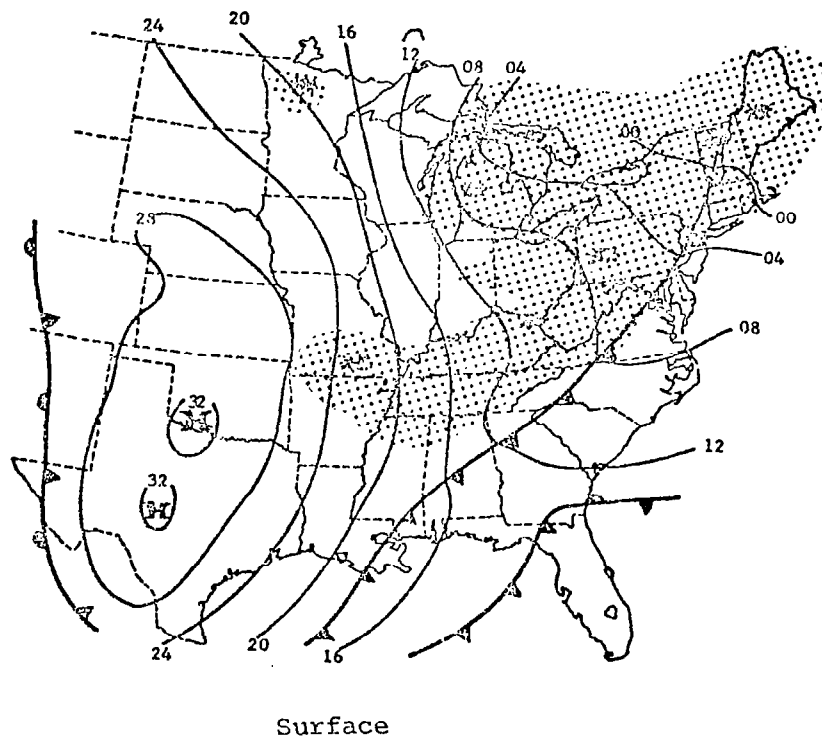
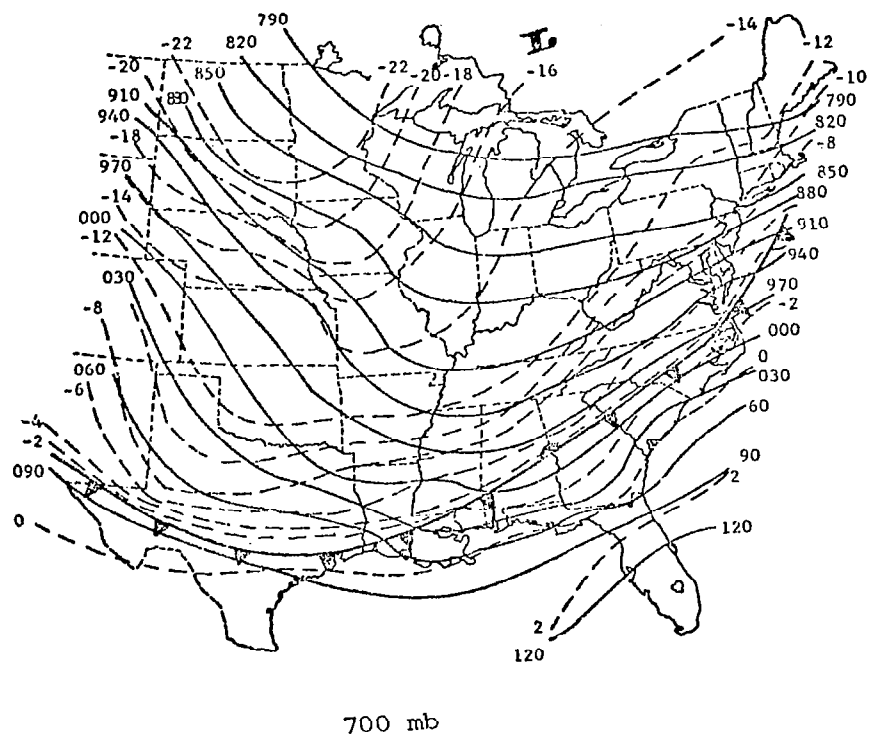


Fig. 3-1. Synoptic charts for 1800 GMT, 6 February 1975.

Fig. 3-2. Three-hour composite of MDR data at 1800 GMT on 6 February 1975.

3.3.1.1 Local changes

Vertical profiles of the local rate-of-change of moisture related to MDR data are shown in Fig. (3-3). In the areas of precipitation (MDR 2), moisture was lost locally in the lower 100 mb. The maximum loss was found in the lowest layer evaluated (900-850 mb). Above 800 mb, there was a gain of moisture locally, reaching a maximum in the 50-mb layer centered on 725 mb.

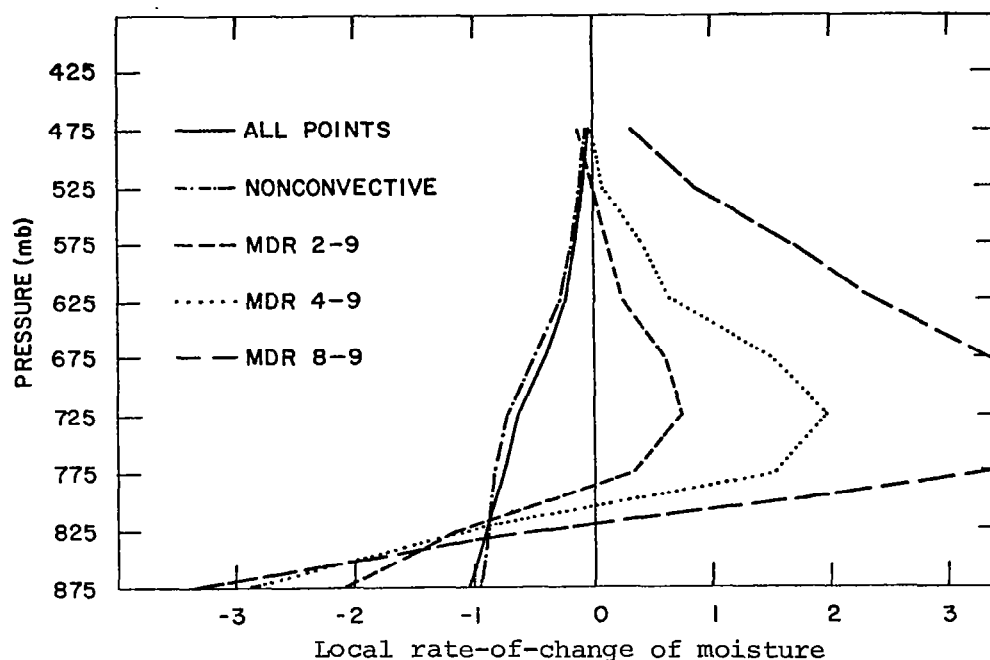


Fig. 3-3. Vertical profiles of the local rate-of-change of moisture ($10^{-6} \text{ g cm}^{-2} \text{ s}^{-1}$) as function of MDR values.

The profile of the nonconvective precipitation areas was markedly different from those just discussed. In these areas, local drying was calculated in all layers in the troposphere.

Comparisons made between this term and MDR data lagged by three hours (figure not shown) showed little change in the profiles of the non-convective regions of precipitation. However, in the areas of heavier rainfall, all profiles were shifted in the positive direction indicating that most of the troposphere was becoming more moist three hours prior to thunderstorm formation.

3.3.1.2 Vertical moisture divergence

Vertical profiles of the vertical moisture divergence appear in Fig. (3-4). The convective rainfall areas were characterized by strong

vertical divergence below 700 mb and equally strong convergence above. Since, in this situation, upward vertical motion usually increased throughout the layer below 700 mb, it would be expected that each 50-mb layer below 700 mb would be losing moisture to the next one above (assuming constant moisture through the layer). This loss of moisture would be registered as a gain higher up in the atmosphere as vertical motion decreased above the level of nondivergence.

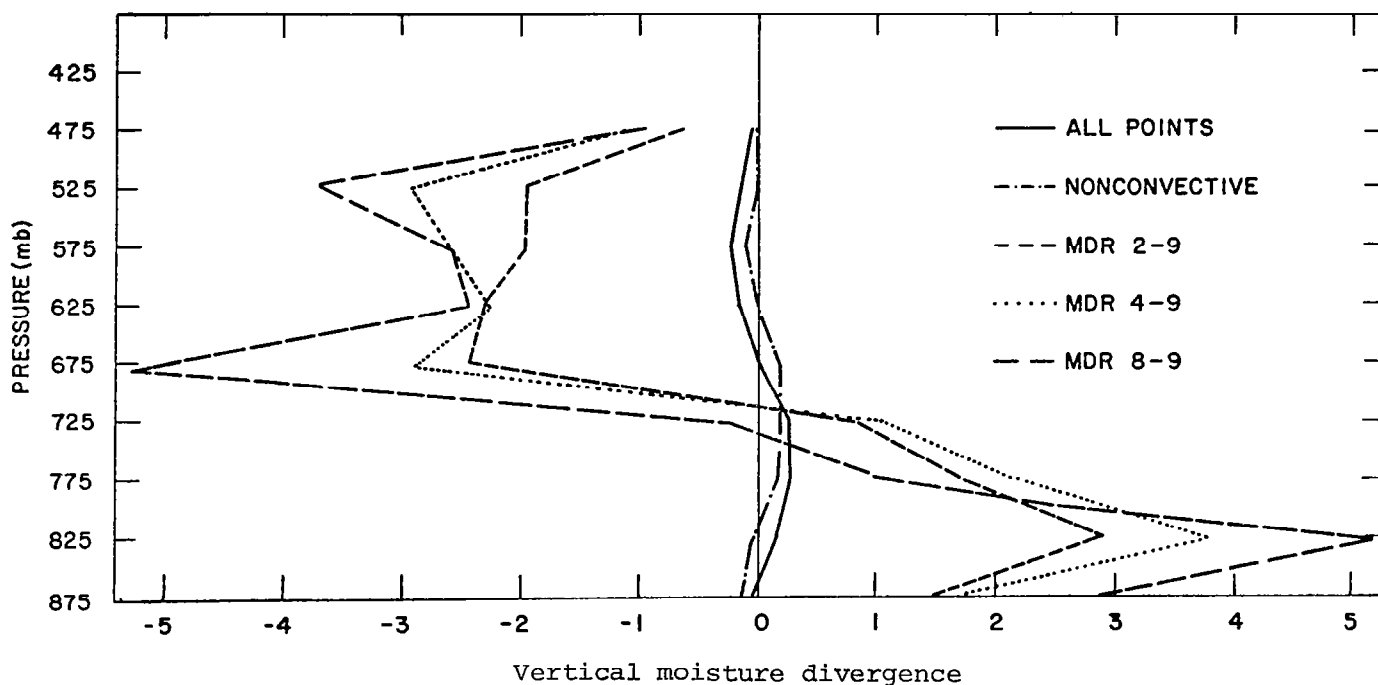
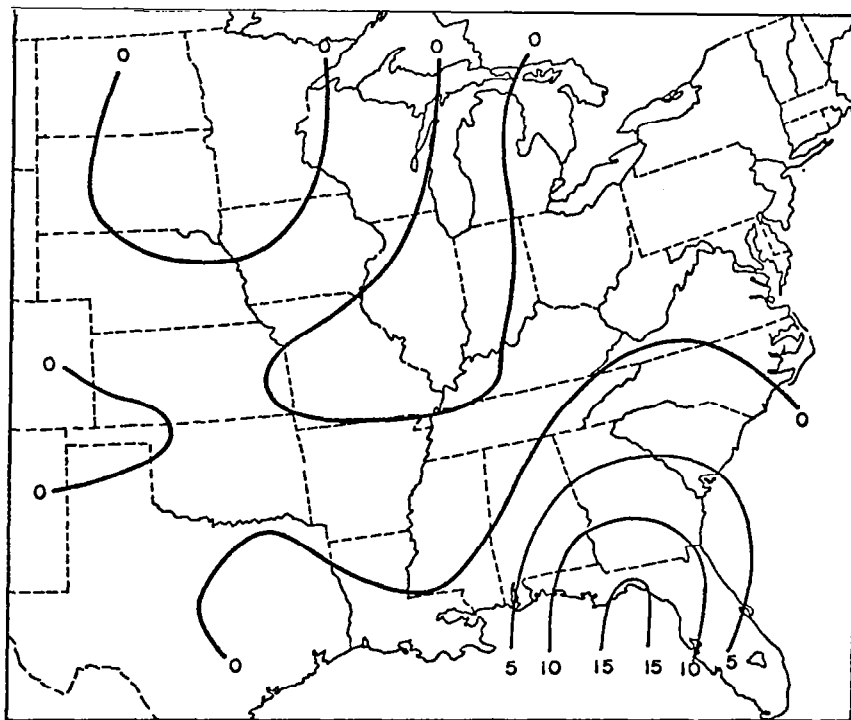


Fig. 3-4. Vertical profiles of vertical moisture divergence ($10^{-6} \text{ g cm}^{-2} \text{ s}^{-1}$) as function of MDR values.

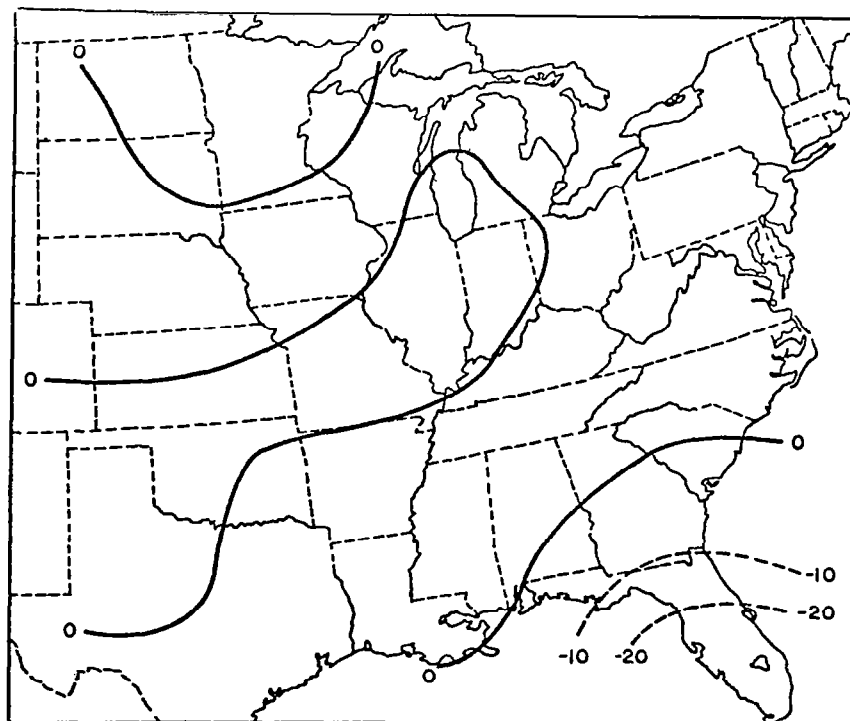
The profile for the nonconvective areas show values near zero throughout the atmosphere. This result was expected since any large vertical convergence or divergence in any layer would indicate the presence of strong vertical motion likely associated with much heavier rainfall or subsidence in storm areas.

Spatial fields of the vertical moisture divergence in the 900-to-750-mb, and 750-to-500-mb layers at 1800 GMT appear in Fig. (3-5). In comparison with Fig. (3-2), it is easily seen that this term was large only in the areas near the higher MDR values and weak in the nonconvective areas. This supports what was found in the profiles of Fig. (3-4).

In making comparisons between this term and MDR data lagged by three hours (figure not shown), it was found that the nonconvective profiles were essentially unchanged. The regions of heavier precipitation also showed the



(a) 900 - 750 mb



(b) 750 - 500 mb

Fig. 3-5. Analyses of vertical moisture divergence at 1800 GMT on 6 February 1975 ($10^{-6} \text{ g cm}^{-2} \text{ s}^{-1}$) within two layers.

same general pattern, but values were less than the "no lag" case, especially in the areas of the strongest storms ($MDR \geq 8$). This indicates that strong vertical moisture divergence occurred in the areas where heavy rain fell three hours later, but the largest values were found at the time of the storms. It also suggests that the term could be used to indicate the positions of future development or continued maintenance of storms.

3.3.1.3 Horizontal moisture divergence

Vertical profiles of horizontal moisture divergence as function of MDR values appear in Fig. (3-6). Strong horizontal convergence of moisture occurred in association with the heavier precipitation areas below 650 mb. Maximum convergence occurred in the 50-mb layer from 800 to 750 mb. Positive moisture divergence was present above 600 mb. The nonconvective areas were characterized by small divergence below 700 mb with no contribution from this term above this level.

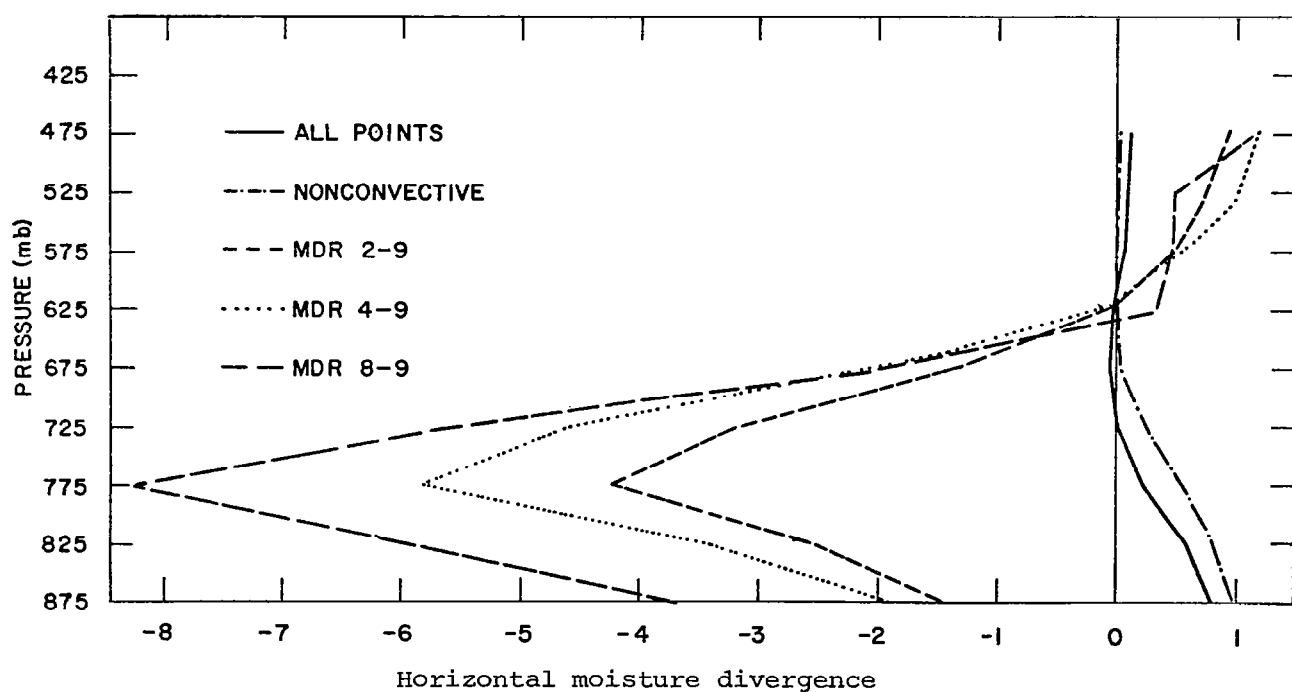


Fig. 3-6. Vertical profiles of horizontal moisture divergence ($10^{-6} \text{ g cm}^{-2} \text{ s}^{-1}$) as function of MDR values.

By splitting the horizontal moisture divergence into its two components, it can be seen from their vertical profiles that both moisture concentration due to wind divergence (Fig. 3-7) and moisture advection (Fig. 3-8) contributed heavily to the large concentration of moisture in the lower atmosphere.

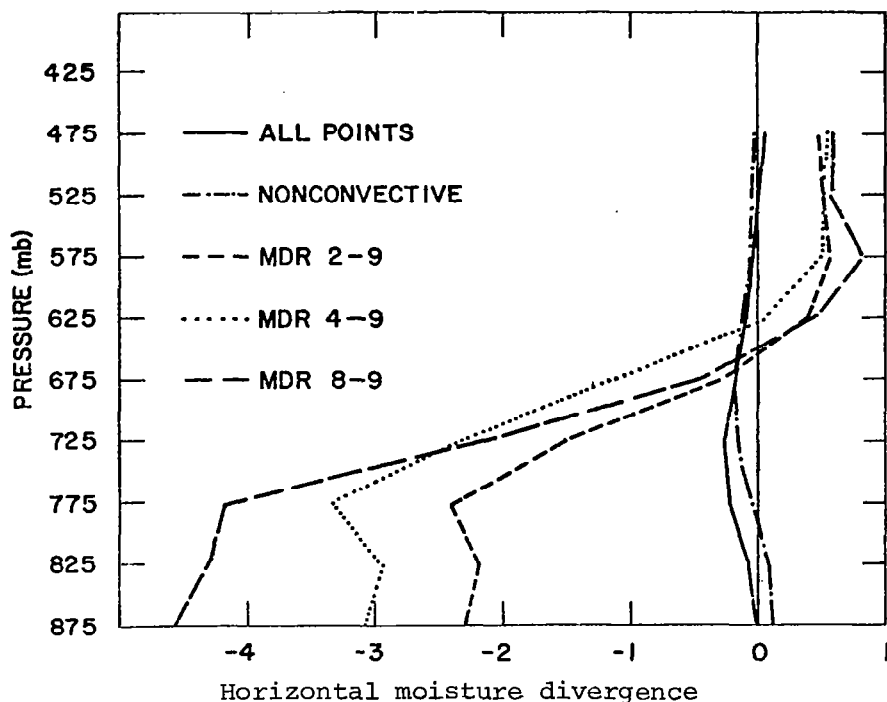


Fig. 3-7. Vertical profiles of moisture concentration due to wind divergence ($10^{-6} \text{ g cm}^{-2} \text{ s}^{-1}$) as function of MDR values.

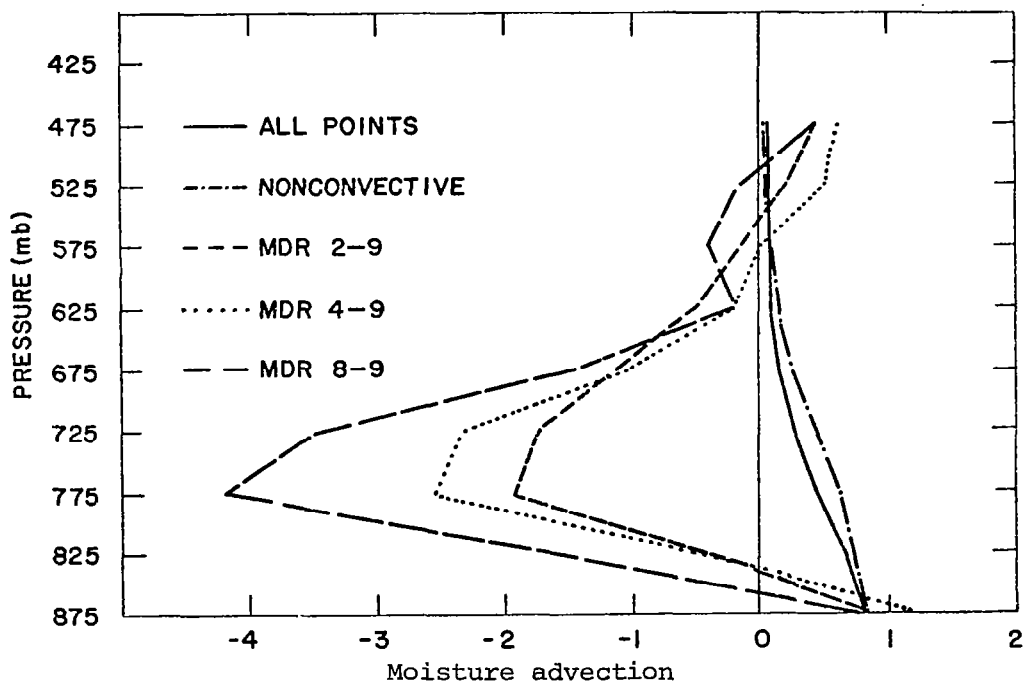


Fig. 3-8. Vertical profiles of moisture advection ($10^{-6} \text{ g cm}^{-2} \text{ s}^{-1}$) as function of MDR values.

Both components were strongest in the 800-to-750-mb layer which accounts for the large amount of convergence at that level shown in Fig. (3-6).

Horizontal moisture divergence in the lower levels of the nonconvective areas was caused by moisture advection. Since only small velocity divergence (positive or negative) would be expected in these areas, any horizontal accumulation of moisture could only come from advection.

Analyses of the horizontal moisture divergence in the layers from 900-750 mb and 750-500 mb at 1800 GMT on 6 February 1975 are shown in Fig. (3-9). Referring to Fig. (3-2), it is seen that only the regions where $MDR \geq 2$ were associated with strong moisture divergence.

Values of this term were much larger in the heavier rainfall areas when the MDR data were lagged by three hours. This indicates that horizontal moisture divergence was stronger just ahead of the storm areas which, like vertical moisture divergence, gives an indication of the position for future development or continued maintenance of storms.

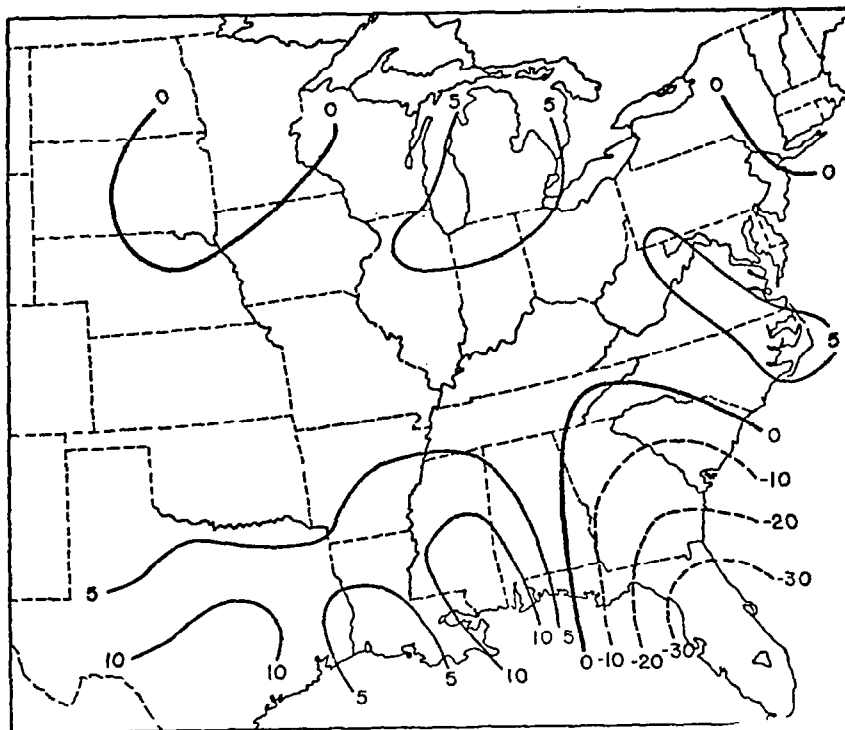
3.3.1.4 Residual of moisture

Vertical profiles of the residual of moisture during the AVE III experiment are shown in Fig. (3-10). All areas showed a net loss of moisture from the environment throughout the atmosphere. This means that condensation and precipitation were greater than evaporation of clouds during the AVE III experiment. The difference was larger in the heavy rainfall areas. Very small losses were found in the nonconvective areas.

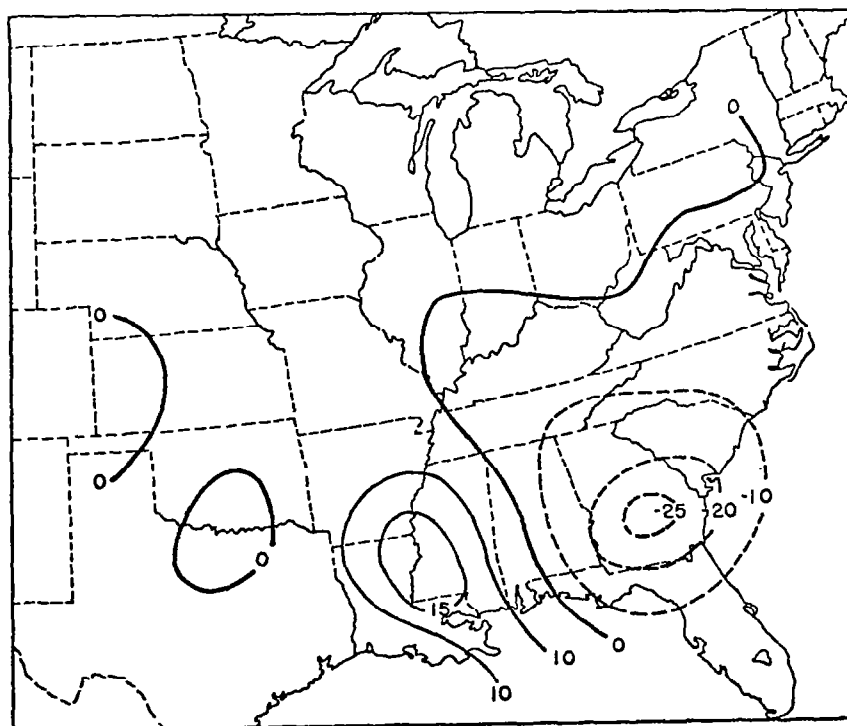
The analysis of the residual of moisture in the layer from 900-450 mb at 1800 GMT on 6 February 1975, appears in Fig. (3-11). Large values of negative residual were found in the areas of the heaviest rainfall (see Fig. (3-2)). The values were much larger than those found in the nonconvective precipitation areas as shown in Fig. (3-10).

Comparison of the residual of moisture and MDR data lagged by three hours (figure not shown) showed a closer balance of the terms in the moisture budget. As stated earlier, areas of $MDR \geq 2$ experienced decreases in the local rate-of-change of moisture term between the 3-h lag and zero lag so that the larger local rate-of-change term at a 3-h lag resulted in a smaller residual.

In an attempt to account for a portion of the large residual, precipitation analyses were made from hourly precipitation data collected via recording raingages. The analysis for 1800 GMT on 6 February is shown in



(a) 900 - 750 mb



(b) 750 - 500 mb

Fig. 3-9. Analyses of horizontal moisture divergence at 1800 GMT on 6 February 1975 ($10^{-6} \text{ g cm}^{-2} \text{ s}^{-1}$).

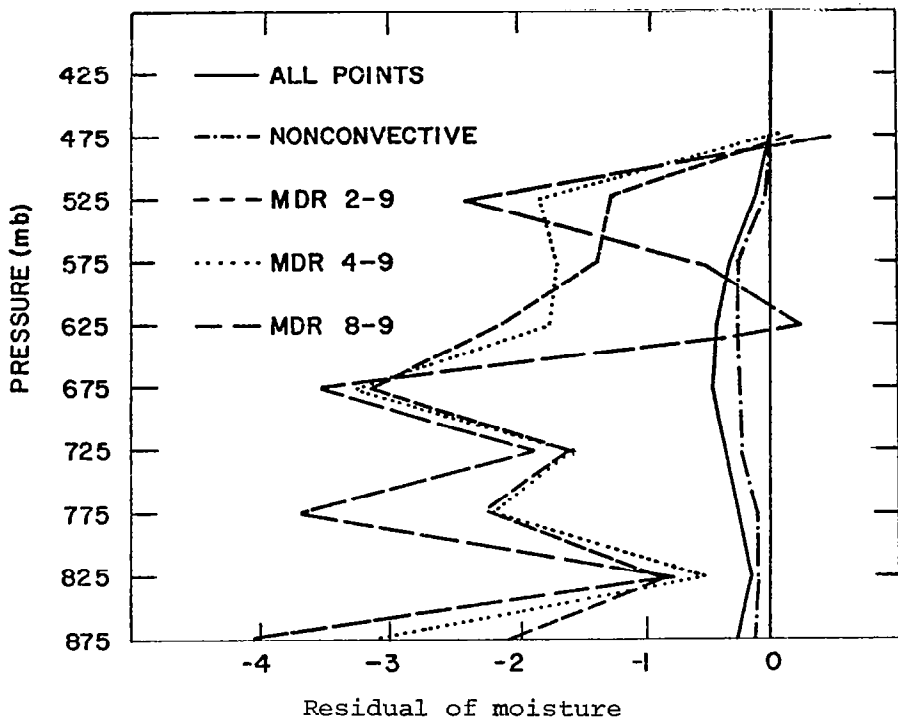


Fig. 3-10. Vertical profiles of the residual of moisture ($10^{-6} \text{ g cm}^{-2} \text{ s}^{-1}$) as function of MDR values.

Fig. (3-12). The heavy rainfall area over Florida coincides well with the region of large negative residual in the same area shown in Fig. (3-11). It must be pointed out that large rainfall occurred in the Gulf of Mexico in association with the strong convection and was not measured. Thus, the precipitation analysis is not complete in that area. The data collection was very good in the nonconvective regions but the amounts were very light. The residual was also small in these areas, comparing favorably to the precipitation analysis.

3.3.2 Comparisons between AVE III and AVE IV

The discussion in this section relates the results of this report on AVE III with those concerning AVE IV performed by Scott and Scoggins (1977).

Comparisons between AVE III and AVE IV are difficult to make since the two experiments represent entirely different synoptic systems. AVE III was characterized, for the most part, by light rain and snow over much of the northern United States with a small area of convection across the northern Gulf of Mexico. Conversely, two strong lines of convective storms were in existence during the AVE IV experiment. Since the data coverage in the heavy rainfall areas of AVE III is poorer than in AVE IV, comparisons are made relative only to the general patterns present and not to actual computed values of the various terms.

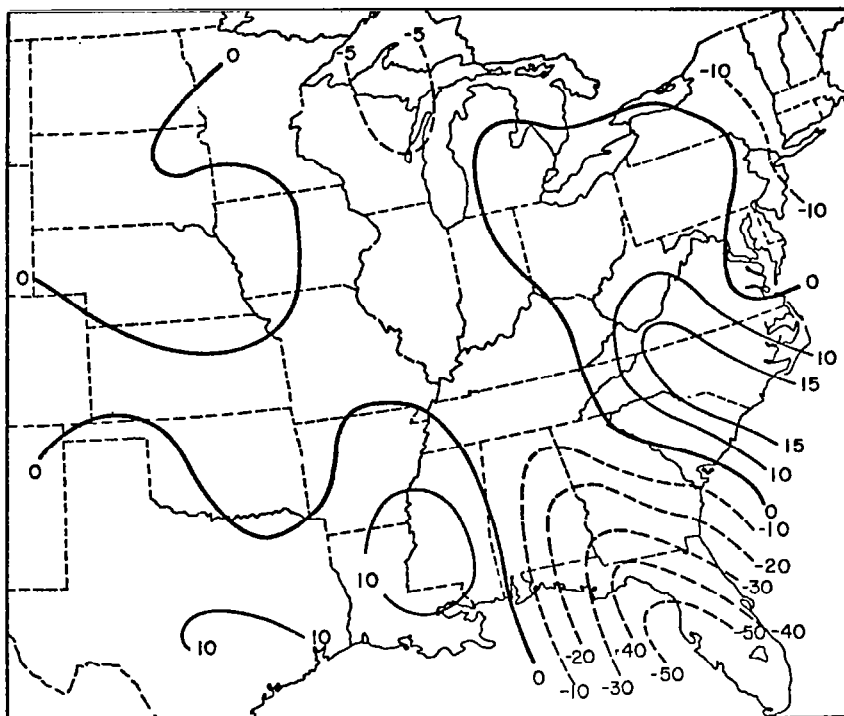


Fig. 3-11. Analysis of the residual of moisture in the layer from 900-450 mb at 1800 GMT on 6 February 1975 ($10^{-6} \text{ g cm}^{-2} \text{ s}^{-1}$).

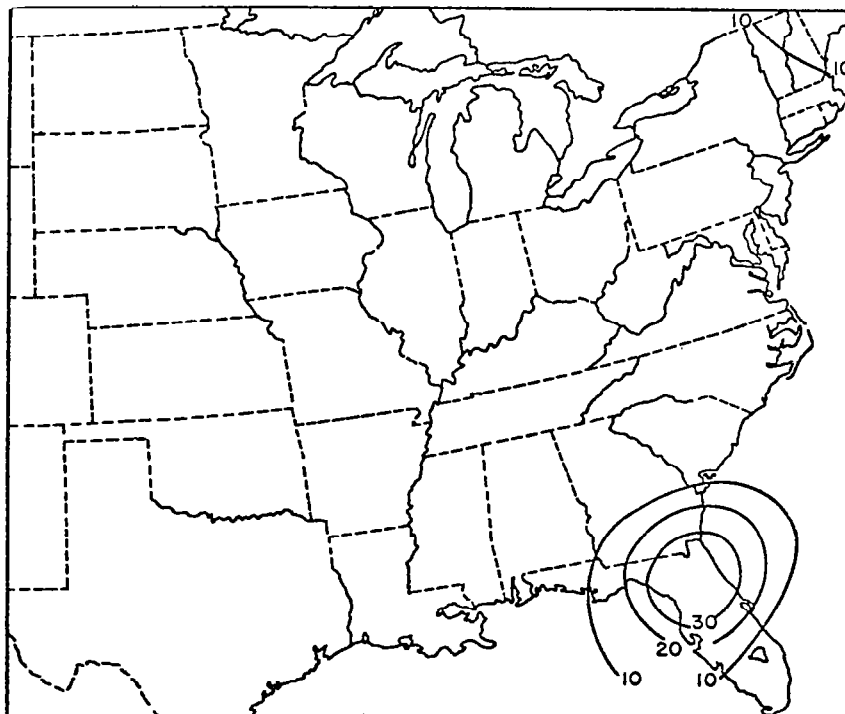


Fig. 3-12. Three-hour composite of precipitation flux at 1800 GMT on 6 February 1975 obtained from rainfall rates ($10^{-6} \text{ g cm}^{-2} \text{ s}^{-1}$).

The most noticeable similarity between the two experiments was in the convective rainfall areas. The vertical moisture divergence (called the net vertical boundary flux of moisture in AVE IV) indicated divergence in the lower layers and convergence aloft in both experiments. The horizontal moisture divergence (termed the net horizontal boundary flux of moisture in AVE IV) showed strong convergence through a deep layer near the surface and small divergence higher up during AVE III and AVE IV. Thus, strong horizontal convergence of moisture occurred at the surface where it was transported vertically upward and then accumulated in the middle layers of the convective regions during both experiments.

The two separate components of the horizontal moisture divergence shows the moisture concentration due to wind divergence to be very nearly the same in both experiments. Large negative values were found in a deep lower layer with small positive values aloft. Moisture advection, however, was strikingly different in each experiment. In the convective region of AVE III, the horizontal moisture advection term was strongly negative in the middle layers (positive moisture advection). Contrary to this, data collected during AVE IV indicated positive moisture advection in the same layers. This can be partially explained by the differences in the moisture content of the regions surrounding the convective storms. Winds at 700 mb blowing into the thunderstorm areas during AVE IV were from the west and southwest and, for the most part, were relatively dry. Convection in AVE III, on the other hand, was located in the Gulf of Mexico. Thus, the air being advected into the system had a higher moisture content, particularly in the middle troposphere.

The local rate-of-change of moisture was also different in both experiments. Whereas in AVE IV the term was negative in lower layers and negligible above, the local rate-of-change of moisture was negative near the surface but positive in a deep layer aloft during AVE III. The different moisture advection distributions previously described were primarily responsible for explaining the differences in the local rate-of-change profiles.

The pattern of the residual of moisture was also very similar during both experiments. Large negative values of the term were present throughout most of the atmosphere. Precipitation analyses were able to account for a large portion of the residual in both AVEs.

Contrary to all of the above similarities, results for the nonconvective areas were seldom the same when comparing the two experiments. The magnitude of the terms in these areas were generally very small and the signs were

often different between AVE III and AVE IV and followed no noticeable pattern. Since the convective regions were so strikingly similar and the non-convective areas were not, it is possible that the moisture budget method that was used in evaluating AVE III and AVE IV is applicable only in convective or heavy rainfall areas. Regions of light or no precipitation accumulate too little moisture to obtain results which are not affected strongly by possible errors in the data or computations.

3.4 Conclusions

1. Large amounts of moisture were accumulated in the convective areas of AVE III, as shown by horizontal moisture divergence. This was accomplished through both horizontal wind divergence and moisture advection. Much of this moisture was then transported vertically as indicated by strong vertical moisture divergence.

2. Although an increase in moisture content was found locally in the convective areas, a large negative residual remained. This was balanced, in part, by precipitation that fell during the experiment measured by hourly precipitation totals.

3. Comparisons made between computed moisture quantities and MDR values lagged by three hours revealed larger values in the preconvective areas in all terms. This indicated the position of future development or continued maintenance of storms.

4. Results from AVE III and AVE IV closely compare in the convective areas of both experiments. Terms in the nonconvective areas were so small in both experiments that only systems which transport large amounts of moisture can be evaluated accurately using the moisture budget analysis presented here.

3.5 References

- Haltiner, George J., 1971: Numerical Weather Prediction, Wiley, 161-163.
- Palmen, E., and C. W. Newton, 1969: Atmospheric Circulation Systems, Academic Press, Chapters 12 and 13.
- Scott, R. W., and J. R. Scoggins, 1977: The moisture budget in relation to convection. NASA CR-2817, NASA Marshall Space Flight Center, Huntsville, Alabama, 88 pp.
- Spar, J., 1953: A suggested technique for quantitative precipitation forecasting. Mon. Wea. Rev., 81, 217-221.

ATMOSPHERIC ENERGETICS DURING THE AVE III EXPERIMENT

by

Henry E. Fuelberg*
Department of Meteorology
Texas A&M University
College Station, Texas 77843

ABSTRACT

An energy budget and transformation study was conducted for AVE III (a wintertime case) as was done previously for AVE IV (a springtime case). The same computational procedures were employed, and although the synoptic conditions and extent of convective activity were different, similar results were found in both experiments.

Intense energy conversion and transport processes occurred during the AVE III period. The generation of energy by cross-contour flow was large. Much of this generated energy was transported horizontally out of the area, while smaller amounts were transferred to subgrid scales and even smaller amounts used to increase the kinetic energy of the volume. Horizontal and vertical transports were the largest components of the energy budget, while diabatic heating effects were small. Rather large changes in the energy budget occurred during the AVE III period. These changes occurred in all budget terms.

*Assistant Professor of Meteorology, St. Louis University, St. Louis, MO

4.1 Introduction

Understanding atmospheric energetics of all scales of motion is important since energy conversion and transport are associated with weather phenomena of all scales. Interaction between the various scales of motion is an especially important consideration. The kinetic energy balance of middle-latitude cyclones has been described in several recent articles (e.g., Chen and Bosart, 1977; Smith, 1973a and b; Vincent and Chang, 1975; Ward and Smith, 1976; Petterssen and Smebye, 1971). Kung and Baker (1975) described the kinetic energy budgets of eleven categories of midlatitude flow by computing budgets twice daily over a five-year period. These and other studies have shown that cyclones are centers of major energy conversion and transport. The energetics of anticyclones is considerably different from that of cyclones and much less intense. The environment of intense convection also is characterized by major energy activity that is related to the life cycle and intensity of the storms (Fuelberg, 1977; Fuelberg and Scoggins, 1978).

Energy processes associated with many types of synoptic conditions have not been described in detail. In addition, most previous studies have relied on rawinsonde data at the standard 12-h intervals. This study describes budgets of kinetic, internal, and potential energy during a 36-h period when a pronounced upper-level trough, not associated with a deep surface cyclone, traversed the eastern United States. Rawinsonde data at 3- and 6-h intervals permit the temporal resolution of many features that ordinarily cannot be described.

4.2 Energy Equations

The energy equations used in this study have been described by Fuelberg (1977) and West (1973).

The kinetic energy equation is

$$\begin{aligned}
 \frac{\partial K}{\partial t} = & - \frac{1}{g} \iint_{Ap} \vec{V} \cdot \vec{\nabla} \phi \, dp \, dA'' - \frac{1}{g} \iint_{Ap} \vec{V} \cdot \vec{k} \, \vec{V} \, dp \, dA'' \\
 (a) \quad & (b) \quad (c) \\
 & - \frac{1}{g} \iint_{Ap} \frac{\partial \omega k}{\partial p} \, dp \, dA'' + \frac{1}{g} \iint_{Ap} \vec{V} \cdot \vec{F} \, dp \, dA'' \quad (4-1) \\
 & (d) \quad (e)
 \end{aligned}$$

where $k = 1/2(u^2 + v^2)$ is horizontal kinetic energy per unit mass,

$$K = \frac{1}{g} \iint_{Ap} k \, dp dA'',$$

\vec{V} is the horizontal wind vector,

$\phi = gz$ is geopotential height,

p is pressure,

g is acceleration due to gravity,

A'' is a dummy variable of integration corresponding to area,

$\omega = \frac{dp}{dt}$ is vertical motion in isobaric coordinates, and

\vec{F} is frictional force.

Local changes in kinetic energy for a fixed volume, term (4-1a), are due to four processes. Term (4-1b) represents kinetic energy generation (Kung, 1966) or conversion of potential to kinetic energy (Smith, 1970) due to cross-contour flow. Terms (4-1c) and (4-1d) are horizontal and vertical flux divergence of kinetic energy that represent interaction of the limited volume with the surrounding atmosphere. Term (4-1e) conceptually represents primarily frictional processes, but when computed as a residual in (4-1), also represents a transfer of energy between grid and subgrid scales of motion due mostly to unresolvable eddy processes (Smith and Adhikary, 1974; Kung and Smith, 1974). This term is often called the dissipation term and is denoted by D .

The sum of internal and gravitational potential energy is given by

$$\begin{aligned} \frac{1}{g} \iint_{Ap} \frac{\partial}{\partial t} (c_v T) \, dp dA'' + \frac{1}{g} \iint_{Ap} \frac{\partial \phi}{\partial t} \, dp dA'' &= \frac{1}{g} \iint_{Ap} \frac{dH}{dt} \, dp dA'' + \frac{1}{g} \iint_{Ap} \vec{V} \cdot \vec{V} \phi \cdot dp dA'' \\ &\quad - \left[\frac{1}{g} \iint_{Ap} \vec{V} \cdot (c_v T \vec{V}) \, dp dA'' + \frac{1}{g} \iint_{Ap} \vec{V} \cdot \phi \vec{V} \, dp dA'' \right] \\ &\quad - \left[\frac{1}{g} \iint_{Ap} \frac{\partial}{\partial p} (c_v T \omega) \, dp dA'' + \frac{1}{g} \iint_{Ap} \frac{\partial \phi \omega}{\partial p} \, dp dA'' \right] \\ &\quad - \frac{R}{g} \iint_{Ap} \vec{V}_3 \cdot T \vec{V}_3 \, dp dA'', \end{aligned} \quad (4-2)$$

where c_v is specific heat,

T is temperature,

$\frac{dH}{dt}$ is diabatic heating per unit mass, and

R is the gas constant.

Local changes of internal and potential energy, term (4-2a), are due to five component processes. Term (4-2b) represents generation of internal energy due to diabatic effects. Term (4-2c) is identical to (4-1b) but with opposite sign and represents conversion between available potential and kinetic energy. Terms (4-2d) and (4-2e) are horizontal and vertical flux divergence of internal and potential energy. Term (4-2f) defines pressure work at the boundary of the limited volume under consideration.

4.3 Analytical Procedures

Computational procedures used in this study are similar to those of Fuelberg (1977). Surface and rawinsonde data were interpolated from the randomly spaced stations on to a grid with a spacing of 158 km. An objective analysis scheme developed by Barnes (1964) was used for the interpolation. Interpolated fields were smoothed using a mild filter developed by Shuman (1957). Terms in (4-1) and (4-2) were computed on grid points at the surface and at 50-mb intervals from 900 to 100 mb. Values were then integrated over 100-mb layers. Kinematic values of vertical motion were used. Terrain-induced vertical motion was included, and the values were adjusted to those obtained from the adiabatic method at 100 mb by using a technique presented by O'Brien (1970). Diabatic heating, appearing in term (4-2b), was computed from the thermodynamic equation

$$\frac{dH}{dt} = c_p \frac{\partial T}{\partial t} + c_p \vec{V} \cdot \vec{\nabla} T + (c_p \frac{\partial T}{\partial p} - \alpha) \omega, \quad (4-3)$$

where c_p is specific heat and α is specific volume.

4.4 Results

4.4.1 Composite kinetic energy budget

The average energy budget for the entire AVE III experiment describes energetics of the large-scale flow. The kinetic energy budget averaged for all nine observation times is given in Table 4.1. Since the upper-level trough axis remained west of the center of the area for more than half of the observation times, the budget presented here generally describes conditions east of the trough line. A striking feature is large generation of kinetic energy due to cross-contour flow; the vertical total is 70.5 W m^{-2} . Largest generation occurs near the level of the jet stream while a secondary maximum occurs near the surface. A relative minimum is located in the 900- to 700-mb

layer. Much of the generated energy is transported out of the AVE area by horizontal flux divergence. This process also is a maximum near jet-stream level.

Negative dissipation, that is transfer of kinetic energy from grid to subgrid scales of motion, is an additional, but secondary, sink of the generated energy. The vertical profile of dissipation roughly parallels that of the generation term.

Table 4.1. Average kinetic energy budget for the entire AVE III experiment. The AVE area is $49.0 \times 10^{11} \text{ m}^2$. All nine observation times are included.

Pressure Layer	K	$\frac{\partial K}{\partial t}$	$\vec{V} \cdot k \vec{V}$	$\frac{\partial \omega k}{\partial p}$	$-\vec{V} \cdot \vec{V} \phi$	D
mb	10^5 J m^{-2}	W m^{-2}	W m^{-2}	W m^{-2}	W m^{-2}	W m^{-2}
200-100	9.3	0.4	13.0	-0.9	19.3	-6.8
300-200	10.5	1.1	12.6	-0.3	20.1	-6.7
400-300	8.5	1.4	8.2	-0.5	12.6	-3.5
500-400	5.9	0.9	5.3	0.0	7.0	-0.8
600-500	3.9	0.8	2.4	0.4	4.0	-0.4
700-600	2.5	0.3	0.4	0.7	2.2	-0.8
800-700	1.5	0.0	0.2	0.3	1.4	-0.9
900-800	0.8	0.1	0.5	-0.1	1.4	-0.9
sfc-900	0.3	0.0	0.2	-0.1	2.5	-2.4
Vertical total	43.2	5.0	42.8	-0.5	70.5	-23.2

Vertical transport of kinetic energy is relatively small during the AVE III experiment. Vertical flux convergence is evident above 400 mb and below 800 mb with flux divergence occurring in the middle troposphere.

Very little of the generated energy is used to increase the kinetic energy content of the volume because most is transported out of the area

or dissipated into smaller scales of motion. The vertical total of term $\frac{\partial K}{\partial t}$ is 5.0 W m^{-2} which is only 7.1% as large as $-\vec{V} \cdot \vec{\nabla} \phi$.

Random errors in input data and truncation error lead to errors in computed terms of the kinetic energy equation, but such errors are not thought to affect the trends of results or their interpretation in most situations (Vincent and Chang, 1975; Kornegay and Vincent, 1976; Ward and Smith, 1976). Since wind speeds associated with the jet stream were very high during AVE III, computed winds were derived from sonde elevation angles that were low. The accuracy of such winds is less than when sondes remain high on the horizon (Fuelberg, 1974). To minimize this problem, horizontal and vertical smoothing described in the procedures section of this report were used. These error reduction procedures appear successful since spatial fields of energy terms show reasonable continuity with synoptic map features.

A comparison of the average kinetic energy budget for the AVE III experiment with Eulerian budgets of previous investigators reveals some features that are similar to budgets obtained for the different synoptic conditions but many features that are dissimilar (Table 4.2). Average kinetic energy during the AVE III period is much greater than reported for previous studies. As stated earlier, wind speeds as large as 90 m s^{-1} were observed.

An especially interesting feature is large generation of kinetic energy. The value of 70.5 W m^{-2} is much greater than has been reported previously for short waves with west-east extent of about 2000 km (Ward and Smith, 1976), and for the vicinity of mature cyclones associated with intermediate waves (Kung and Smith, 1974). It is noteworthy that such large generation of kinetic energy is observed during the AVE III experiment even though a vigorous surface cyclone is not present in the vicinity. Slight cross-contour flow can produce large generation in the present study because wind speed and height gradients are both very large. Chen and Bosart (1977) reported a value of 64.6 W m^{-2} in the vicinity of a mature cyclone using a quasi-Lagrangian budget approach, but no values of K were given for comparison. Large generation of kinetic energy also occurred in the vicinity of a mature squall line (Fuelberg, 1977; Fuelberg and Scoggins, 1978). Although wind speeds for the squall line case were much smaller than observed during the AVE III experiment, cross-contour flow on synoptic maps was much more noticeable during the squall line of the AVE IV experiment than during AVE III. The

Table 4.2. The average AVE III kinetic energy budget compared with previous results.

Author	Data	Layer	K 10^5 J m^{-2}	$\frac{\partial K}{\partial t}$ W m^{-2}	$\vec{\nabla} \cdot \mathbf{k} \vec{V}$ W m^{-2}	$\frac{\partial \omega k}{\partial p}$ W m^{-2}	$-\vec{\nabla} \cdot \vec{\nabla} \phi$ W m^{-2}	D W m^{-2}
Fuelberg (1977)	Entire AVE IV experiment, area is $49.0 \times 10^{11} \text{ m}^2$	Sfc-100 mb	19.8	-4.0	1.6	-0.1	-4.0	1.5
	Squall line at peak intensity, area is $12.2 \times 10^{11} \text{ m}^2$	Sfc-100 mb	25.5	-6.1	43.9	-0.1	52.2	-14.5
Kung and Smith (1974)	Average mature cyclone vicinity, area is $7.5 \times 10^{11} \text{ m}^2$	Sfc-tropopause	--	14.0	-24.4	0.5	27.4	-37.3
Kung and Baker (1975)	Open cyclonic waves at 500 mb with a cyclone at the surface (283 synoptic cases), area is $71.5 \times 10^{11} \text{ m}^2$	Sfc-100 mb	15.9	0.5	3.3	0.0	9.4	-5.7
	Open cyclonic wave at 500 mb, not cyclonic at surface (344 synoptic cases) area is $71.5 \times 10^{11} \text{ m}^2$	Sfc-100 mb	16.4	0.7	4.9	0.0	7.2	-1.6
Ward and Smith (1976)	Short wave development area is $134.0 \times 10^{11} \text{ m}^2$	Sfc-100 mb	19.6	0.5	-5.2	0.0	-4.4	-0.3
Present Study	AVE III, area is $49.0 \times 10^{11} \text{ m}^2$	Sfc-100 mb	43.2	5.0	42.8	-0.5	70.5	-23.2

budgets for open cyclonic waves presented by Kung and Baker (1975) are an average of several hundred synoptic cases so that details of individual intense storms are not presented.

Large horizontal flux divergence of kinetic energy distinguishes the AVE III situation from previously computed budgets of short waves (Ward and Smith, 1976) as well as in the vicinity of a mature surface cyclone associated with an intermediate wave (Kung and Smith, 1974) where flux convergence has been indicated. Horizontal flux divergence is associated with the average open cyclone at 500 mb (Kung and Baker, 1975), but values are small, probably because of the averaging procedure. Similarity with the AVE IV squall line case (Fuelberg, 1977; Fuelberg and Scoggins, 1978) is again noted; 60% of the generated energy is exported during AVE III while 84% is exported in the vicinity of the squall line.

Dissipation of kinetic energy to subgrid scales of motion consumes about 33% of the generated energy in the present study. This value is similar to that of an intense squall line (Fuelberg, 1977) and to that of open cyclonic waves (Kung and Baker, 1975), but quite different from that observed near a mature cyclone (Kung and Smith, 1974) where more kinetic energy was dissipated than was generated. Dissipation played a minor role in the kinetic energy budget for short waves (Ward and Smith, 1976).

Positive values of $\frac{\partial K}{\partial t}$ are found during the AVE III period and in previous studies involving upper-level troughs and surface cyclones. However, negative values were associated with the squall line case. Vertical flux of kinetic energy in the entire vertical column of the atmosphere is a small component of the overall budget for all studies shown in Table 4.2.

4.4.2 Composite internal and potential energy budget

Transport of internal and potential energy, rather than generation by diabatic effects or cross-contour flow, is the major energy process during the AVE III experiment (Table 4.3). Generation of internal energy by diabatic effects and conversion of available potential energy to kinetic energy by cross-contour flow are at least an order of magnitude smaller than the horizontal boundary term. Horizontal flux divergence of internal and potential energy occurs below 800 mb while flux convergence occurs at higher levels. Vertical flux convergence occurs near the surface and above 200 mb, but flux divergence is seen in most intervening layers. The boundary work term is much smaller than the two flux divergence terms. A local decrease of internal and potential energy is the net result of the five component processes just described.

A residual was computed to balance the equation of internal and potential energy. Values were sometimes as large as the remaining terms in the equation. The large residual is due partially to errors in input data, especially wind data at high altitudes, but is also due to an inability to resolve all of the energy processes with the available input data and computational procedures.

Table 4.3. Average combined internal and potential energy budget for the entire AVE III experiment. The AVE area is $49.0 \times 10^{11} \text{m}^2$. All nine observation times are included.

Pressure Layer mb	$\frac{\partial}{\partial t}(c_v T) + \frac{\partial \phi}{\partial t}$ W m^{-2}	$\frac{dH}{dt}$ W m^{-2}	$\vec{V} \cdot \vec{\nabla} \phi$ W m^{-2}	$\vec{\nabla} \cdot (c_v T \vec{V}) + \vec{\nabla} \cdot \phi \vec{V}$ W m^{-2}	$\frac{\partial}{\partial p}(c_v T \omega) + \frac{\partial}{\partial p}(\phi \omega)$ W m^{-2}	$\vec{\nabla}_3 \cdot (RT \vec{\nabla}_3)$ W m^{-2}
200-100	-3.8	9.2	-19.3	-261.2	-105.7	-71.2
300-200	1.4	21.1	-20.1	-284.4	13.6	-59.0
400-300	0.4	4.5	-12.6	-192.9	-18.3	-54.4
500-400	-7.9	0.7	-7.0	-125.4	6.5	-32.4
600-500	-11.3	13.5	-4.0	-118.7	-24.4	-43.3
700-600	-21.7	8.1	-2.2	-352.0	224.4	-38.9
800-700	-27.8	6.5	-1.4	-237.2	269.0	20.1
900-800	-29.4	21.1	-1.4	372.3	-135.9	96.7
Sfc-900	-35.2	19.9	-2.5	378.1	-80.0	121.3
Vertical Total	-135.4	104.7	-70.5	-821.4	149.1	-61.0

4.4.3 Time series profiles

Time series of terms in the kinetic, internal, and potential energy equations show the variability in energy processes that occurs as the upper-level trough moves slowly eastward through the area.

4.4.3.1 Kinetic energy

Kinetic energy increases steadily through the middle of the AVE III experiment when the wave is nearly centered over the observation network at 500 mb (Fig. 4.1). As this trough and its associated wind speed maximum continue eastward out of the area, kinetic energy decreases. Since the wave tilts with height, maximum kinetic energy in the surface- to 700-mb layer occurs 3-h earlier than in the 700- to 400-mb layer.

Generation of kinetic energy due to cross-contour flow increases through the middle of the experiment (Fig. 4.2). Values increase by a factor of five in the 700- to 400-mb layer between 0000 GMT to 1800 GMT 6 February, and increase by a factor of two in the 400- to 100-mb layer. Horizontal flux divergence of kinetic energy shows similar increases during the first part of the experiment (Fig. 4.3). Flux divergence decreases greatly during the latter portion of the experiment as the trough moves out of the center of the experiment area.

Average vertical motion is upward through 0000 GMT 7 February but reverses sign when the trough moves east of the center of the area. Kinetic energy in the lower atmosphere is transported aloft during the first seven times while downward transport of kinetic energy occurs during the last two times (Fig. 4.4).

Transfer of kinetic energy from grid to subgrid scales of motion increases greatly above 700 mb during the last two times (Fig. 4.5). Positive dissipation, meaning a transfer of kinetic energy from subgrid to grid scales of motion, occurs at three times in the middle troposphere. Motions that are unresolvable in time and/or space and computational error can contribute to positive values of dissipation. During the AVE III experiment, turbulence associated with extreme horizontal and vertical wind shear may produce positive values.

As described earlier, generation of kinetic energy due to cross-contour flow is very large during the experiment. But, what happens to this generated energy? Horizontal transport out of the area is the primary energy sink during the first seven times when this process removes between 33% and 99% of the generated energy in the surface- to 100-mb layer (Fig. 4.6).

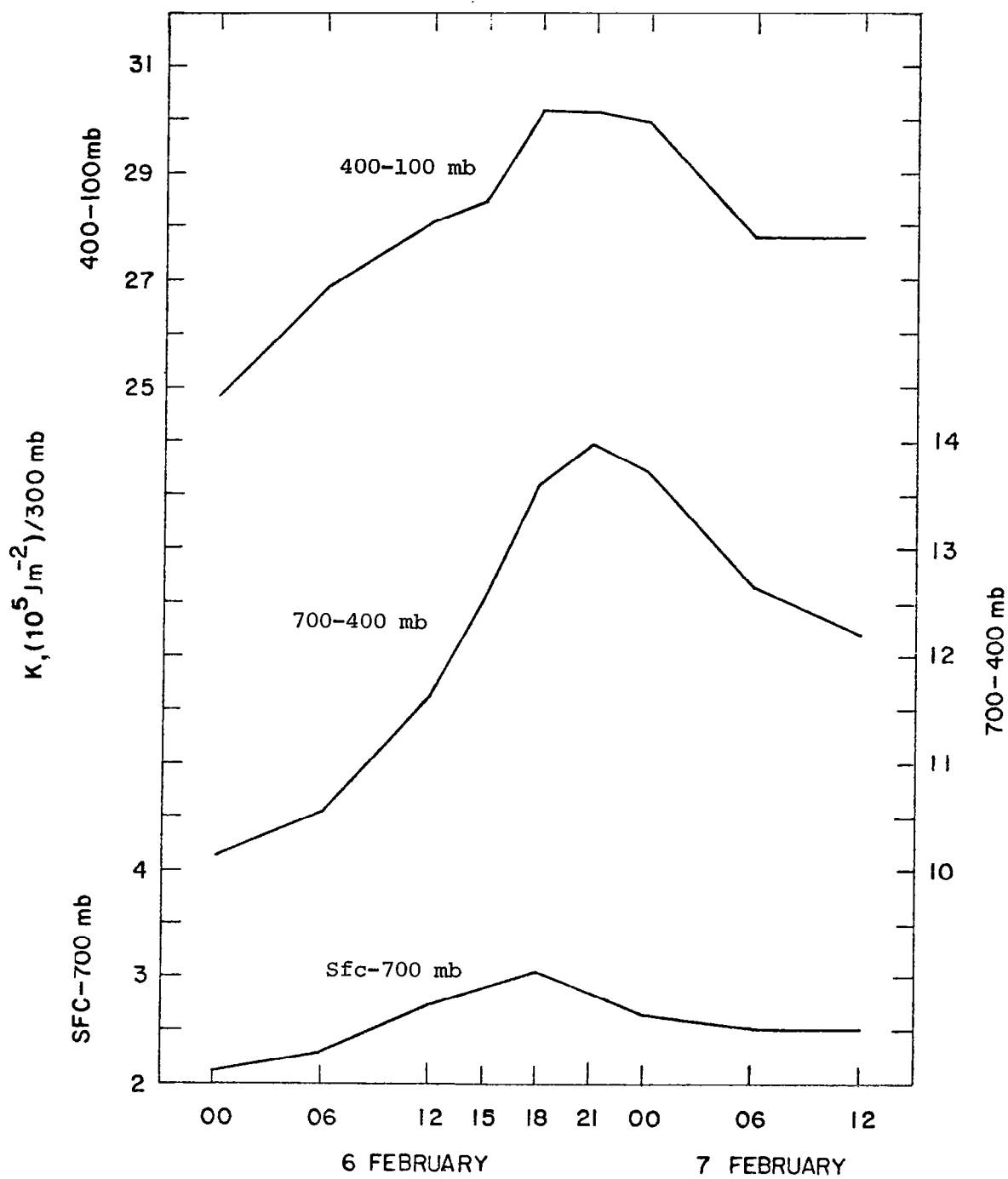


Fig. 4-1. Time series of kinetic energy in AVE III.

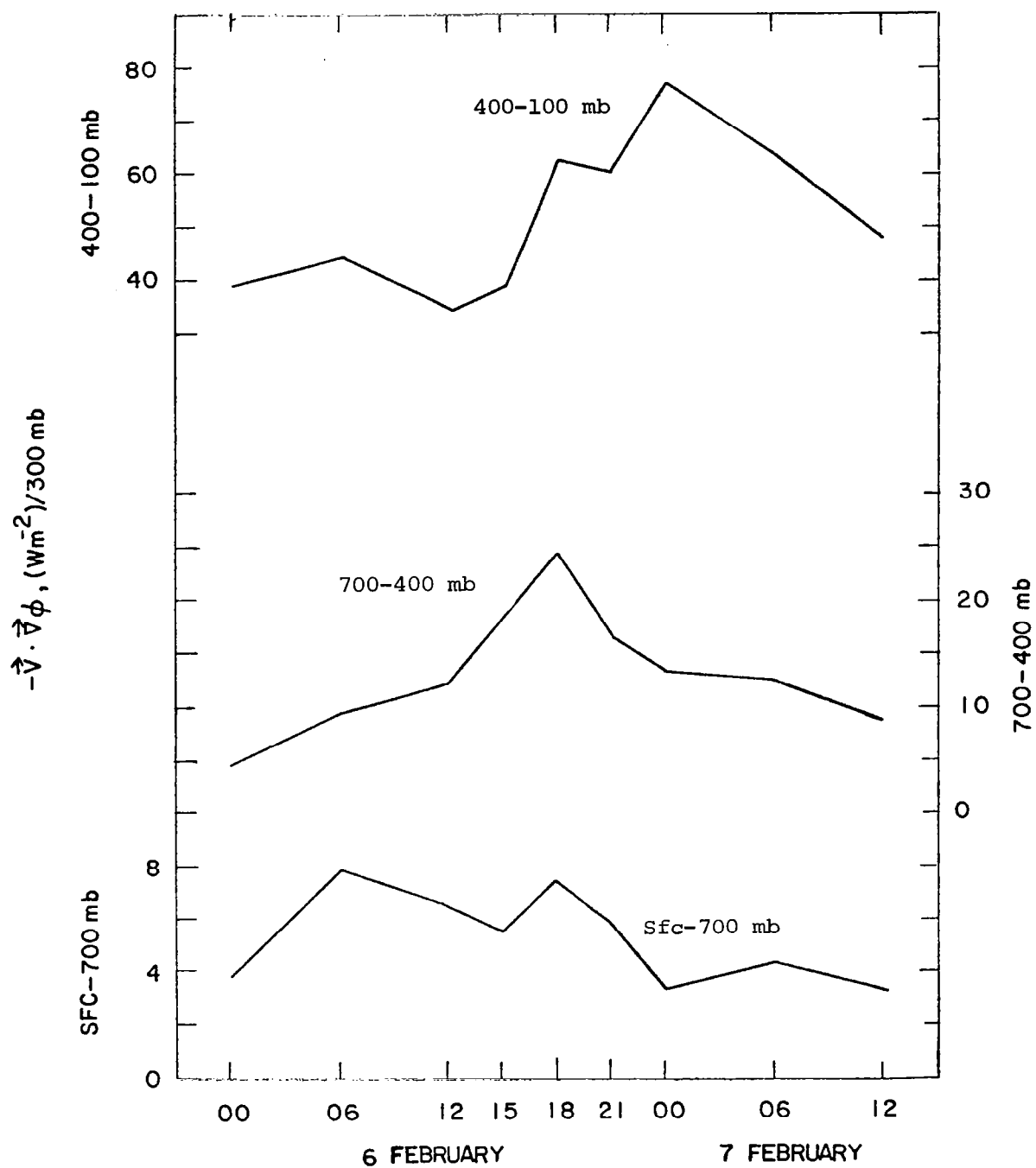


Fig. 4-2. Time series of generation of kinetic energy in AVE III.

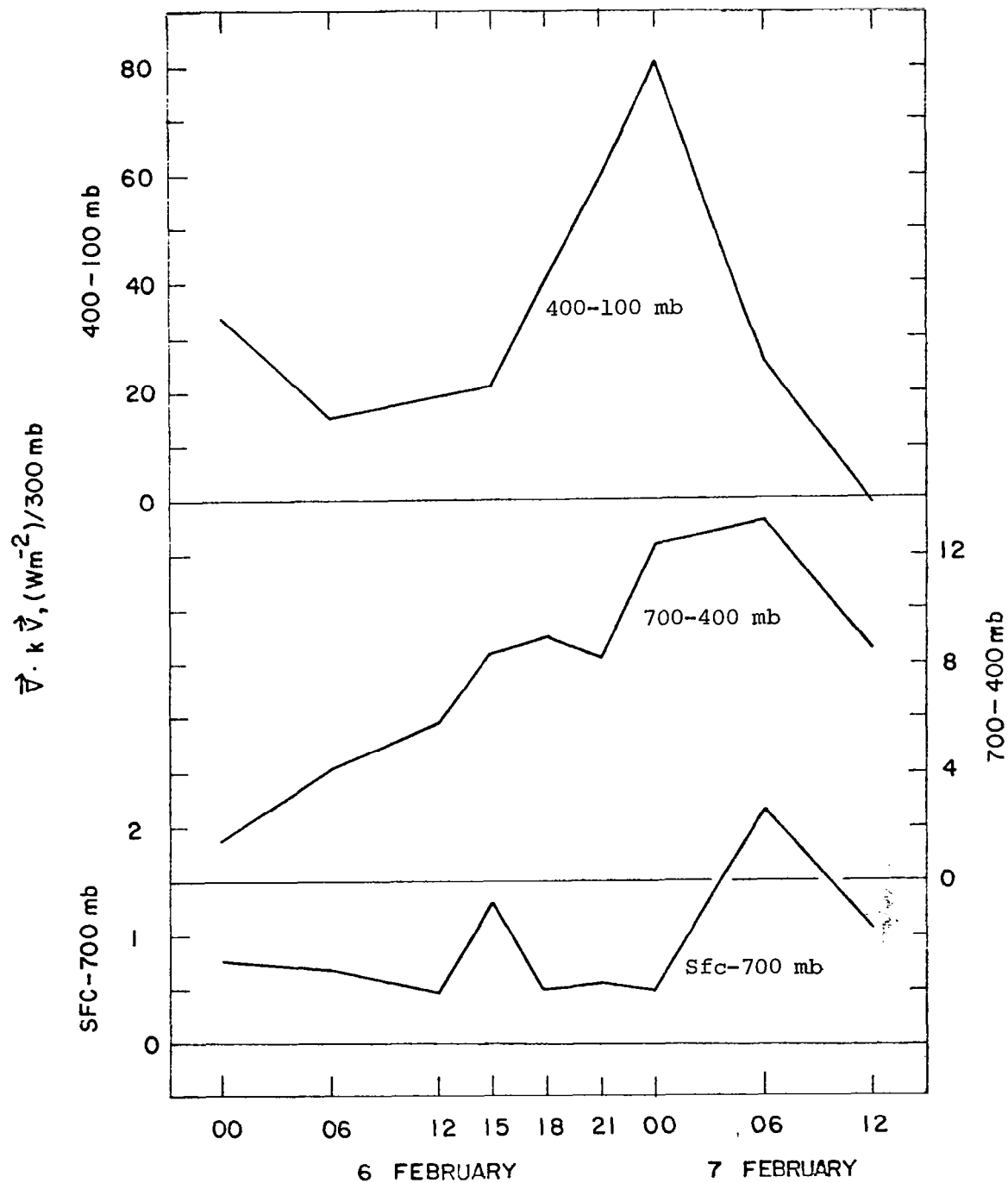


Fig. 4-3. Time series of horizontal flux divergence of kinetic energy in AVE III.

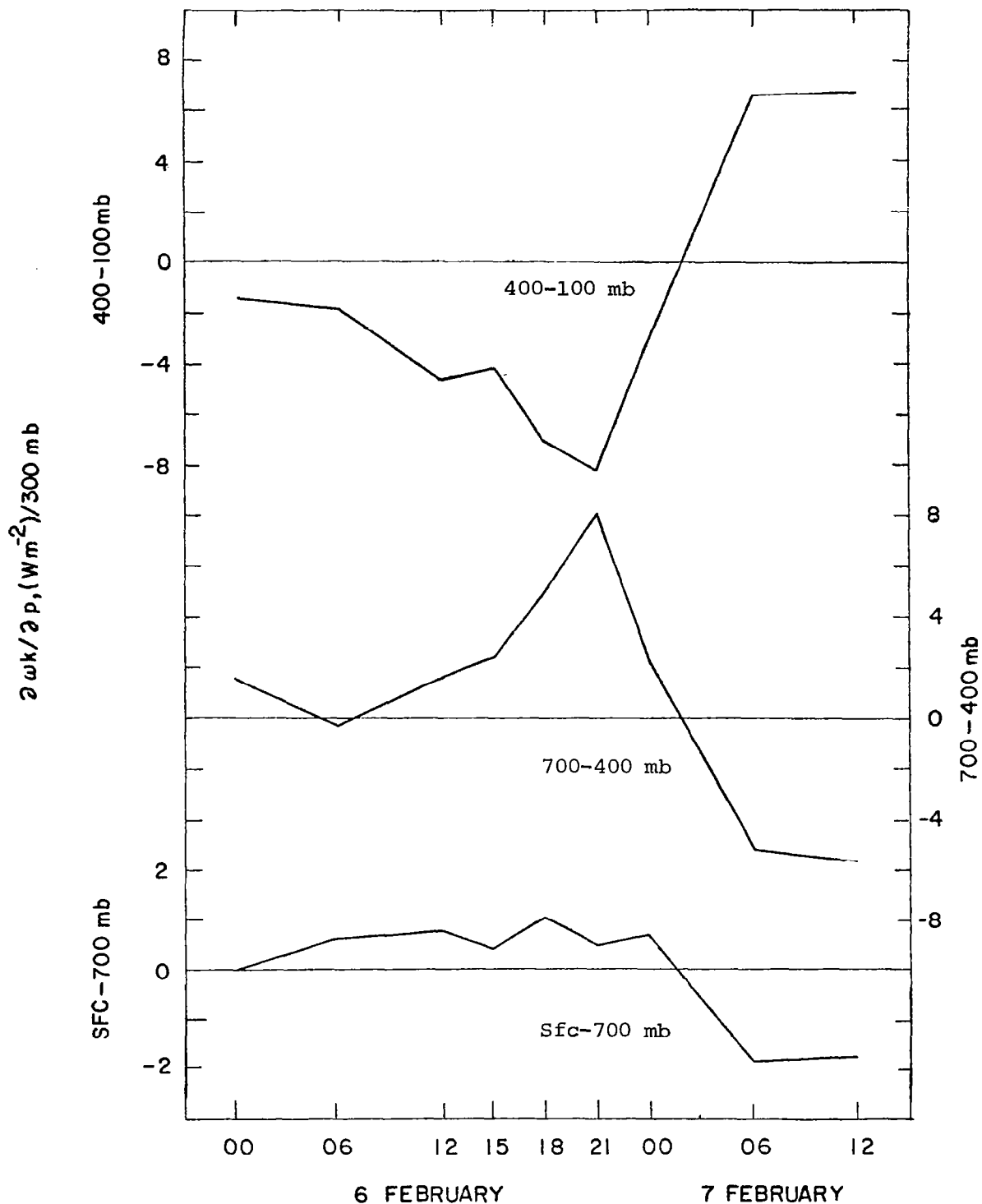


Fig. 4-4. Time series of vertical flux divergence of kinetic energy in AVE III.

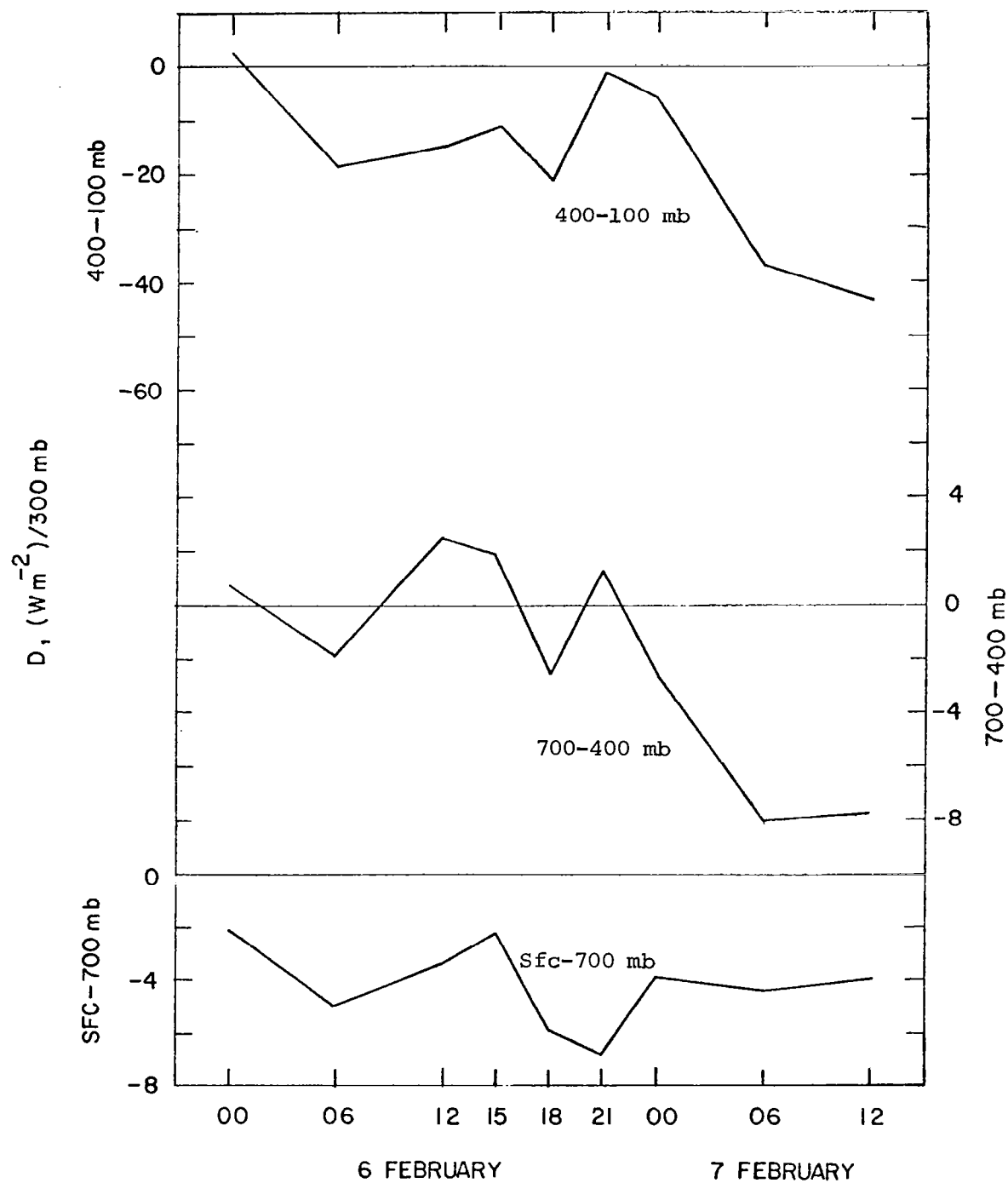


Fig. 4-5. Time series of dissipation of kinetic energy in AVE III.

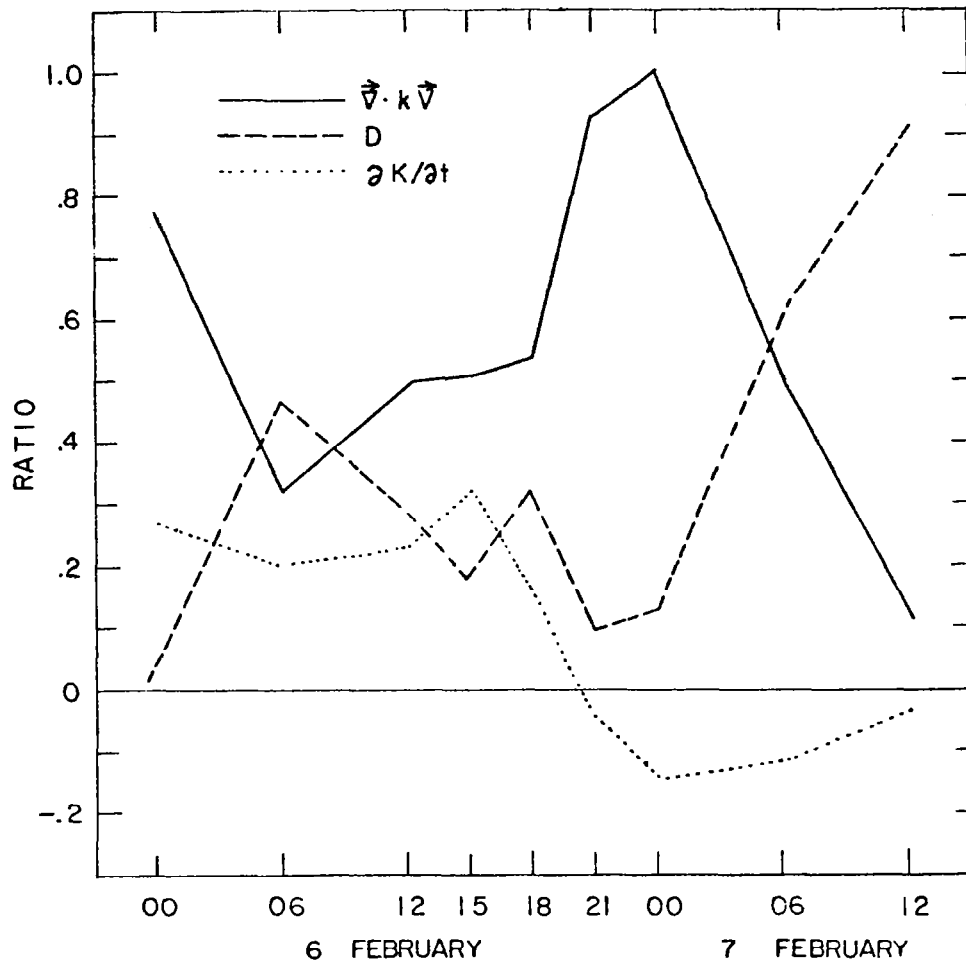


Fig. 4-6. Time series of the ratio between horizontal flux divergence of kinetic energy, dissipation of kinetic energy, and the local change of kinetic energy to the cross-contour generation of kinetic energy in the surface- to 100-mb layer.

Dissipation is a much smaller sink during these times; only about 25% of the generated kinetic energy is transferred to subgrid scales of motion. About 25% of the generated energy is used to increase kinetic energy content.

Conditions change dramatically after 0000 GMT 7 February when the trough moves east of the center of the area. Dissipation becomes the primary energy sink of generated energy with horizontal flux divergence assuming a minor role. Term $\frac{\partial K}{\partial t}$ is negative after 2100 GMT 6 February since more energy is dissipated and transported out of the area than is generated.

4.4.3.2 Internal and potential energy

The time series of generation of internal energy by diabatic effects, computed using the thermodynamic equation, is given in Fig. 4.7. Radiative effects dominate the generation process; production of internal energy occurs during the day and destruction occurs at night. Generation due to latent heat release associated with light precipitation that occurred over much of the AVE area during the first half of the experiment is not noticeable in the profiles. The heavier precipitation observed during AVE III was confined to a relatively small area and contributed little to the average over the network. Although latent heat release associated with precipitation certainly creates energy, the effects are masked by radiative processes.

Horizontal flux convergence of internal and potential energy occurs in the lower atmosphere during the first three times when the low-level trough dominates the circulation (Fig. 4.8). Flux divergence is evident in the lower atmosphere during the later times in association with the surface anticyclone and eastward movement of the upper-level trough. The 400- to 100-mb layer is generally characterized by horizontal flux divergence through 0000 GMT 7 February, although several times with relatively weak flux convergence also are indicated. The layer is characterized by strong horizontal flux convergence during the last two times. Profiles of vertical flux divergence (Fig. 4.9) together with a knowledge of vertical motion fields indicate that internal and potential energy are transported aloft through 0000 GMT 7 February. Downward transport occurs afterward.

Profiles of cross-contour conversion of energy have been described in Fig. 4.2. Although very important to the kinetic energy budget, cross-contour conversion is quite small in the internal and potential energy budget when compared to the boundary transport processes. The boundary work term indicates significant interaction between the limited volume under consideration with the surrounding atmosphere (Fig. 4.10).

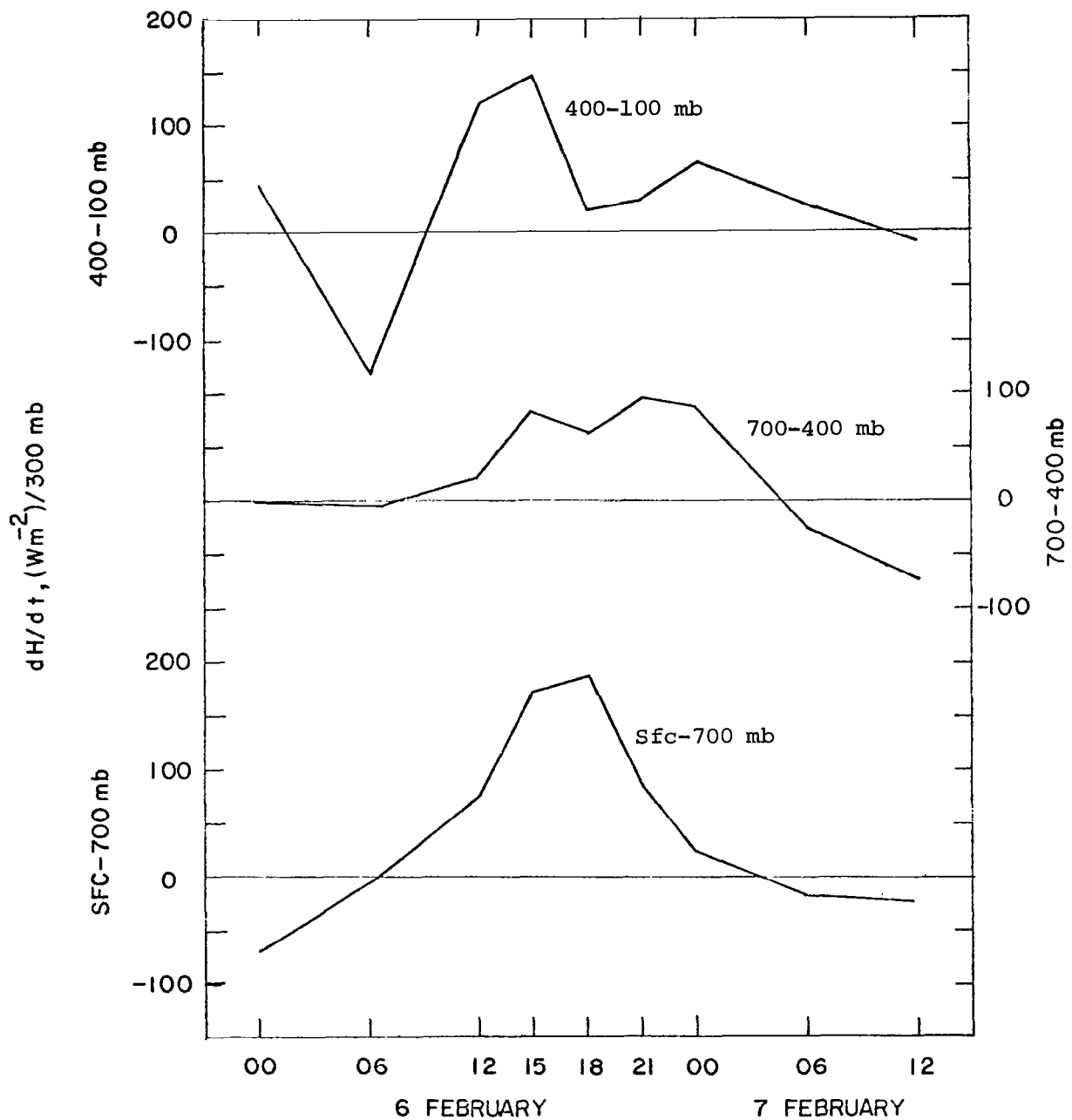


Fig. 4-7. Time series of production of internal energy by diabatic effects in AVE III.

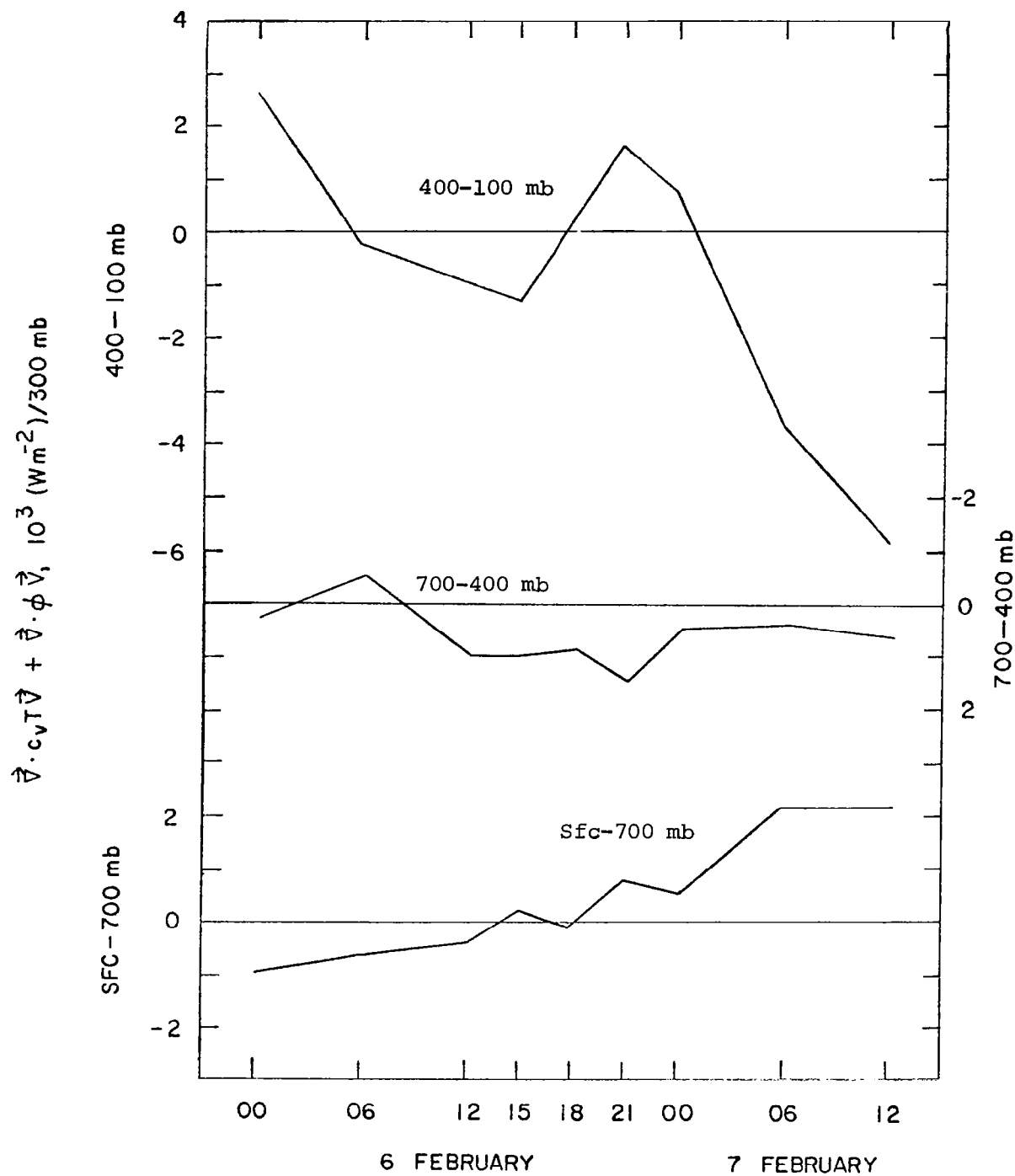


Fig. 4-8. Time series of the sum of horizontal flux divergence of internal energy and potential energy in AVE III.

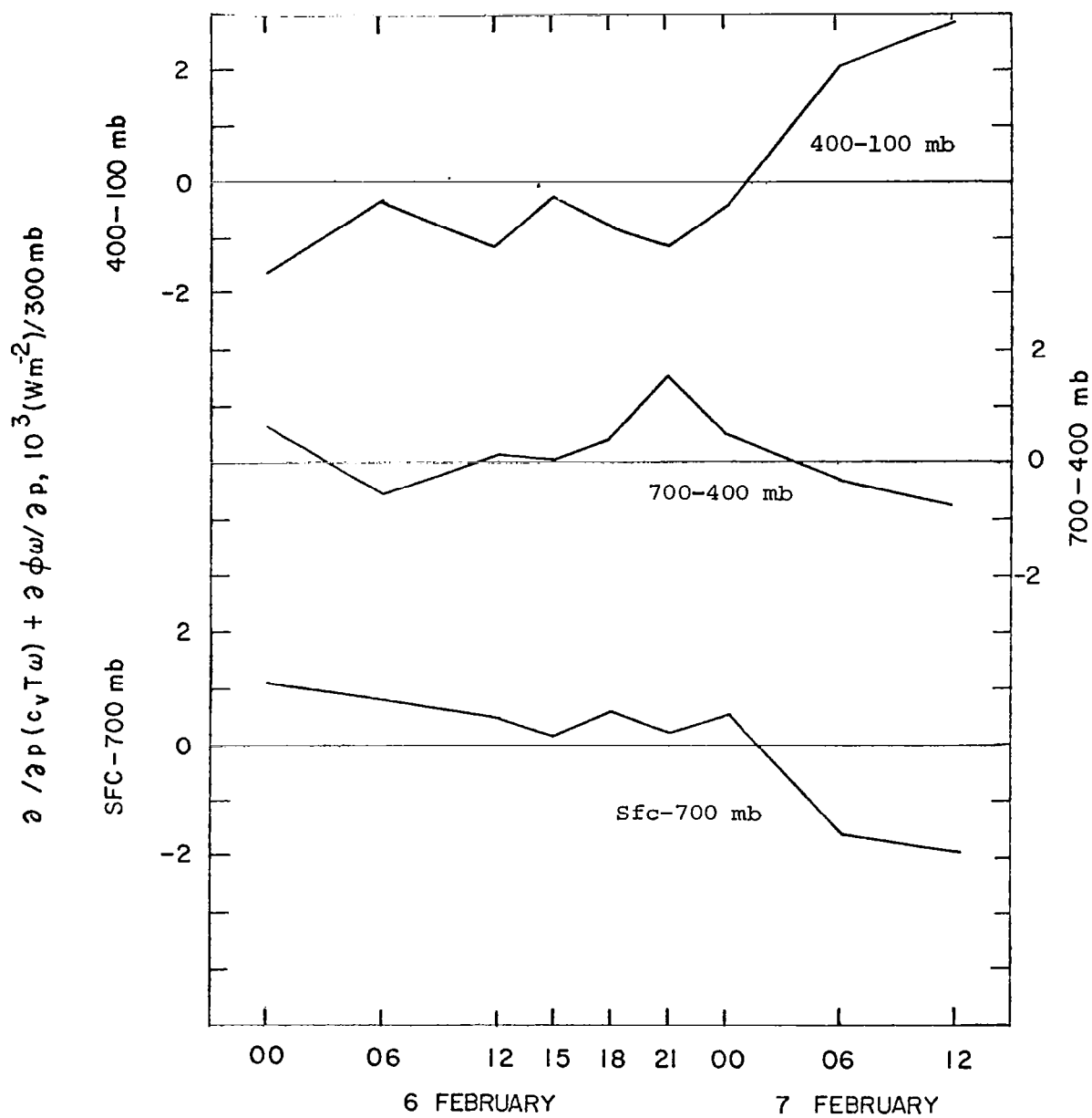


Fig. 4-9. Time series of the sum of vertical flux divergence of internal energy and potential energy in AVE III.

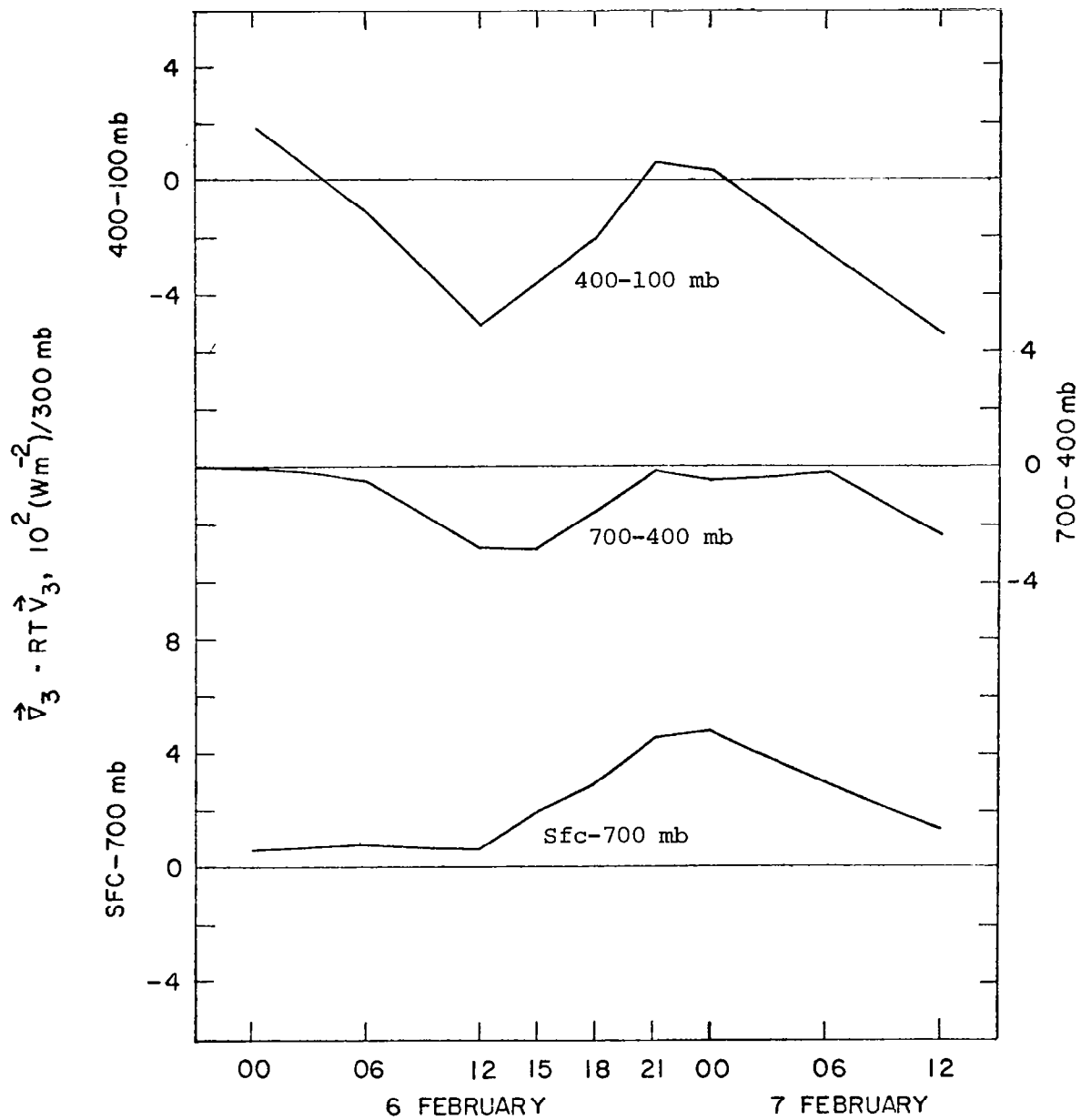


Fig. 4-10. Time series of the pressure work term in AVE III.

The net effect of generation and transport of internal and potential energy can be seen in the local change term (Fig. 4.11). Since horizontal and vertical flux divergence and boundary work tend to cancel each other, changes in energy are closely related to generation by diabatic effects (Fig. 4.7). The variation in cross-contour destruction of available potential energy (Fig. 4.2) is relatively small when compared to the diabatic term.

4.4.4 Energy budgets versus precipitation intensity

Energy conversion and transport processes have been related to the presence and intensity of precipitation by Fuelberg (1977). The procedure was to average grid point values of energy budget terms over ranges of Manually Digitized Radar (MDR) values for all nine observation times. Results of a similar study are described here using the AVE III data. The five categories include all 1512 grid points (MDR 0-9), 1414 grid points with no precipitation or very light precipitation (MDR 0-1), 98 points with moderate to intense precipitation (MDR 2-9), 48 points with strong to intense precipitation (MDR 4-9), and 16 grid points with intense precipitation (MDR 8-9). The AVE III data are not as suitable for this type of study as the AVE IV data used previously because heavy precipitation is not widespread during AVE III and occurs only near the edge of the data area. However, meaningful results are obtained for comparison purposes.

Generation of kinetic energy by cross-contour flow is much greater in areas of moderate precipitation than in areas of no precipitation and light precipitation (Fig. 4.12). This difference occurs because of the different synoptic conditions in which precipitation forms and due to the effect of precipitation on the surrounding atmosphere (Danard, 1964; Ninomiya, 1971a and b; Auburt, 1957). The integrated value in the surface- to 100-mb layer is 62.8 W m^{-2} for the MDR 0-1 category, and 193.5 W m^{-2} for the MDR 8-9 category. Similar differences in profiles were obtained using AVE IV data (Fuelberg, 1977).

Horizontal flux divergence of kinetic energy in the upper atmosphere is greater for the three precipitation categories than for the remaining two categories (Fig. 4.13). Low-level flux convergence occurs in areas of moderate to intense precipitation, but this feature is absent in the other profiles. Weak vertical flux divergence is associated with the MDR 0-9 and MDR 0-1 categories (Fig. 4.14). Upward vertical motion transports energy aloft in areas of precipitation. Similar profiles were observed during the AVE IV experiment.

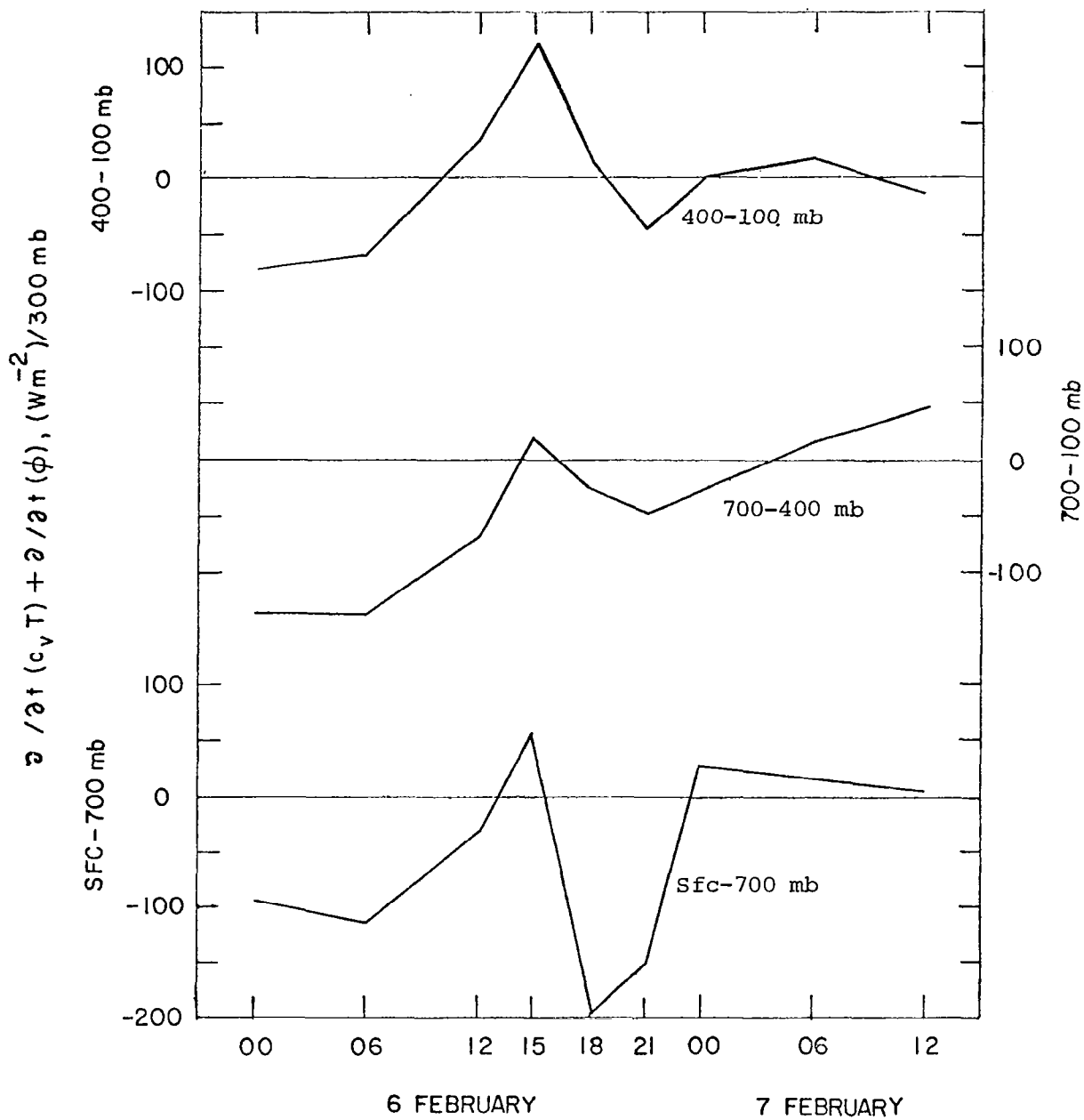


Fig. 4-11. Time series of the sum of the local change of internal and potential energy in AVE III.

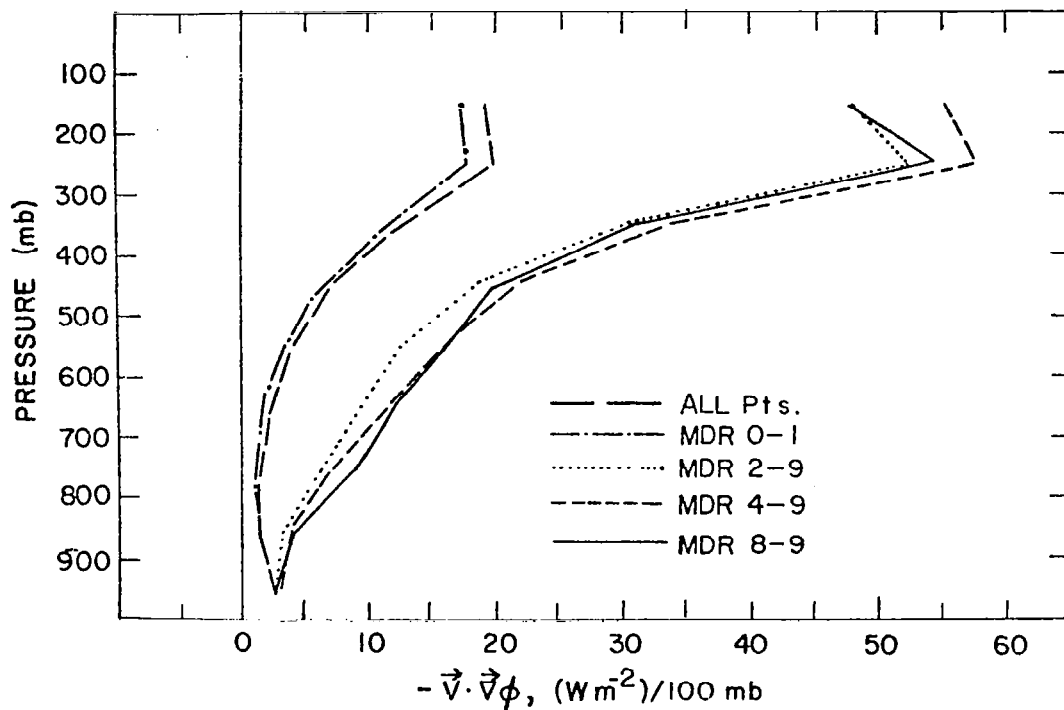


Fig. 4-12. Vertical profiles of generation of kinetic energy for various ranges of MDR values in AVE III.

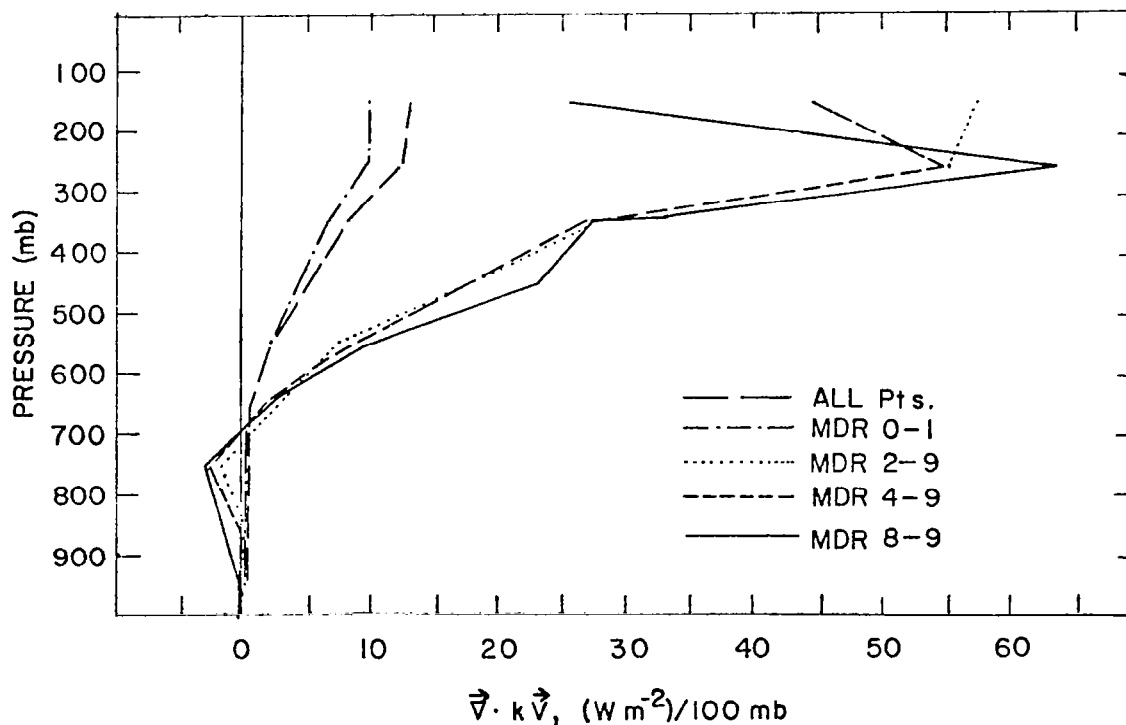


Fig. 4-13. Vertical profiles of horizontal flux divergence of kinetic energy for various ranges of MDR values in AVE III.

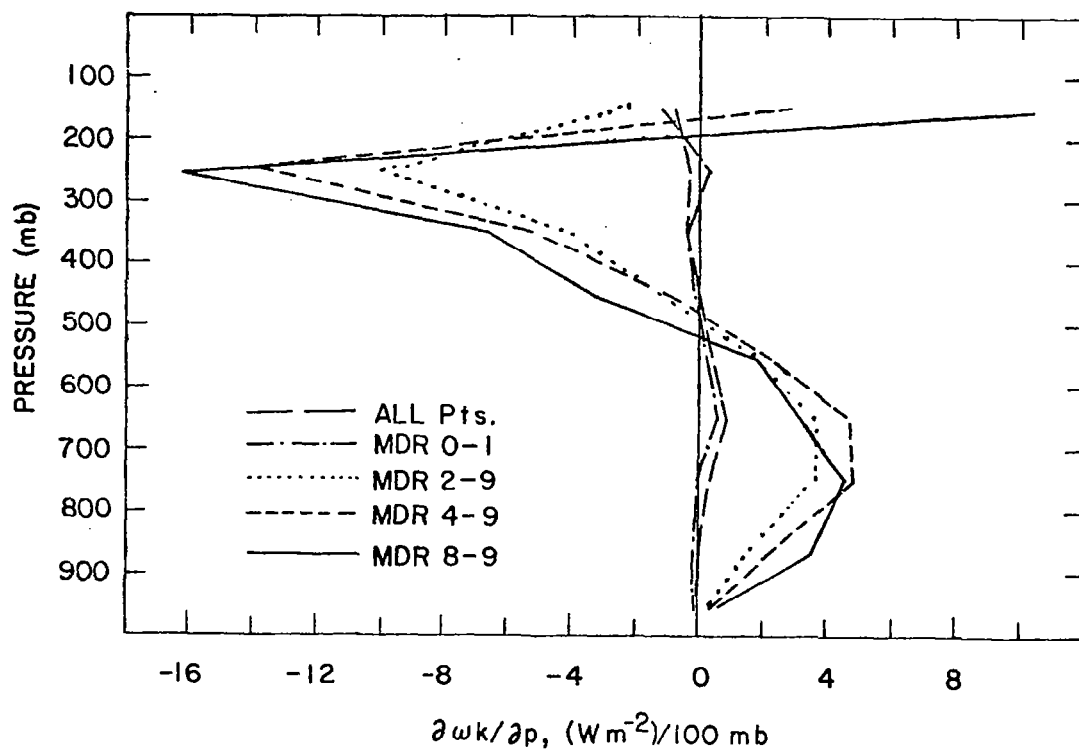


Fig. 4-14. Vertical profiles of vertical flux divergence of kinetic energy for various ranges of MDR values in AVE III.

Profiles of the dissipation term indicate enhanced transfer of kinetic energy from grid to subgrid scales of motion in areas of precipitation (Fig. 4.15). Positive dissipation in the middle troposphere is associated with the three categories of precipitation, but this feature is not evident in the MDR 0-9 and MDR 0-1 categories (Fig. 4.14). Upward vertical motion transports energy aloft in areas of precipitation. Similar profiles were observed during the AVE IV experiment.

Profiles of the dissipation term indicate enhanced transfer of kinetic energy from grid to subgrid scales of motion in areas of precipitation (Fig. 4.15). Positive dissipation in the middle troposphere is associated with the three categories of precipitation, but this feature is not evident in the MDR 0-9 and MDR 0-1 categories. Again, these features are comparable to those reported by Fuelberg (1977) for AVE IV.

The tabulated kinetic energy budget for the MDR 4-9 category is given in Table 4.4. Generation, dissipation, and transport of kinetic energy are

Table 4.4. Kinetic energy budget for the 48 grid points with MDR values between 4 and 9.

Pressure Layer	K	$\frac{\partial K}{\partial t}$	$\vec{V} \cdot k \vec{V}$	$\frac{\partial \omega k}{\partial p}$	$-\vec{V} \cdot \vec{V} \phi$	D
mb	10^5 J m^{-2}	W m^{-2}	W m^{-2}	W m^{-2}	W m^{-2}	W m^{-2}
200-100	14.1	5.2	44.6	2.8	54.9	-2.3
300-200	11.5	-3.1	55.4	-13.8	57.6	-19.1
400-300	8.6	-0.2	26.7	-5.2	32.9	-11.6
500-400	6.0	3.5	17.0	-1.1	21.3	-1.9
600-500	4.6	5.5	8.2	2.2	15.5	0.4
700-600	3.1	4.6	1.2	4.7	11.3	-0.8
800-700	1.9	2.6	-2.5	4.8	7.1	-2.2
900-800	1.0	0.9	-0.3	2.2	3.6	-0.8
sfc-900	0.4	0.3	-0.2	0.5	1.8	-1.2
Vertical Total	51.2	19.3	150.1	-2.9	206.0	-39.5

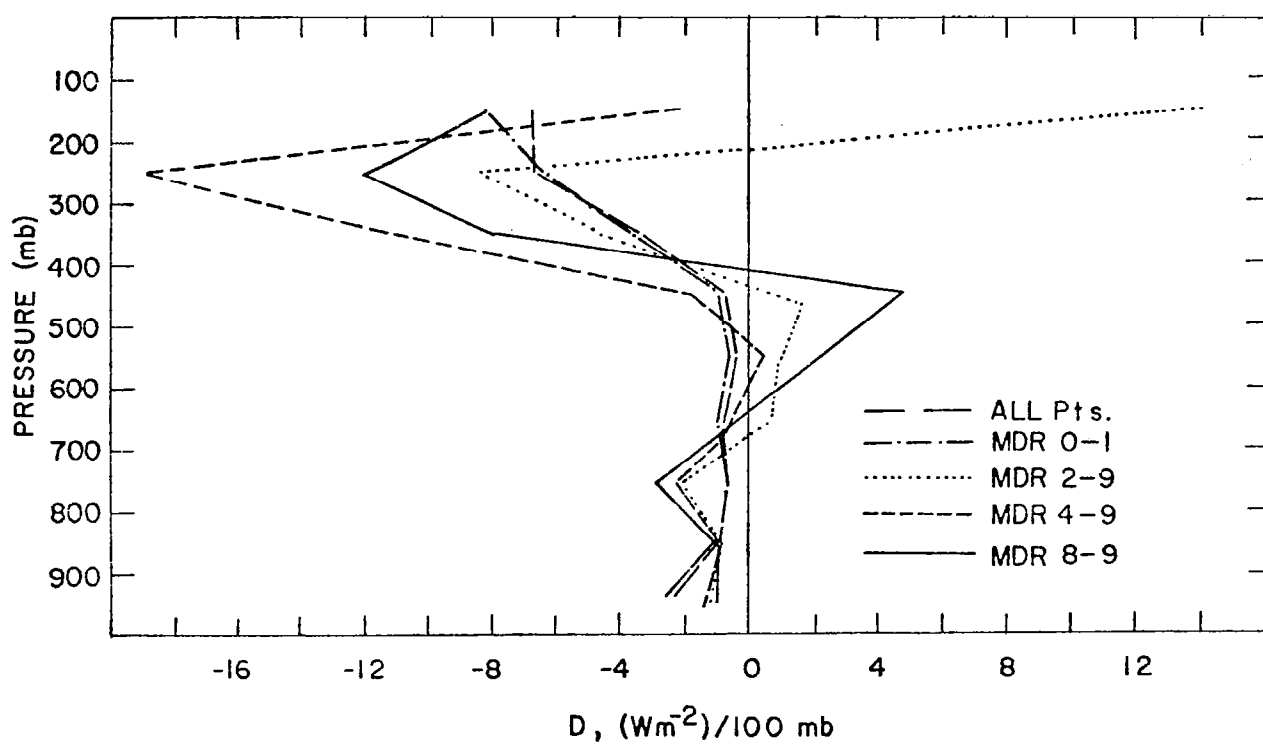


Fig. 4-15. Vertical profiles of dissipation of kinetic energy for various ranges of MDR values in AVE III.

much greater in areas of moderate or intense precipitation than for the AVE III area as a whole (Table 1.1). Generation by cross-contour flow is offset mostly by horizontal flux divergence. Dissipation of energy is far less important.

Generation of internal energy by diabatic heating is greater in areas of precipitation than over the total area (Fig. 4.16). The enhanced generation, which reaches a maximum near 650 mb, is due to latent heat release associated with precipitation. Large negative values near 200 mb may be due to radiative cooling from the tops of clouds.

Low-level horizontal flux convergence of internal and potential energy and vertical flux divergence together with upper-level horizontal flux divergence and vertical flux convergence become stronger for the categories of more intense precipitation (Figs. 4.17 and 4.18). Similar results were obtained during the AVE IV experiment.

The tabulated internal and potential energy budget for grid points with MDR values between 4 and 9 (Table 4.5) indicates that generation and transport of energy in areas of moderate or intense precipitation are much greater than are observed in the AVE III area as a whole (Table 4.3).

4.5 Conclusions

Intense energy conversion and transport processes occur during the AVE III experiment when a broad upper-level trough passes over the eastern United States. An especially interesting feature is strong generation of kinetic energy by cross-contour flow. Much of this generated kinetic energy is transported horizontally out of the area. A smaller amount of energy is transferred to subgrid scales of motion while even less of the generated energy is used to increase the kinetic energy content of the volume. Horizontal and vertical transport processes are the largest components of the combined budget of internal and potential energy. Generation by diabatic heating is small.

Energy processes near the beginning of the experiment when the upper-level trough was approaching the center of the area are considerably different from those at the end of the experiment when the trough was near the eastern edge of the data network. Rawinsonde data at 3- or 6-h intervals permit a detailed temporal description of the energy changes that occur. Cross-contour generation and horizontal flux divergence of kinetic energy are a maximum

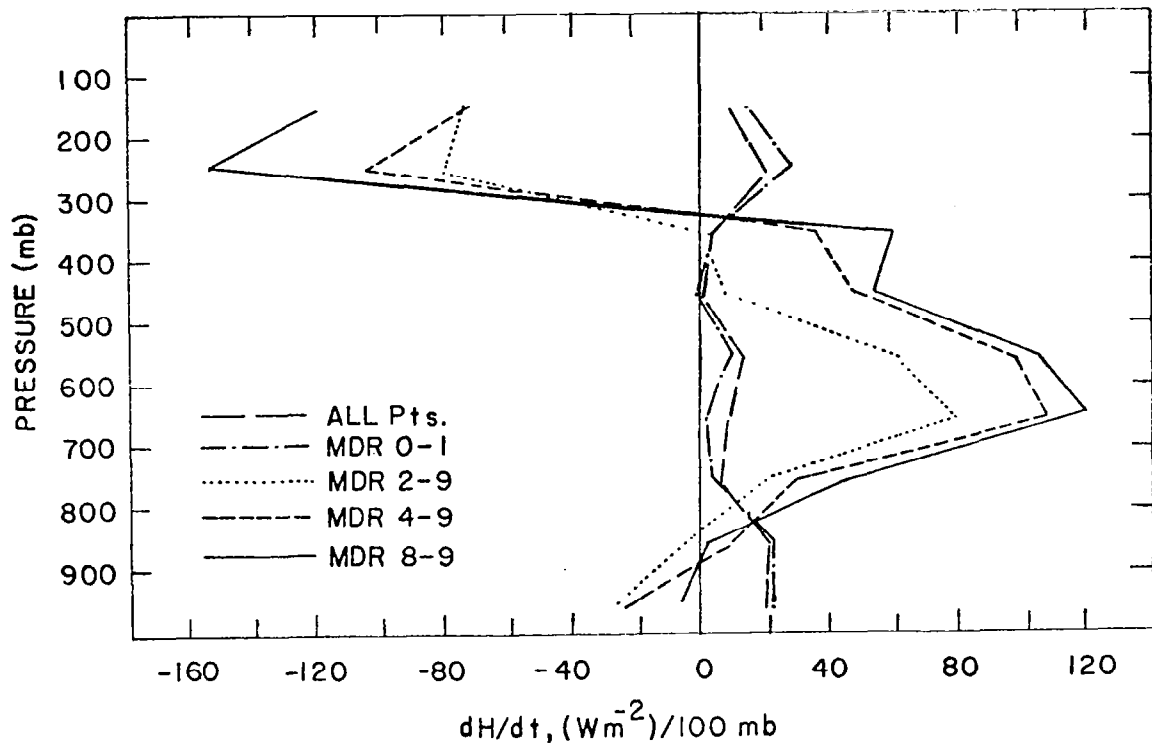


Fig. 4-16. Time series of creation of internal energy by diabatic effects in AVE III.

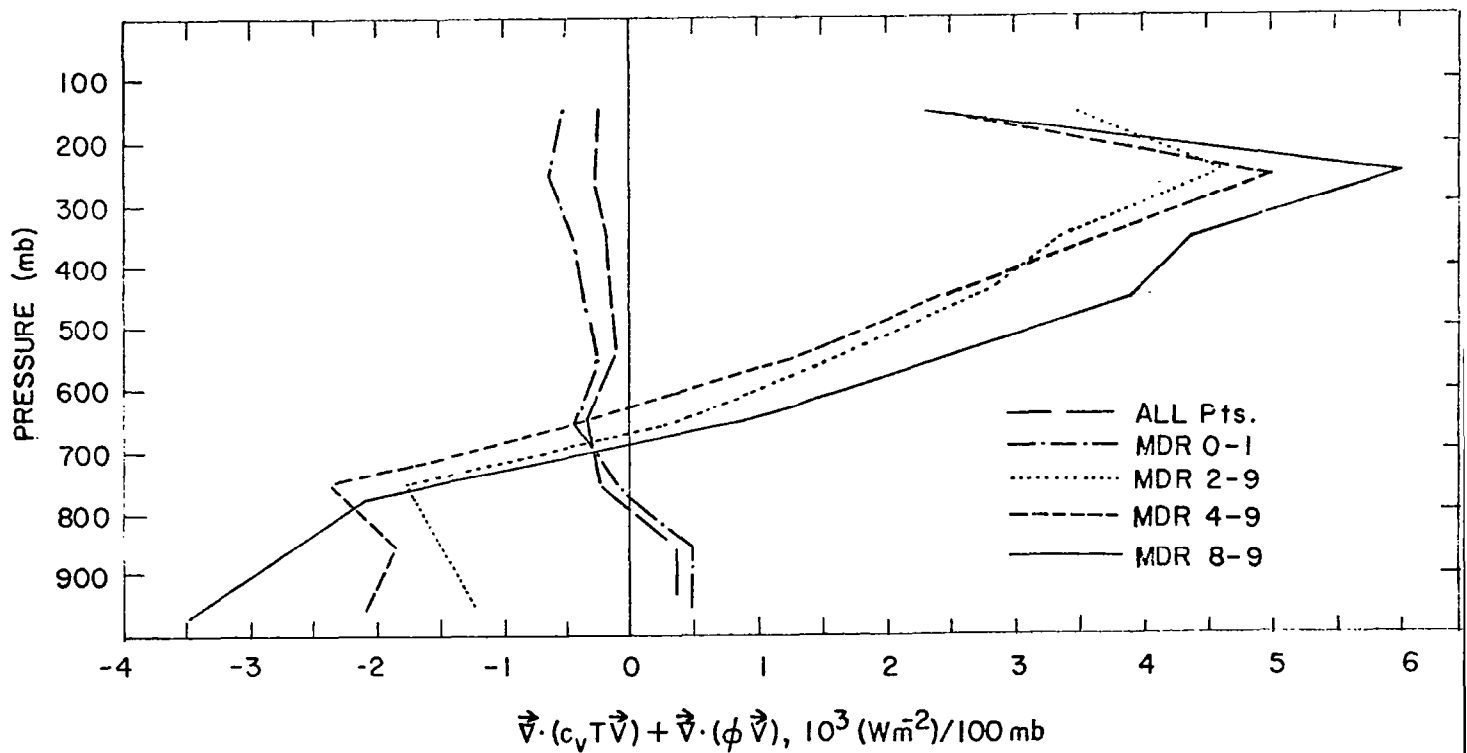


Fig. 4-17. Vertical profiles of the sum of horizontal flux divergence of internal energy and potential energy in AVE III.

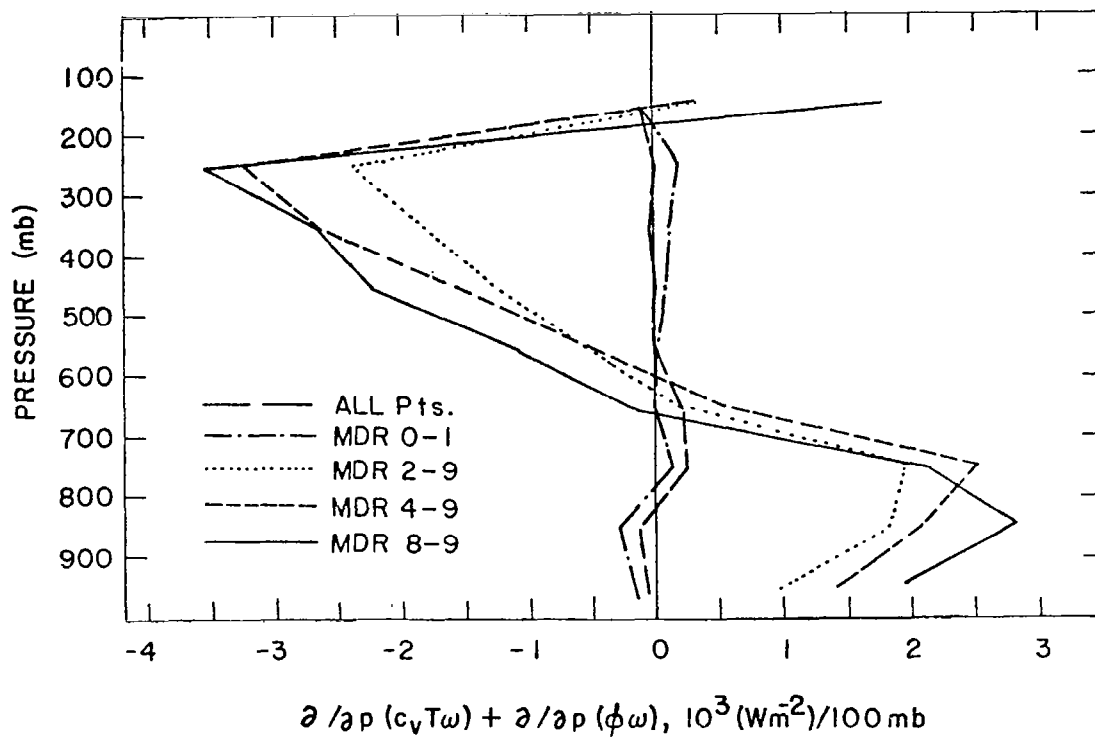


Fig. 4-18. Vertical profiles of the sum of vertical flux divergence of internal energy and potential energy in AVE III.

Table 4.5. Combined internal and potential energy budget for the 48 grid points with MDR values between 4 and 9.

Pressure Layer mb	$\frac{\partial}{\partial t}(c_v T) + \frac{\partial \phi}{\partial t}$ $W m^{-2}$	$\frac{dH}{dt}$ $W m^{-2}$	$\vec{V} \cdot \vec{\nabla} \phi$ $W m^{-2}$	$\vec{V} \cdot (c_v T \vec{V}) + \vec{V} \cdot \phi \vec{V}$ $W m^{-2}$	$\frac{\partial}{\partial p}(c_v T \omega) + \frac{\partial}{\partial p}(\phi \omega)$ $W m^{-2}$	$\vec{V}_3 \cdot (RT \vec{V}_3)$ $W m^{-2}$
200-100	-34.5	-72.3	-54.9	2507.4	341.2	673.6
300-200	-7.1	-105.5	-57.6	5023.6	-3227.2	418.7
400-300	16.7	35.4	-32.9	3687.3	-2657.3	194.4
500-400	-3.5	43.5	-21.3	2452.7	-1518.9	151.4
600-500	-5.1	97.3	-15.5	1346.7	-536.7	126.5
700-600	-12.7	109.4	-11.3	-328.4	585.9	-35.2
800-700	-31.6	29.6	-7.1	-2366.2	2514.2	-32.9
900-800	-32.0	11.7	-3.6	-1821.3	2065.7	49.3
Sfc-900	-39.3	-22.2	-1.8	-2047.7	1384.7	-272.3
Vertical Total	-149.1	126.9	-206.1	8454.1	-1048.3	1273.6

when the trough is centered over the area, but then decrease in magnitude. Upward transport of kinetic energy during the first part of the AVE III experiment changes to downward transport toward the end of the period. Negative dissipation of energy is greatest toward the end of the experiment as the trough exits the area.

Temporal changes in horizontal and vertical flux divergence of internal and potential energy are generally similar to those of kinetic energy.

Energy generation and transport processes associated with precipitation are much larger than those observed for the entire AVE III area. Results are similar to those found during the AVE IV experiment.

4.6 References

- Aubert, E. J., 1957: On the release of latent heat as a factor in large-scale atmospheric motions. J. Meteor., 14, 527-542.
- Barnes, S. L., 1964: A technique for maximizing detail in numerical weather map analysis. J. Appl. Meteor., 3, 396-409.
- Chen, T., and L. F. Bosart, 1977: Quasi-Lagrangian kinetic energy budgets of composite cyclone-anticyclone couplets. J. Atmos. Sci., 34, 452-464.
- Danard, M. B., 1964: On the influence of released latent heat on cyclone development. J. Appl. Meteor., 3, 27-37.
- Fuelberg, H. E., 1974: Reduction and error analysis of the AVE II pilot experiment data. NASA CR-120496, George C. Marshall Space Flight Center, Alabama, 131 pp.
- _____, 1977: Atmospheric energetics in regions of intense convective activity. NASA CR-2826, National Aeronautics and Space Administration, Washington, D. C., 136 pp.
- _____, and J. R. Scoggins, 1978: Kinetic energy budgets during the life cycle of intense convective activity. Mon. Wea. Rev., 106, 637-653.
- _____, and R. E. Turner, 1975: Data for NASA's AVE III experiment: 25-mb sounding data and synoptic charts. NASA TM X-64938, George C. Marshall Space Flight Center, Alabama, 462 pp.
- Kornegay, F. C., and D. G. Vincent, 1976: Kinetic energy budget analysis during interaction of tropical storm Candy (1968) with an extratropical frontal system. Mon. Wea. Rev., 104, 849-859.
- Kung, E. C., 1966: Kinetic energy generation and dissipation in the large-scale atmospheric circulation. Mon. Wea. Rev., 94, 67-82.
- _____, and W. E. Baker, 1975: Energy transformation in middle-latitude disturbances. Quart. J. Roy. Meteor. Soc., 101, 793-815.
- _____, and P. J. Smith, 1974: Problems of large-scale kinetic energy balance--A diagnostic analysis in GARP. Bull. Amer. Meteor. Soc., 55, 768-777.
- Ninomiya, K., 1971a: Dynamical analysis of outflow from tornado-producing thunderstorms as revealed by ATS III pictures. J. Appl. Meteor., 10, 275-294.
- _____, 1971b: Mesoscale modification of synoptic situations from thunderstorm development as revealed by ATS III and aerological data. J. Appl. Meteor., 10, 1103-1121.

- O'Brien, J. J., 1970: Alternate solution to the classical vertical velocity problem. J. Appl. Meteor., 9, 197-203.
- Petterssen, S., and S. J. Smebye, 1971: On the development of extratropical cyclones. Quart. J. Roy. Meteor. Soc., 97, 457-482.
- Shuman, F. G., 1957: Numerical methods in weather prediction: II. Smoothing and filtering. Mon. Wea. Rev., 85, 357-361.
- Smith, P. J., 1970: A note on energy conversions in open atmospheric systems. J. Atmos. Sci., 27, 518-521.
- _____, 1973a: Mid-latitude synoptic scale systems: Their kinetic energy budgets and role in the general circulation. Mon. Wea. Rev., 101, 757-762.
- _____, 1973b: The kinetic energy budget over North America during a period of major cyclone development. Tellus, 25, 411-423.
- _____, and S. P. Adhikary, 1974: The dissipation of kinetic energy in large-scale atmospheric circulations. Rev. Geophys. Space Phys., 12, 281-284.
- Vincent, D. G., and L. N. Chang, 1975: Kinetic energy budgets of moving systems: Case studies for an extratropical cyclone and hurricane Celia, 1970: Tellus, 27, 215-233.
- Ward, J. H., and P. J. Smith, 1976: A kinetic energy budget over North America during a period of short synoptic wave development. Mon. Wea. Rev., 104, 836-848.
- West, P. W., 1973: Atmospheric energetics as related to cyclogenesis over the eastern United States. NASA CR-2189, Marshall Space Flight Center, Alabama, 103 pp.
- Wilson, G. S., 1976: Large-scale vertical motion calculations in the AVE IV experiment. Geophys. Res. Letters, 3, 735-740.

GRADIENTS OF METEOROLOGICAL PARAMETERS DURING AVE III

by

Milton S. McCown*
Department of Meteorology
Texas A&M University
College Station, Texas 77843

ABSTRACT

Horizontal gradients of geopotential height, temperature, wind speed, and mixing ratio were computed at the 850-, 700-, 500-, and 200-mb levels (gradients of mixing ratio not computed at 200 mb) and results presented for AVE III as was done previously for AVE II and AVE IV. AVE III is a wintertime case; AVE II and AVE IV were springtime cases. The results for AVE III are essentially the same as those for the other AVEs.

Mixing ratio gradients are generally largest near convective areas, and wind speed gradients at 850 mb tend to be largest near storms as identified by Manually Digitized Radar (MDR) data. Differences in the gradients of the parameters were observed between convection associated with fronts and that associated with squall lines.

The analysis of HIPLEX data indicated that the magnitude of gradients versus distances over which the gradients were computed continued to increase as the gradient distances decreased down to about 60 km.

*Presently employed by Climatological Consulting Corporation, Asheville, N.C.

CHAPTER 5. GRADIENTS OF METEOROLOGICAL PARAMETERS DURING AVE III

5.1 Introduction

In a previous report, McCown and Scoggins (1977) have shown that different gradient patterns of various meteorological parameters occur in areas where convection is associated with cold fronts and squall lines. These conclusions were based upon gradient analyses of the data presented in the second and fourth Atmospheric Variability Experiments, which are a continuing series of experiments in which data are collected during time periods when rapid changes in weather patterns occur. An analysis of the gradients observed during the third AVE experiment (AVE III) has now been performed and is the primary subject of this report.

5.2 Analytical Procedures

5.2.1 Stratification of Data

Gradients were first considered without regard to convective areas and were calculated for grid points over distances of 315, 630, and 944 km. Cumulative frequency distributions of the computed quantities for each of the three distances were determined.

In an effort to determine differences in gradients observed in convective and nonconvective areas, Manually Digitized Radar (MDR) data were used to define convective areas. Overlays of the composite MDR charts were placed over the computer-generated parameter grid, and any parameter grid point within one-half grid spacing of an MDR block containing a value of 4 or greater was considered as a convective area.

Since distances of 630 km and 944 km were so much larger than the storm areas, no attempt was made to classify the horizontal gradients on scales this large into either convective or nonconvective areas. Even when considering the gradients on a scale as small as 315 km, it should be emphasized that for a particular grid point, some of the gradients had to be calculated using one or more grid points outside of the convective region.

Following the designation of each grid point as being in either a convective or nonconvective area, cumulative frequency distributions and the determination of several statistical parameters were made for the data in convective and nonconvective areas over all nine times of the experiment. The means of the gradients over convective and nonconvective areas were

determined separately for each time, allowing one to see how the mean gradient values changed over these areas. The areas on the grid were also subdivided into four categories according to the strength of the convection as determined from the radar data. These categories and the corresponding MDR values are as follows.

<u>Precipitation category</u>	<u>MDR values</u>
Weak or no precipitation	0, 1
Moderate precipitation or less	0, 1, 2, 3
Strong or intense precipitation	4, 5, 6, 7, 8, 9
Intense precipitation	8, 9

Statistical studies of the gradients of the meteorological parameters were conducted for each of these categories. It should be noted that the category labelled "strong or intense convection" is the same category as that of the "convective" areas defined by McCown and Scoggins (1977).

In an effort to concentrate on how the gradients change as storms move into (or develop in) an area, the horizontal gradients at grid points, which were initially in nonconvective regions but were in convective regions in the succeeding time period, were classified as "prestorm" gradients. Similarly, grid points which had been in convective areas but were in nonconvective areas a time period later, were classified as "poststorm" points. The mean of the horizontal gradients in such prestorm or poststorm areas was then compared with the mean over the same grid points in the corresponding storm areas a time period later, or earlier, than the respective prestorm or poststorm time. An extensive investigation involving the change of intensity of storm areas for all nine time periods and four pressure levels was performed. The changes in intensity of precipitation were subdivided as follows.

<u>Development</u>		<u>Dissipation</u>	
Prestorm	Storm	Storm	Poststorm
MDR = 0, 1 to MDR \geq 2		MDR \geq 2 to MDR = 0, 1	
MDR = 0, 1 to MDR \geq 4		MDR \geq 4 to MDR = 0, 1	
MDR \leq 3 to MDR \geq 4		MDR \geq 4 to MDR \leq 3	
4 \leq MDR \leq 7 to MDR = 8, 9		MDR = 8, 9 to 4 \leq MDR \leq 7	

5.2.2 Gradients

The field of any scalar $Q(x,y)$ can be represented by a set of lines along which Q is constant. The horizontal ascendant vector, $\vec{\nabla}_n Q$, may be written as

$$\vec{\nabla}_n Q = \vec{n} \left(\frac{dQ}{dn} \right) = \hat{i} \left(\frac{\partial Q}{\partial x} \right) + \hat{j} \left(\frac{\partial Q}{\partial y} \right), \quad (5-1)$$

where \vec{n} is normal to the isolines of Q and in the direction of increasing Q . The magnitude of this vector is given by

$$|\vec{\nabla}_n Q| = \left[\left(\frac{\partial Q}{\partial x} \right)^2 + \left(\frac{\partial Q}{\partial y} \right)^2 \right]^{1/2}. \quad (5-2)$$

Following the convention of Saucier (1955), the word "gradient" will refer hereafter only to the magnitude of the ascendant vector.

The centered finite difference approximation for the gradient at any grid point (i, j) can be calculated by the formula:

$$|\vec{\nabla}_n Q|_{ij} = \frac{[(q_{i+1} - q_{i-1})^2 + (q_{j+1} - q_{j-1})^2]^{1/2}}{\Delta s} \quad (5-3)$$

where Δs is the spacing between grid points used in the computation. In this case, Δs represents 315 km since the spacing between adjacent grid points is approximately 157.5 km. Gradients over the distances of 630 km and 944 km also were calculated by considering the values of the parameters at grid points of $i+2, i-2, j+2, j-2$, and $i+3, i-3, j+3, j-3$, respectively. Gradients hereafter will be expressed as differentials (not divided by Δs), or as changes per unit distance (divided by Δs).

Geopotential height, temperature, and wind speed gradients were calculated at 850, 700, 500, and 200 mb for each of the three different distances, and for all times. Mixing ratio gradients were similarly computed, but only for the 850-, 700-, and 500-mb levels. The solid line in Fig. 5.1 represents the outer boundary of grid points used in computing the gradients observed for each of the three distances. For each time, there were 99 grid points for the 315-km distance, 63 for the 630-km distance, and 35 for the 944-km distance.

5.2.3 Statistical parameters

Several statistical techniques were employed in evaluating the data. These included the use of cumulative frequency distributions, sample mean and median as measures of central tendency, and the standard deviation, coefficient

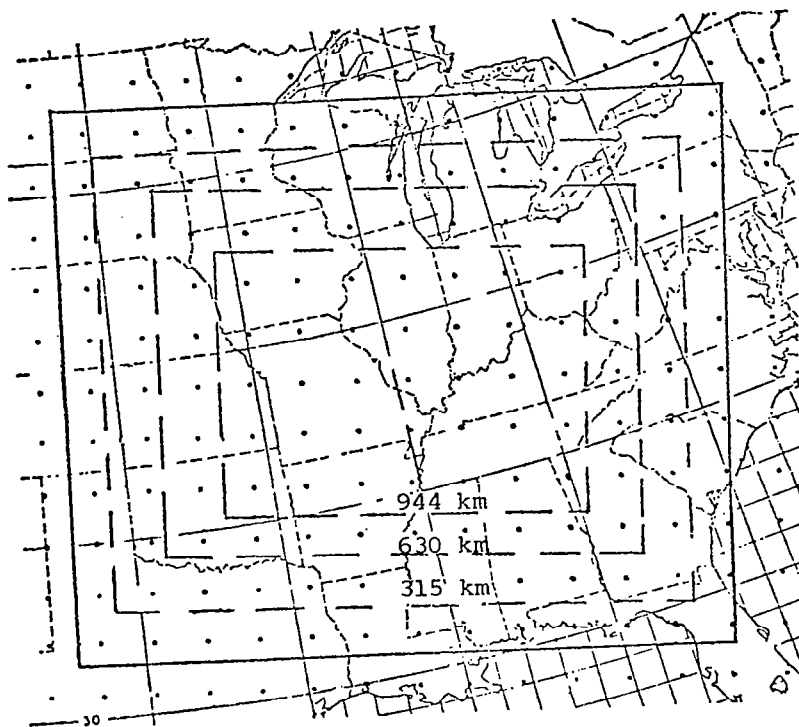


Fig. 5.1. Boundaries encompassing grid points at which gradients over 315, 630, and 944 km were computed.

of variation, and skewness as indicators of the dispersion and variability of the data. In preparing cumulative frequency distributions, the data were first grouped into 20 consecutive, equally-divided class intervals, and the cumulative percent up to the upper limit of each interval determined. Such distributions can be plotted on probability graph paper which can be used to determine how well a given distribution can be fit to a normal distribution.

Used as a measure of central tendency of the data, the mean is the arithmetic average of all the values. The median is the $[(n + 1)/2]$ th observation when the values are arranged in order of magnitude. Since the 50th percentile on a cumulative frequency distribution represents the median, median values in this study were approximated by using an interpolative method as described by Ostle and Mensing (1975).

The most familiar measure of the variability of data is the standard deviation, and is defined by

$$s = \left[\sum_{i=1}^N (x_i - \bar{x})^2 / N \right]^{1/2}, \quad (5-4)$$

where x_i represents the i th observation of a set of numbers, \bar{x} represents the mean, and N is the total number of observations. The coefficient of variation, CV , is a measure of the dispersion of the data, and is useful in comparing series of data that are measured in different units. The variation is expressed as a fraction of the mean and is defined as $CV = s/\bar{x}$. Skewness, a measure of the asymmetry of a distribution, was not calculated directly, but the sign of the skewness was indicated by the relative magnitude of the mean and median values. In symmetric distributions, the median and mean coincide. In cases where the median is less than the mean, positive skewness is indicated, and in cases where the reverse is true, there is negative skewness.

5.3 Results for AVE III

5.3.1 Convective versus nonconvective areas

Table 5.1 contains values of statistical parameters computed for the gradients in both convective areas and nonconvective areas of AVE III. The gradients were computed over 315 km distances.

Geopotential height gradients increased with height in both convective and nonconvective areas, and standard deviations were approximately 10-40% as large as the mean. At all levels the mean (average) height gradients were larger in the nonconvective areas than in the convective areas.

Mean temperature gradients at all levels below 200 mb were larger in the nonconvective areas than in convective regions, while at 200 mb the reverse was true. In both convective and nonconvective areas the largest mean gradients occurred at 850 mb. In the nonconvective areas the temperature gradients tended to decrease with height while the variability (as expressed by the coefficient of variation) generally increased. The mean temperature gradients in the convective areas also tended to decrease with height to 500 mb, and then increased between 500 and 200 mb. The variability did not appear to be a function of height in the convective areas.

Mean wind speed gradients in both convective and nonconvective areas increased with height. At all levels the mean gradients were larger in the convective than in nonconvective areas; however, the variability, as expressed by the coefficient of variation, was larger at all levels in the nonconvective areas than in convective areas.

Mean mixing ratio gradients were larger in the convective areas than elsewhere. As expected, the mean gradients generally decreased with height. The coefficient of variation was large at all levels in both areas indicating

Table 5.1. Selected statistical parameters of gradients in convective and nonconvective areas of AVE III.

Parameter	Convective Areas			Nonconvective Areas		
	Mean	Standard Deviation	Coefficient of Variation	Mean	Standard of Deviation	Coefficient of Variation
Geopotential Height	[m(315 km) ⁻¹]			[m(315 km) ⁻¹]		
850 mb	28.8	6.7	.23	33.6	10.9	.32
700 mb	49.4	11.0	.22	52.2	16.8	.32
500 mb	69.5	19.0	.27	85.8	34.5	.40
200 mb	140.7	36.3	.26	143.9	42.7	.30
Temperature	[°C(315 km) ⁻¹]			[°C(315 km) ⁻¹]		
850 mb	3.8	1.7	.45	5.2	2.6	.50
700 mb	2.6	1.7	.65	4.0	1.9	.48
500 mb	2.1	0.7	.33	4.0	2.9	.73
200 mb	3.6	2.1	.58	2.4	1.7	.71
Wind Speed	[m s ⁻¹ (315 km) ⁻¹]			[m s ⁻¹ (315 km) ⁻¹]		
850 mb	4.4	2.2	.50	3.6	2.2	.61
700 mb	7.2	2.6	.36	5.9	3.7	.63
500 mb	11.2	2.6	.23	9.9	7.6	.77
200 mb	12.2	4.4	.36	10.8	5.9	.55
Mixing Ratio	[g kg ⁻¹ (315 km) ⁻¹]			[g kg ⁻¹ (315 km) ⁻¹]		
850 mb	2.8	1.4	.50	1.1	0.9	.82
700 mb	2.0	1.2	.60	0.9	0.8	.89
500 mb	0.8	0.5	.63	0.3	0.3	1.00

a large variability in the gradients. Larger variability occurred in non-convective than in convective areas.

5.3.2 Probability of magnitudes of gradients

Cumulative frequency distributions were computed without regard to convective areas for gradients over 315-, 630-, and 944-km distances. As was done for AVE II and AVE IV (McCown and Scoggins, 1977), the distributions at each level were plotted on probability graph paper.

Cumulative frequency distributions of gradients are shown in Figs. 5.2, 5.3, 5.4, and 5.5 for geopotential height, temperature, wind speed, and mixing ratio, respectively. The geopotential height frequency distributions generally exhibit an increase in the magnitude of the gradients with height. The temperature gradients are irregularly distributed with the mean gradients of temperature decreasing with height; however, the largest 10% of the gradients at 500 mb are as large as the largest 10% at 850 mb, even though 50% of the gradients at 500 mb are $3^{\circ}/315$ km or smaller, while only 20% of the gradients at 850 mb are only $3^{\circ}/315$ km or less. Plots of the frequency distributions of wind speed gradient reveal a tendency toward larger gradients as higher levels are considered, but the largest 15% of the gradients at 500 mb are stronger than the largest 15% of the gradients at 200 mb. The mixing ratio gradients are also somewhat irregularly distributed, though the decrease in the magnitude of the gradient with height should be noted. At 850 and 700 mb, 80% of the gradients were less than $1.5 \text{ gm kg}^{-1} (315 \text{ km})^{-1}$, while the maximum values were 5.6 and $4.4 \text{ gm kg}^{-1} (315 \text{ km})^{-1}$, respectively.

5.3.3 Magnitudes of gradients in the vicinity of convection

The mean magnitudes of gradients were calculated for areas before and after convection and were compared to the respective storm areas, as was done previously for AVE II and AVE IV. The results from this investigation are presented in Table 5.2.

Except at 200 mb, geopotential height gradients increased as the storms developed and the maximum gradients occurred in the poststorm areas. At 200 mb, the maximum height gradients occurred just after the storms had formed. Temperature gradients were largest generally during the storms, except at 850 mb where the maximum gradients occurred in the poststorm areas. Maximum wind speed gradients at 850 and 700 mb occurred either before the storms or immediately after the storms formed, but at 500 and 200 mb the maximum gradients occurred in the rear portion of the storm area or in the poststorm region. Maximum mixing ratio gradients at all levels occurred generally in the storm or poststorm areas.

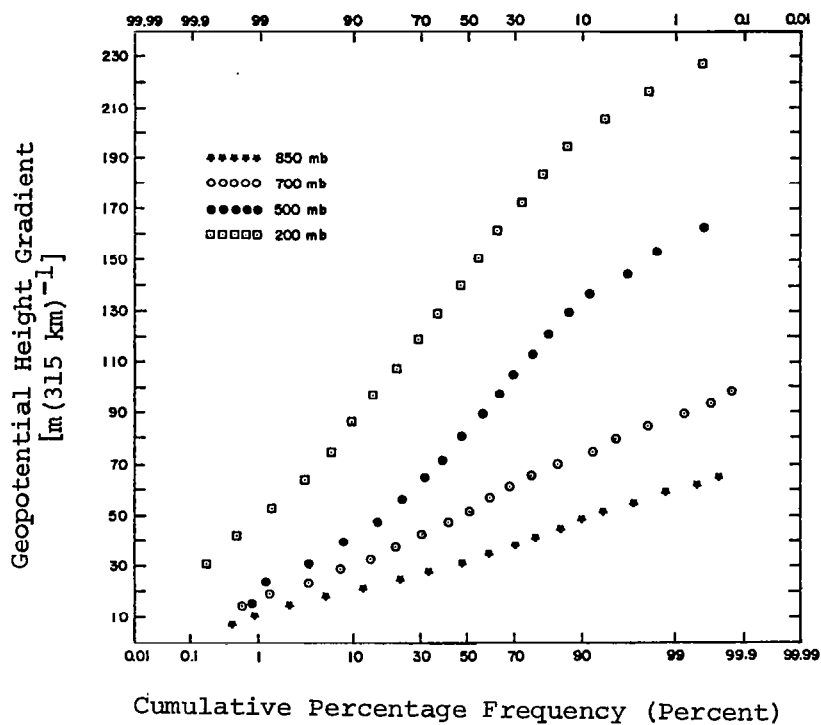


Fig. 5-2. Cumulative frequency distributions of geopotential height gradients.

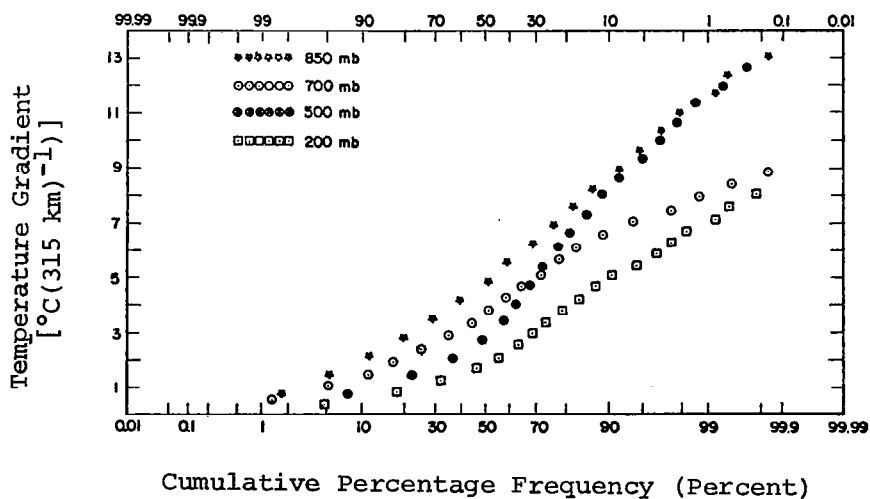


Fig. 5-3. Cumulative frequency distributions of temperature gradients.

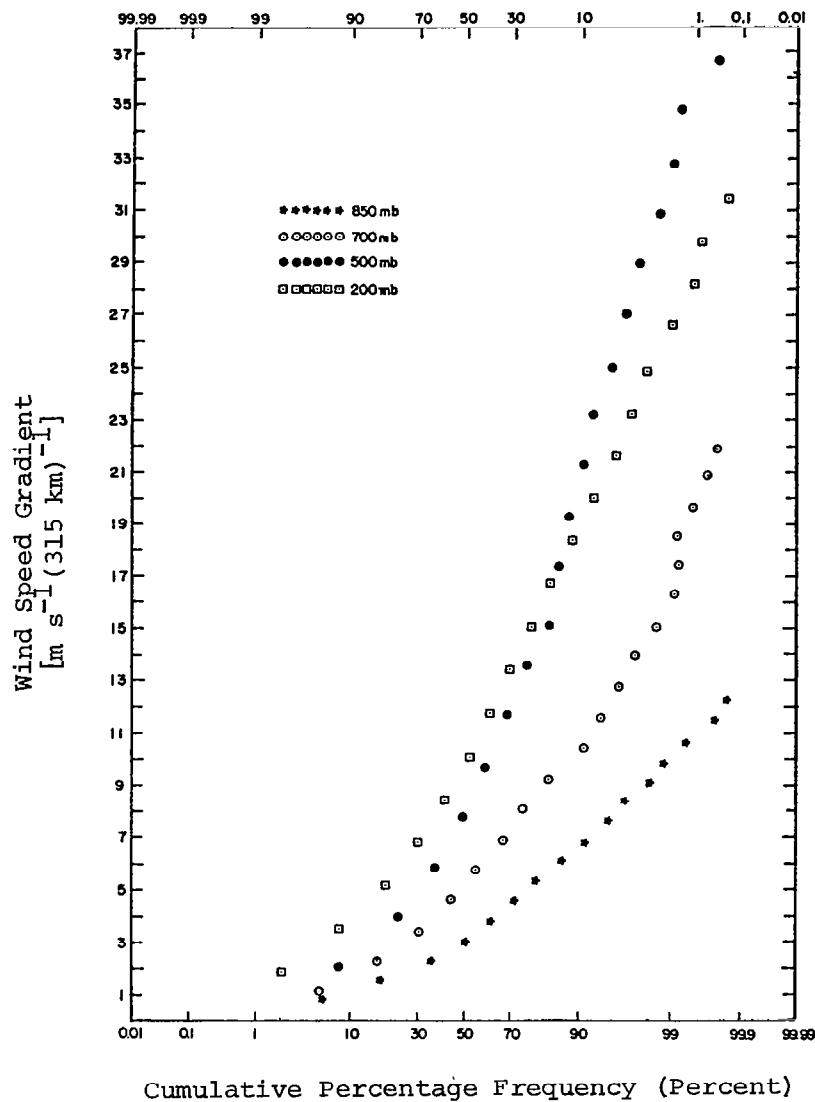


Fig. 5-4. Cumulative frequency distributions of wind speed gradients.

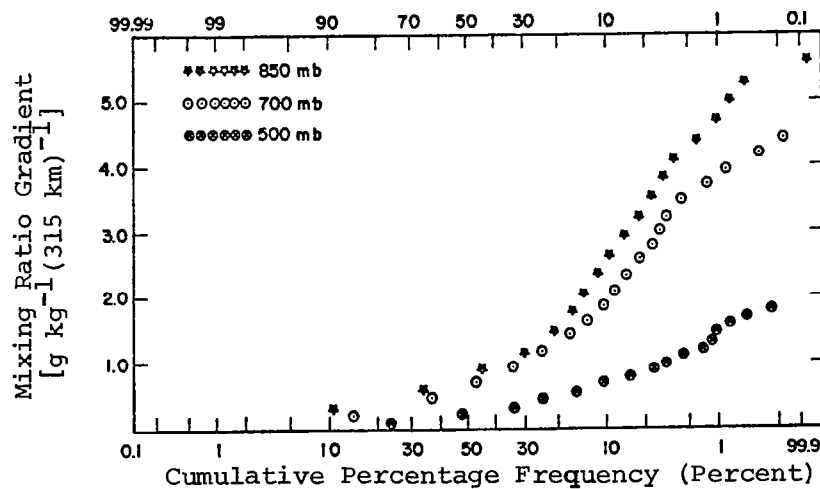


Fig. 5-5. Cumulative frequency distributions of mixing ratio gradients.

Table 5.2. Means of gradients in AVE III over areas in which the status of convection changed.

	Prestorm - Storm (Means of Gradients)		Storm - Poststorm (Means of Gradients)	
	Prestorm (MDR \leq 3)	Storm (MDR \geq 4)	Storm (MDR \geq 4)	Poststorm (MDR \leq 3)
Geopotential Height	[m (315 km) $^{-1}$]		[m (315 km) $^{-1}$]	
850 mb	22.9	(16) *	29.2	(18) *
700 mb	42.3	26.8	50.9	30.6
500 mb	62.5	50.5	73.0	55.2
200 mb	122.1	74.1	137.7	80.4
		142.1		136.4
Temperature	[°C (315 km) $^{-1}$]		[°C (315 km) $^{-1}$]	
850 mb	3.6	3.9	4.3	5.0
700 mb	2.6	3.1	2.9	3.0
500 mb	1.8	2.0	2.4	1.7
200 mb	2.4	3.0	2.8	2.0
Wind Speed	[m s $^{-1}$ (315 km) $^{-1}$]		[m s $^{-1}$ (315 km) $^{-1}$]	
850 mb	3.9	5.1	3.3	3.6
700 mb	6.8	5.9	6.4	6.7
500 mb	9.8	11.5	11.7	13.1
200 mb	9.9	11.2	12.6	12.3
Mixing Ratio	[g kg $^{-1}$ (315 km) $^{-1}$]		[g kg $^{-1}$ (315 km) $^{-1}$]	
850 mb	2.8	2.1	3.2	2.5
700 mb	2.2	2.8	1.8	2.2
500 mb	0.6	0.5	0.8	0.8

*Number of grid points

Analyzed fields of the gradients are shown to give some idea of the structure of the gradient patterns in AVE III. As was done for the previous AVE experiments, only 850 and 500 mb fields for the time in which the maximum convection occurred will be presented. In AVE III the most widespread convection occurred at 2100 GMT 6 February 1975, and the MDR composite for this time is shown in Fig. 5.6.

Fig. 5.7 shows the analyzed height gradient fields. The stippled areas on the analyzed charts indicate areas of convection. As was noted in Table 5.2, maximum height gradients near the areas of convection occurred following the storms. At 850 mb, the maximum gradients on the grid occur near central Iowa and are not associated with precipitation of any kind, but a secondary maximum occurs over southwest Georgia which appears to be associated with the convection. At 500 mb, the maximum gradients on the grid occur over central Georgia and Alabama and to the rear of the convective area.

Analyzed temperature gradient fields are presented in Fig. 5.8. At 850 mb the maximum gradients on the grid occur from northern Georgia southward into central Alabama and are positioned in the poststorm region, while over the convective area itself, the gradients are relatively weak. At 500 mb, the maximum gradients on the grid occur well away from any convective activity, while near the convection the gradients are relatively weak.

Figure 5.9 shows the analyzed gradient fields of wind speed. At 850 mb the wind speed gradient was relatively weak throughout most of the AVE III grid. The strongest gradients were only $10 \text{ m s}^{-1} (315 \text{ km})^{-1}$ and were occurring in the Texas Panhandle away from any convection. At 500 mb, a strong jet with speeds of 55 m s^{-1} lay from central Alabama into central North Carolina. Wind speed gradients of $35 \text{ m s}^{-1} (315 \text{ km})^{-1}$ were noted on the western side of the jet and near $20 \text{ m s}^{-1} (315 \text{ km})^{-1}$ between the jet and the convective area. Over the convective area itself, the gradients were about $10 \text{ m s}^{-1} (315 \text{ km})^{-1}$.

Analyzed fields of mixing ratio gradient are presented in Fig. 5.10. At 850 mb, the maximum gradients occurred ahead of the storms, but at most other time periods the maximum occurred to the rear of the storms. At 500 mb, the strongest mixing ratio gradients were occurring near the storms, but in general the largest gradients occurred in the rear portion of the storm area.

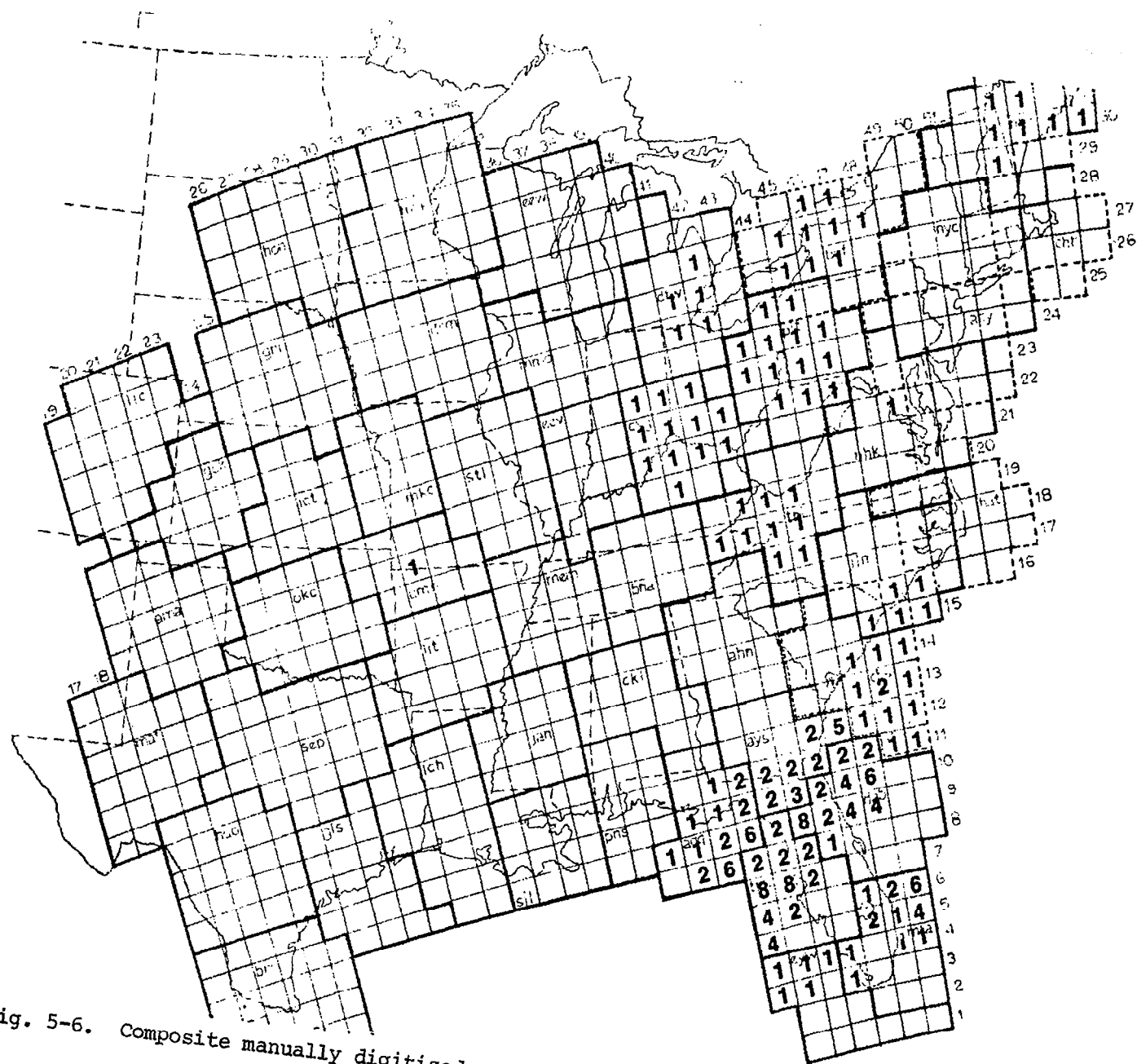
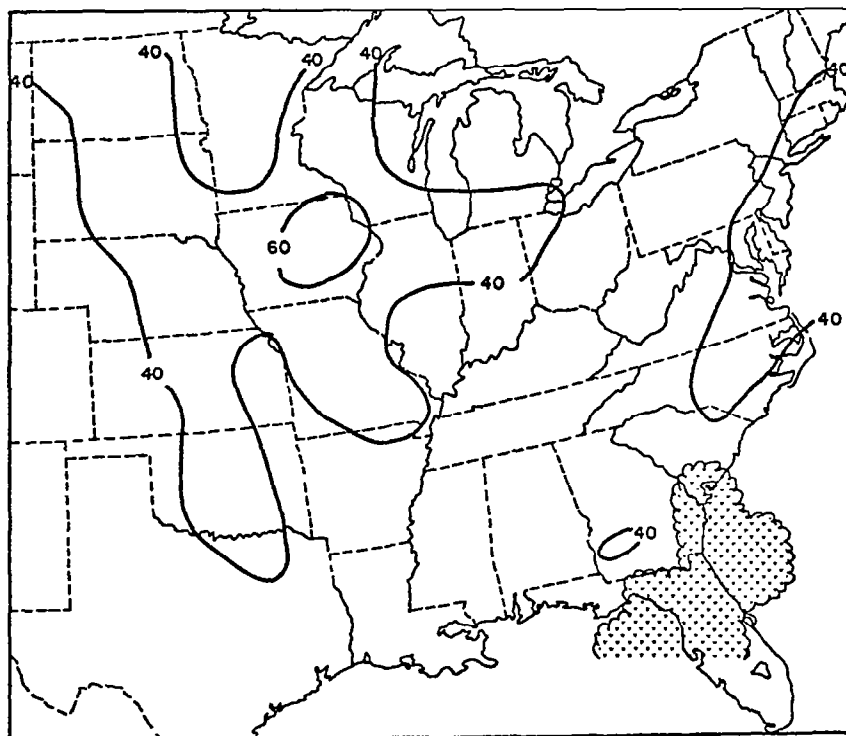
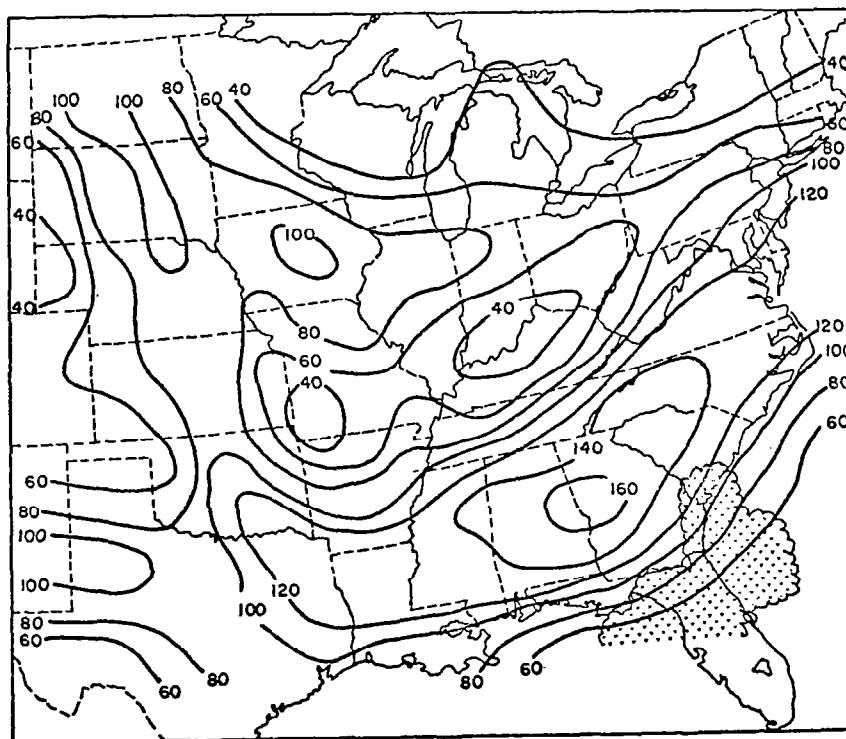


Fig. 5-6. Composite manually digitized radar (MDR) chart for 2100 GMT, 6 February 1975.

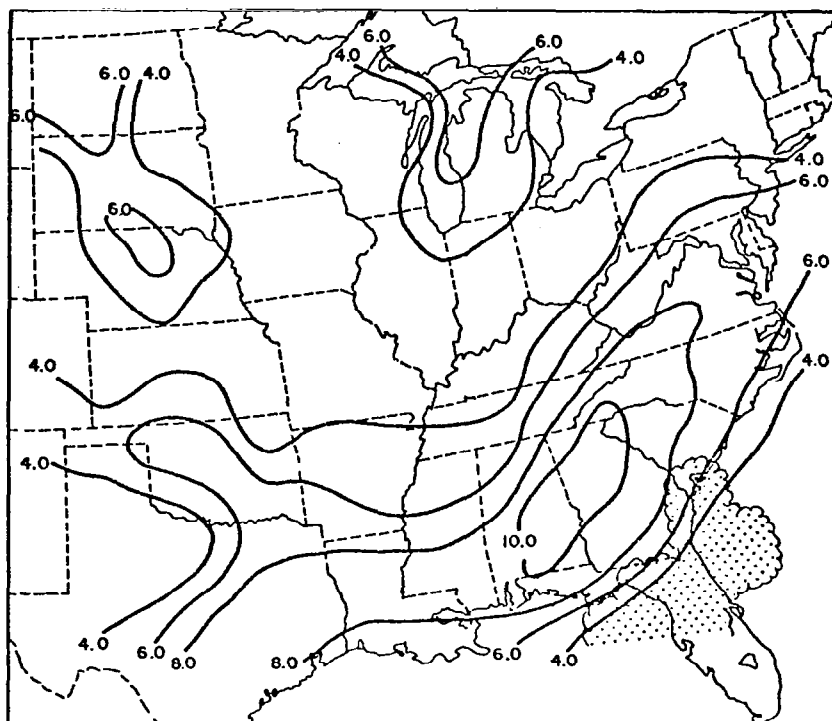


(a) 850 mb

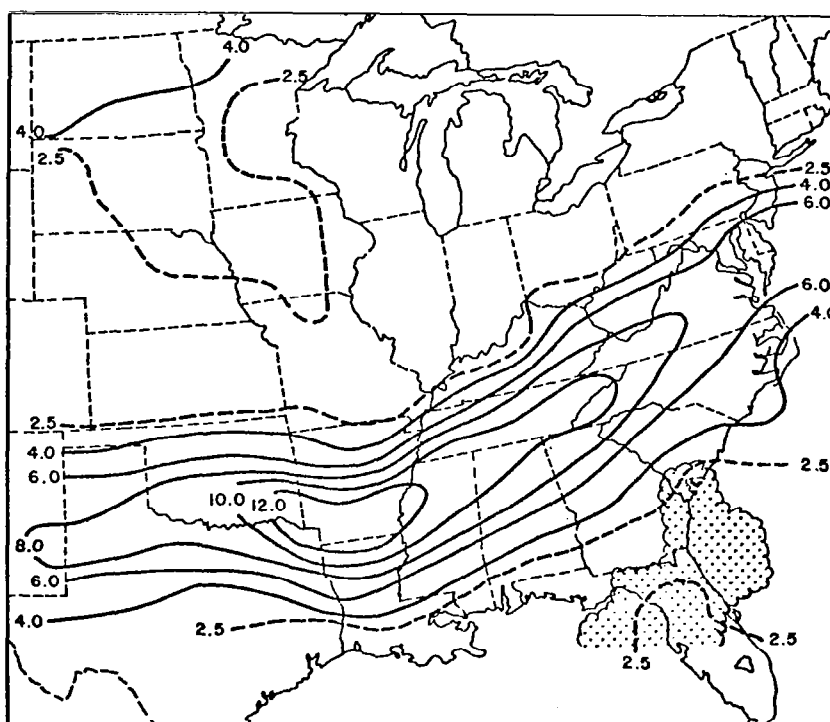


(b) 500 mb

Fig. 5-7. Geopotential height gradient fields [$m(315 km)^{-1}$] at 2100 GMT 6 February 1975.

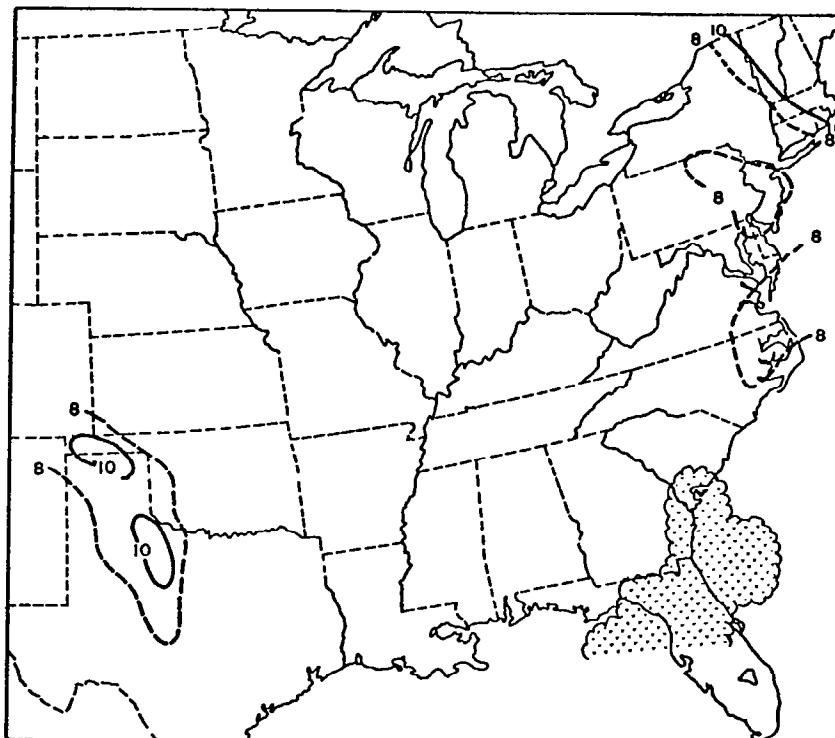


(a) 850 mb

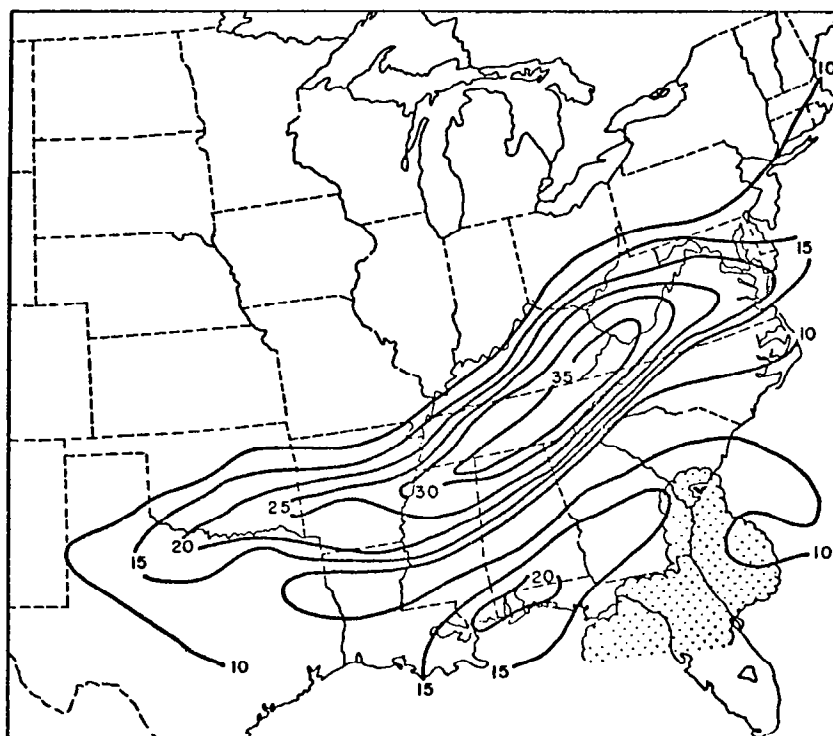


(b) 500 mb

Fig. 5-8. Temperature gradient fields [$^{\circ}\text{C}(315 \text{ km})^{-1}$] at 2100 GMT 6 February 1975.

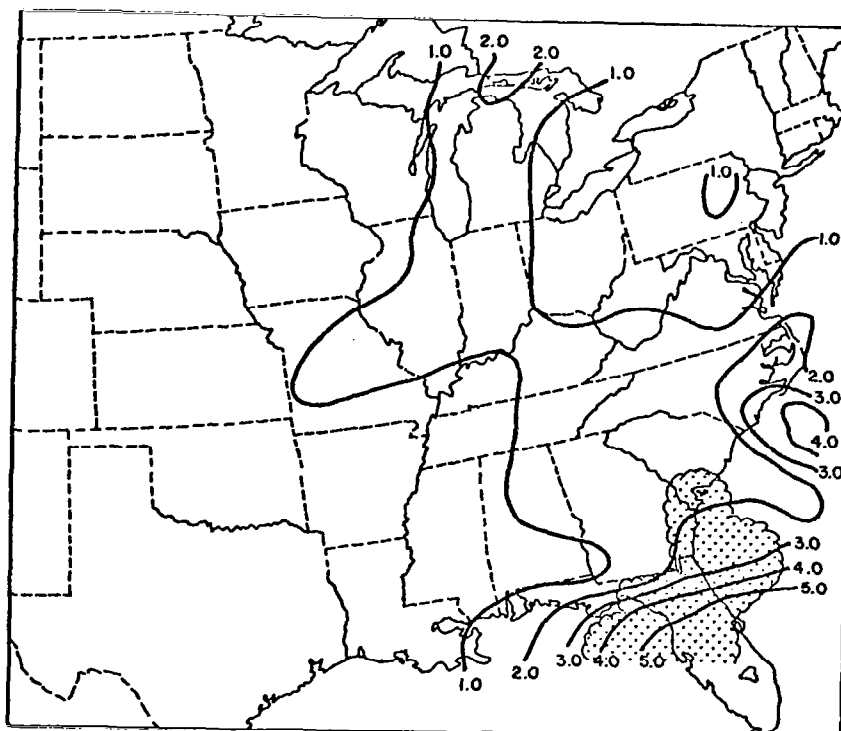


(a) 850 mb

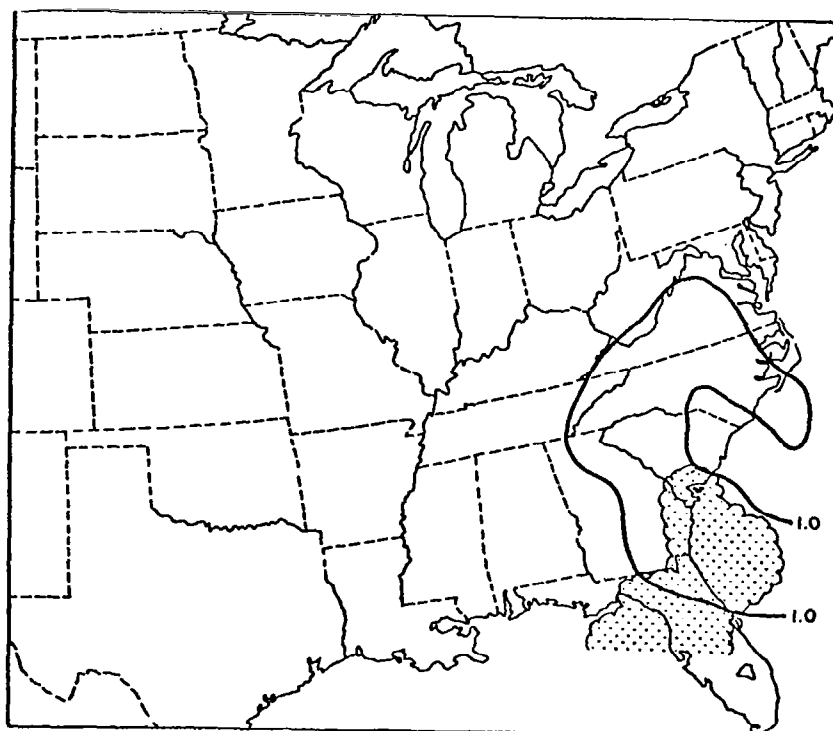


(b) 500 mb

Fig. 5-9. Wind speed gradient fields [$\text{m s}^{-1} (315 \text{ km})^{-1}$] at 2100 GMT 6 February 1975.



(a) 850 mb



(b) 500 mb

Fig. 5-10. Mixing ratio gradient fields [$\text{g kg}^{-1} (315 \text{ km})^{-1}$] at 2100 GMT 6 February 1975.

5.4 Comparison of AVE II, AVE III, and AVE IV

5.4.1 Convective and nonconvective areas

In a previous report (McCown and Scoggins, 1977), the differences in the synoptic situations of AVE II and AVE IV have been discussed, and it was concluded that these differences had an impact upon the gradients near the convective areas. The synoptic situations of AVE II and AVE III were similar in that convection was occurring ahead of a major trough with seasonably cold air pushing southeastward over most of the United States.

Since the synoptic situations of AVE II and AVE III were so similar, it may be expected that the two cases would agree as to whether gradients of a particular parameter were larger in convective or nonconvective areas of each experiment. To a large degree this was true. Mean geopotential height gradients at 700, 500, and 200 mb, and mean temperature gradients at 850, 700, and 500 mb were larger in the nonconvective areas than in convective areas in both AVE II and AVE III. Many of these results should be expected since the convection was occurring in conjunction with the polar front. Since convection occurred ahead of and near the surface frontal position and cold fronts slope so that warm air overlies colder air, the upper level front sloped away from the convection. Thus, temperature and consequently height gradients were larger in the nonconvective areas. Mean 850 and 700 mb wind speed and 700 and 500 mb mixing ratio gradients were larger in convective than nonconvective regions in both cases.

AVE IV contained an entirely different synoptic situation than was present in the other AVE experiments. Consequently, there were major differences between AVE IV and the other AVE experiments on the question of whether the convective or nonconvective areas had the larger mean gradients. In AVE IV, there was no strong major trough aloft and the convective areas all formed along weak fronts and eventually moved eastward as pre-frontal thunderstorms. Height, temperature, and mixing ratio gradients at all levels were larger or equal in the convective regions than elsewhere in AVE IV. Wind speed gradients at 850 and 200 mb in AVE IV were larger in the convective areas, but at 700 and 500 mb the mean gradients were larger in the nonconvective areas.

Comparing the magnitudes of the gradients in the convective and nonconvective areas of each AVE experiment with the other AVE experiments is also instructive. Comparing Tables 1 and 2 in a previous report by McCown and

Scoggins (1977) with Table 5.1 of this report, one finds that in the nonconvective areas the temperature gradients at 850, 700, and 500 mb and consequently the height gradients at 500 and 200 mb, were largest in AVE III, but mixing ratio gradients in the nonconvective areas were smallest in that experiment. Considering the fact that AVE III is a mid-winter situation with strong temperature contrasts and very dry air, such results are expected. Wind speed and mixing ratio gradients in the nonconvective areas were equal or larger at all levels in AVE II than in either of the other AVE experiments.

Comparing the mean gradients in the convective areas using the tables described above, one finds that the largest height, temperature (with the exception of 500 mb), and wind speed gradients in the upper two levels occurred in AVE III. In the lower two levels, the largest height gradients occurred in AVE II. At 850 mb, the largest wind speed gradients in the convective areas were present in AVE IV, indicating the presence of a low-level jet. As was the case in the nonconvective areas, the smallest mixing ratio gradients were found in AVE III and the largest in AVE II.

5.4.2 Magnitudes of gradients in the vicinity of convection

As was noted previously, the synoptic situations of AVE II, particularly in the midwest, and that of AVE IV were similar. The synoptic situations in the southeast portion of AVE II and AVE IV differ from the others in that squall lines formed in those regions without major troughs in the upper levels following them. These differences in the synoptic conditions caused minor variations in the pattern of the magnitude of the gradients as the status of convection changed.

By comparing Tables 8 and 9 of the previous report (McCown and Scoggins, 1977) with Table 5.2 of this report, it can be seen that the height gradients were largest in the poststorm areas at 850 and 500 mb in AVE III and the midwest United States in AVE II. Temperature gradients at 850 and 500 mb, wind speed gradients at 500 mb, and mixing ratio gradients at 850 mb were also largest in the rear portion of the storm area or in the poststorm region. Such results are suggestive of the polar front structure as described by Palmen and Newton (1969). The sloping baroclinic zone tends to be positioned near the baroclinic zone in the upper levels. Thus, wind speed gradients increase following the convection. Wind speed gradients at 850 mb were largest before the storms or in the storm's forward portion.

The main difference in gradient patterns between the frontal cases mentioned above and the squall line cases in the southeast United States region of AVE II and AVE IV occurs in height and wind speed gradients. In the squall line cases, maximum height gradients at 850 and 500 mb occurred before or during the storm, instead of afterwards as in the frontal cases. Temperature gradients in the squall line situations were largest during the storms at 850 mb, and during or after the storms at 500 mb. Maximum wind speed gradients at 850 mb occurred in the rear portion of the storm areas in the squall line cases as opposed to before or during the storms in the frontal cases. At 500 mb the largest wind speed gradients occurred in the poststorm region. The strongest mixing ratio gradients generally occurred in the rear portion of the storm areas or over the poststorm areas at both 850 and 500 mb, but at 850 mb in the southeast United States region of AVE II the mixing ratio gradients were strongest before the storms.

At 500 mb, both the squall line and frontal cases suggest that temperature, wind speed, and mixing ratio gradients are largest following the storms. Such a finding is consistent with results obtained from previous thunderstorm studies by Ninomiya (1971) and Miller (1967).

5.5 Magnitudes of Gradients versus Distance for AVE and HIPLEX Data

In order to obtain generalized information about expected magnitudes of gradients of atmospheric parameters versus distance, selected percentile values of the gradient magnitudes were plotted versus the distance over which the gradients were measured. In an effort to examine how gradients varied over shorter distances than was possible using synoptic-scale rawinsonde data from the three AVE experiments, data from the Texas HIPLEX Mesoscale Experiment (Scoggins and Wilson, 1976) of summer 1976 were used to supply information about mesoscale gradients.

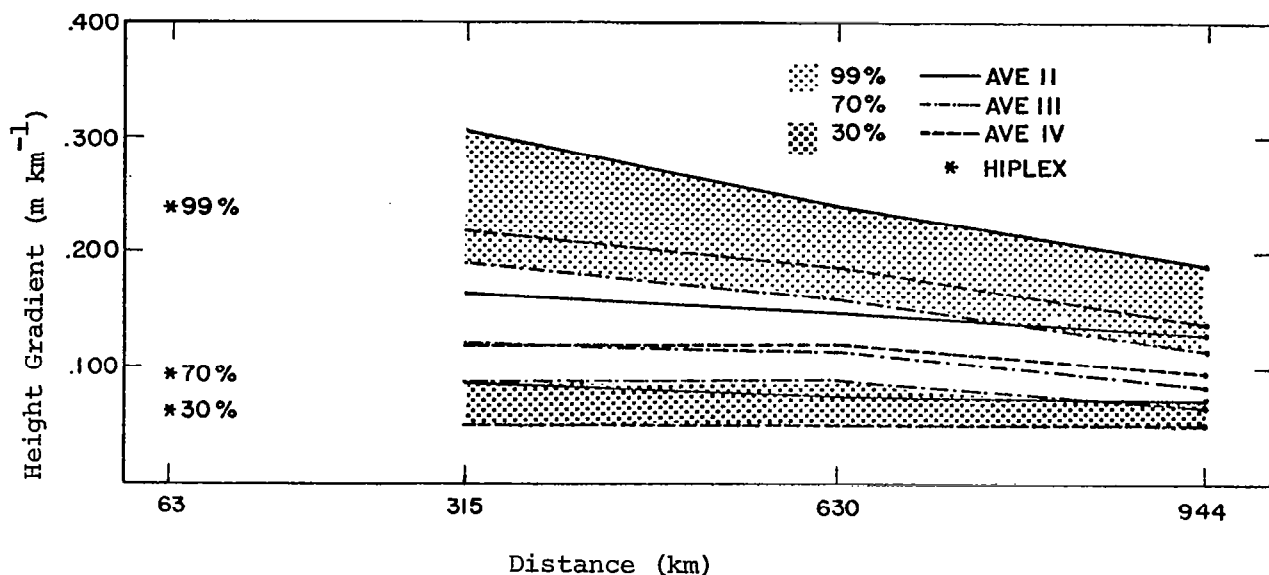
The HIPLEX area contained a mesoscale network of surface stations plus four rawinsonde stations. Three of the rawinsonde stations (Midland, Post, and Robert Lee) nearly form an equilateral triangle, and Big Spring is located near the triangle's center. An overall-gradient value was computed for each observation time over a distance of 63 km near the center of the triangle for the same parameters and levels considered during the AVE investigations. Nine of the fourteen operational days (June 22, 23, 25, and 28 plus July 1, 3, 8, 10, and 11) were selected, and the gradient values were determined

for each of five times beginning at 1500 GMT and continuing at consecutive 3-h intervals until 0300 GMT the next day. With the exception of June 28, all the operational days were conducted when there was shower or thundershower activity in the general HIPLEX area. Due to the fact that HIPLEX was conducted during a summertime situation, the gradients should be expected to be somewhat weaker than the gradients encountered during the AVE experiments. The data reduction schemes of both HIPLEX and AVE are similar, using the same objective analysis technique.

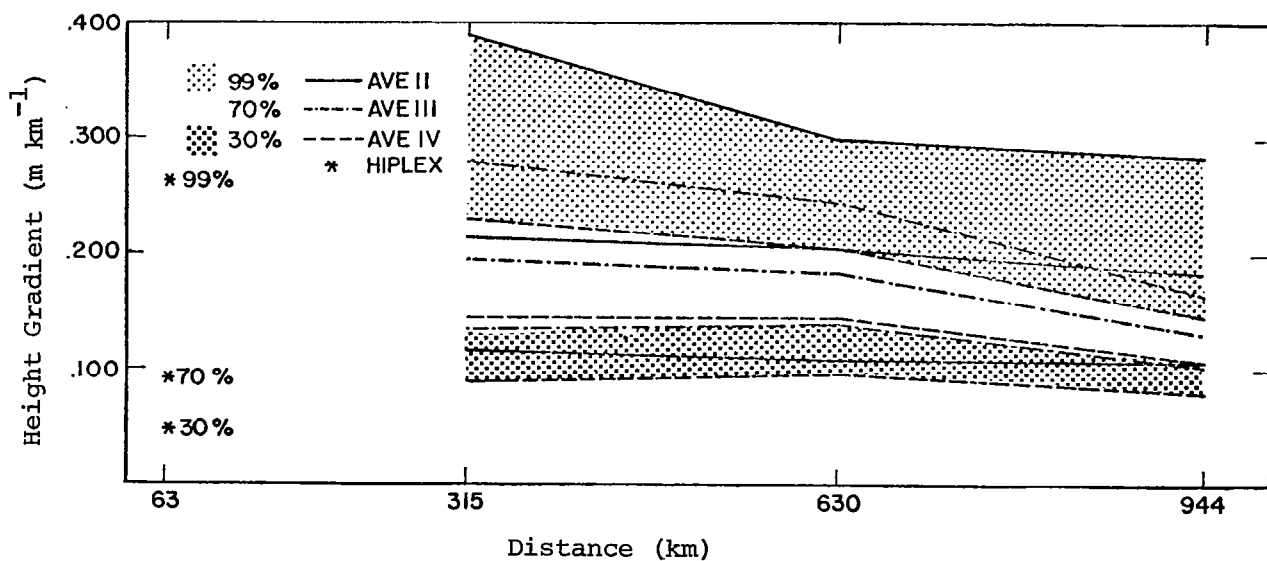
Figure 5.11 shows plots of the 30, 70, and 99 percentile values of height gradients versus distance for the 850-, 700-, 500-, and 200-mb levels. The chosen percentile values had to be spaced somewhat widely apart, and even then there was considerable overlapping of those values between the various AVE experiments. The plots reveal that height gradients for the AVE experiments presented a wider range of values over the 315-km distance than for the other distances. There was considerable overlapping of the different percentile values of the gradients computed over the 944-km distance and in the upper levels of the atmosphere. Such overlapping may be expected since the three AVE experiments represent widely-varying synoptic situations. The percentile values of the gradients computed for the HIPLEX area are considerably smaller than the simple extrapolation of the percentile curves developed for the AVE experiments. One obvious reason for this difference is that the HIPLEX gradients were computed during mid-summer when the gradients should be expected to be smaller.

Plots of percentile values of temperature gradient are shown in Fig. 5.12. As with height gradients, the percentile values overlapped when the gradients were considered over the larger distances and in the upper levels of the atmosphere. Especially wide bands of the 99 percentile value are noted at 500 and 200 mb, indicating a wide variability of the expected maximum temperature gradients at those levels. At nearly all levels, the HIPLEX gradient percentile values occur within the lower values of the appropriate percentile "envelope" established by extrapolation of the curves from the AVE experiments, which may be expected because of the lower-gradient summer situation occurring during HIPLEX.

Figure 5.13 shows plots of percentile values of wind speed gradient versus distance for each of the four levels. Unlike the height and temperature gradient percentile envelopes, the wind speed gradient percentile values do not



(a) 850 mb



(b) 700 mb

Fig. 5-11. Plots of selected percentile values of height gradient versus distance for different pressure levels.

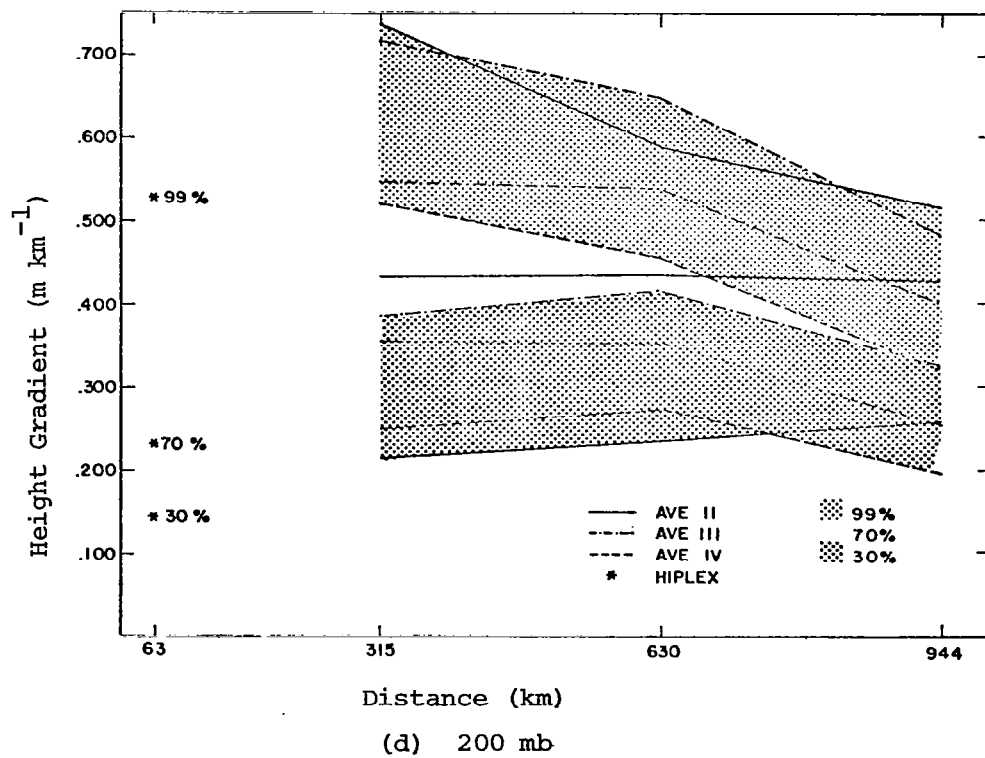
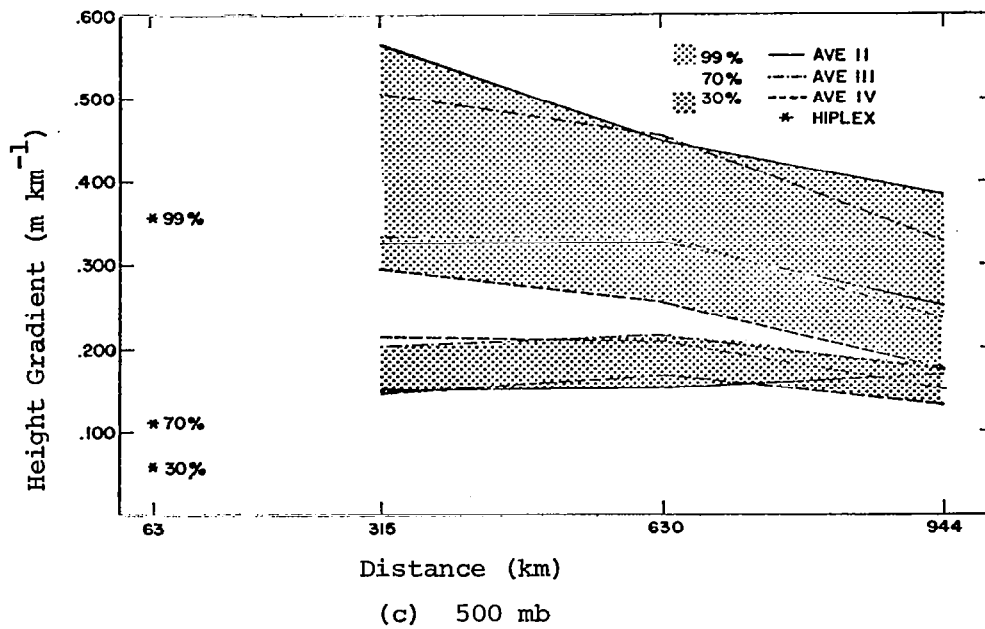
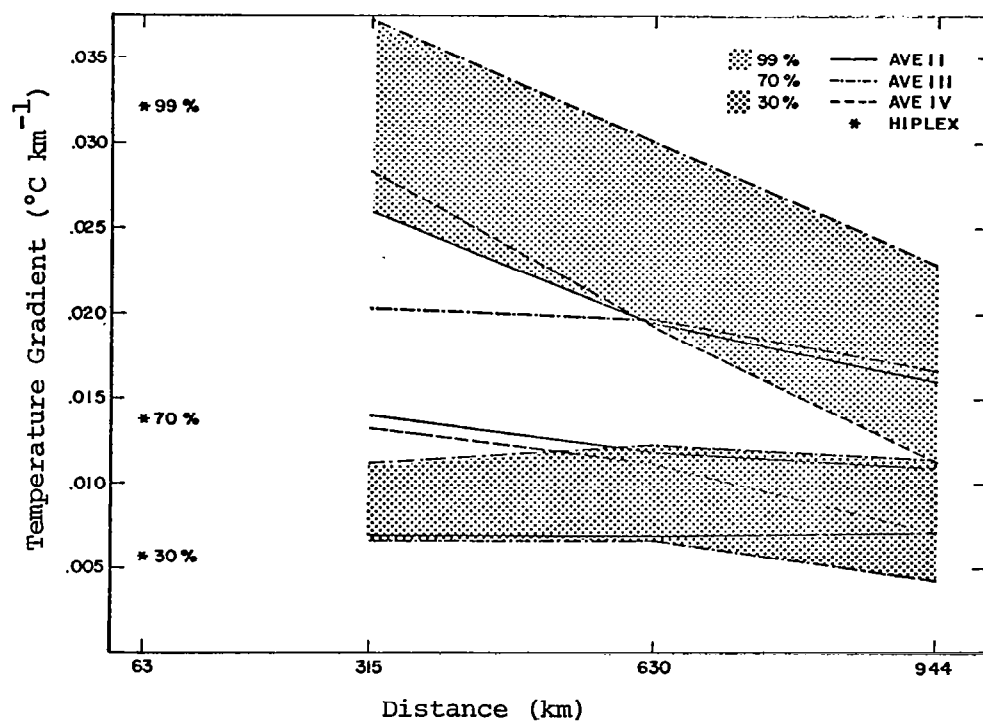
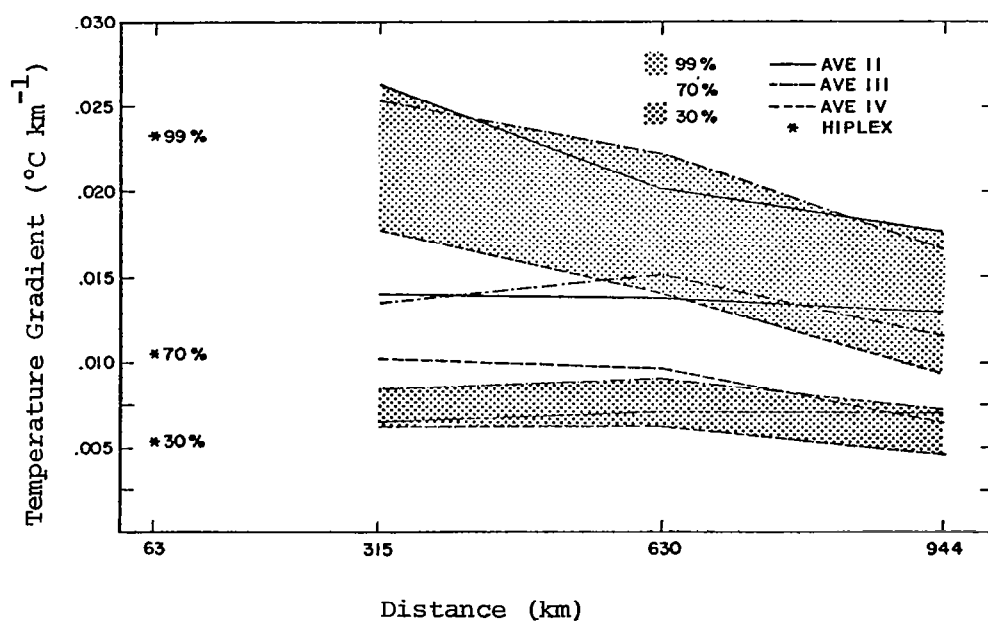


Fig. 5-11. (Continued)



(a) 850 mb



(b) 700 mb

Fig. 5-12. Plots of temperature gradient values versus distance for different levels.

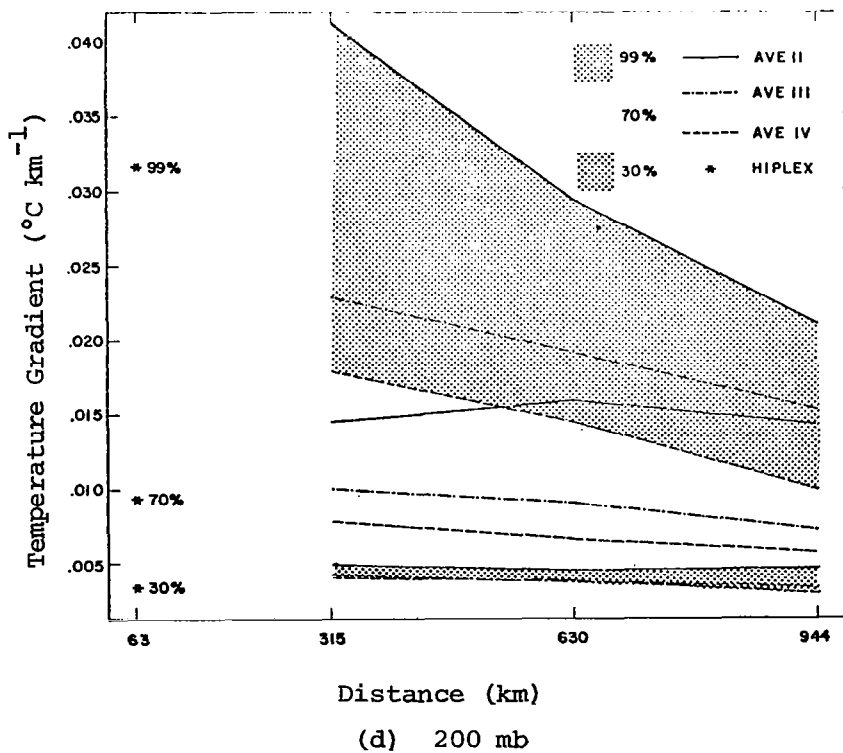
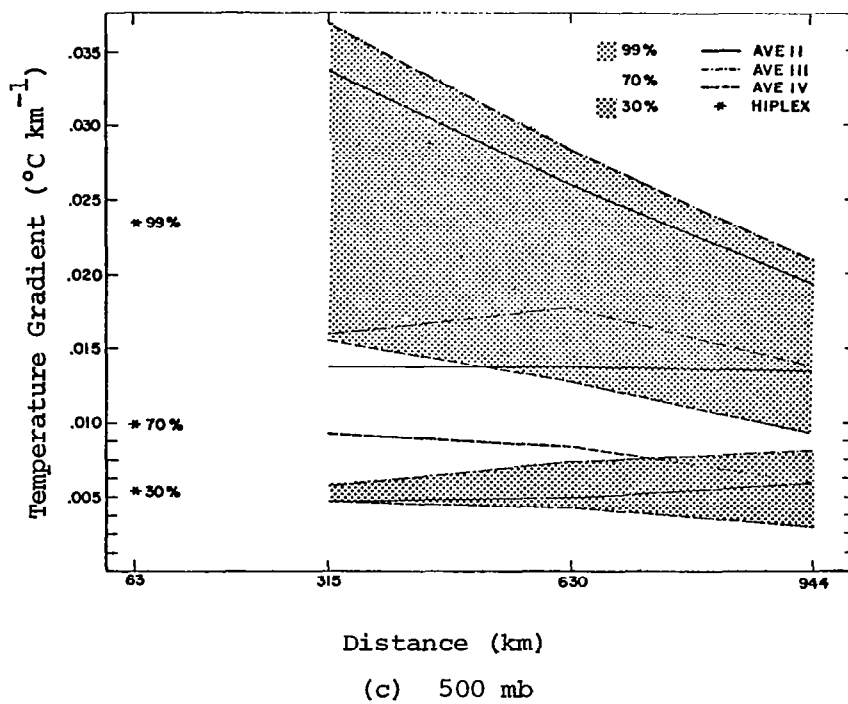


Fig. 5-12. (Continued)

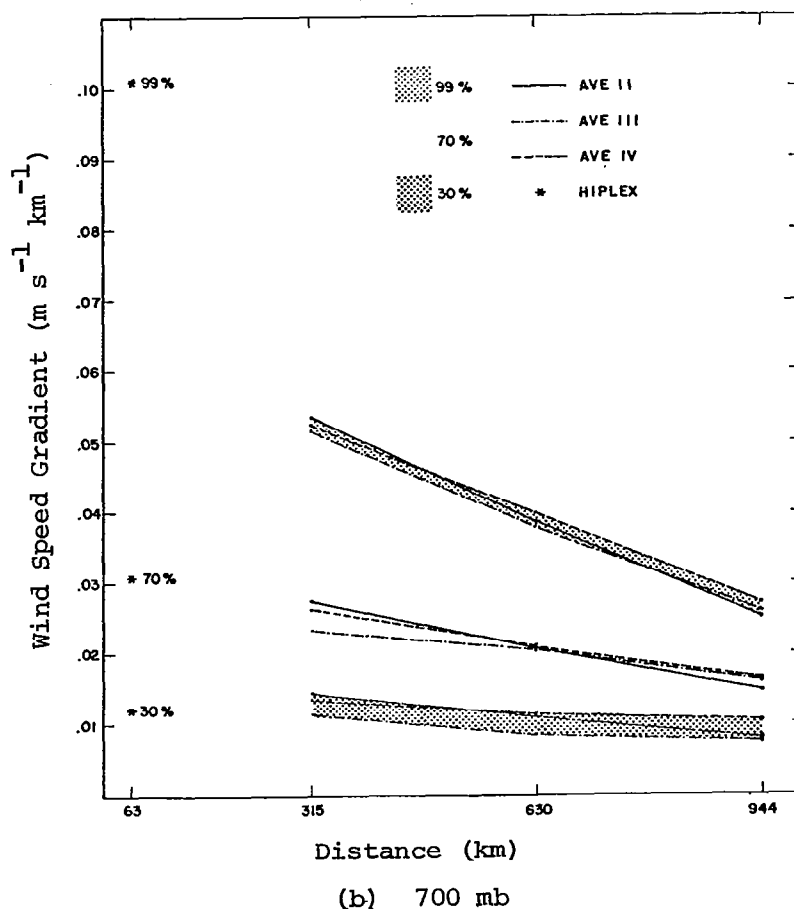
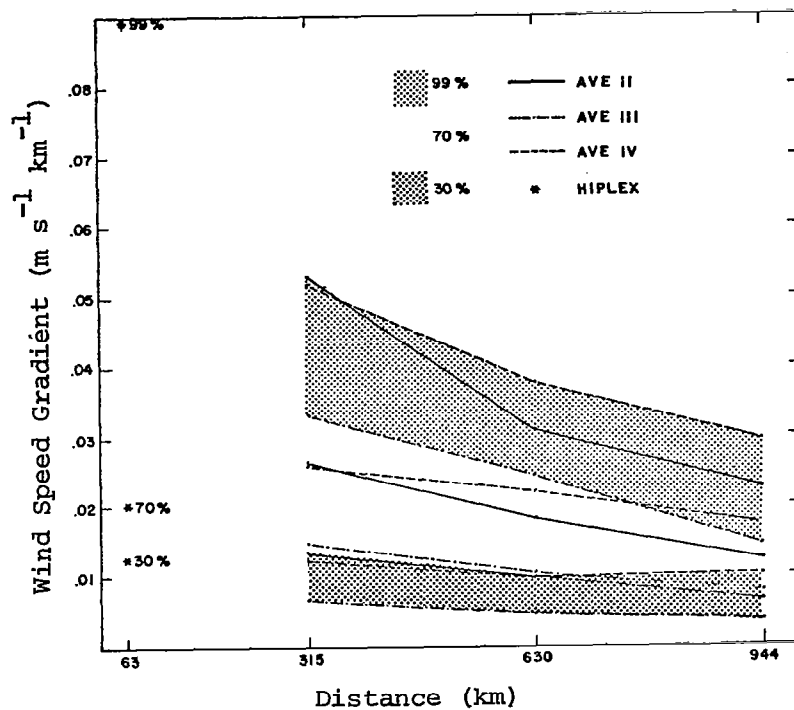


Fig. 5-13. Plots of wind speed gradient values versus distance for different levels.

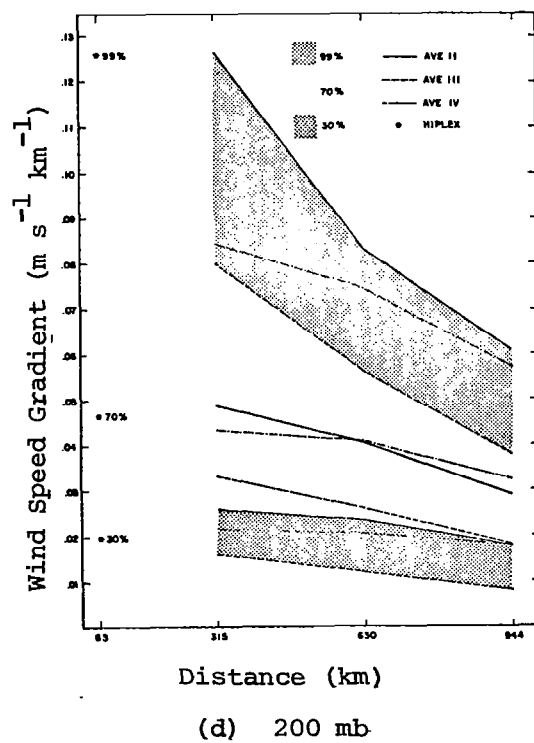
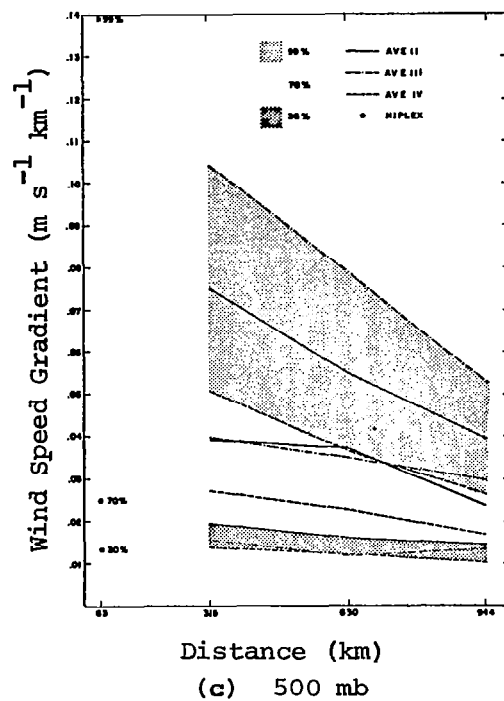


Fig. 5-13. (Continued)

overlap to any appreciable degree. The 99 percentile values get much larger with height and over shorter distances indicating the presence of limited areas with high horizontal speed shear. As with the temperature gradient values, the HIPLEX wind speed gradient percentile values generally occur within the extrapolated envelope values established by the AVE experiments. The 99 percentile values are an exception to this with the HIPLEX value in all cases except 200 mb being larger than expected from the AVE curves, indicating small areas of very high speed shear. The percentile envelopes established at 700 mb by the AVE experiments are extremely narrow and judging from the curves at other levels, should be much broader.

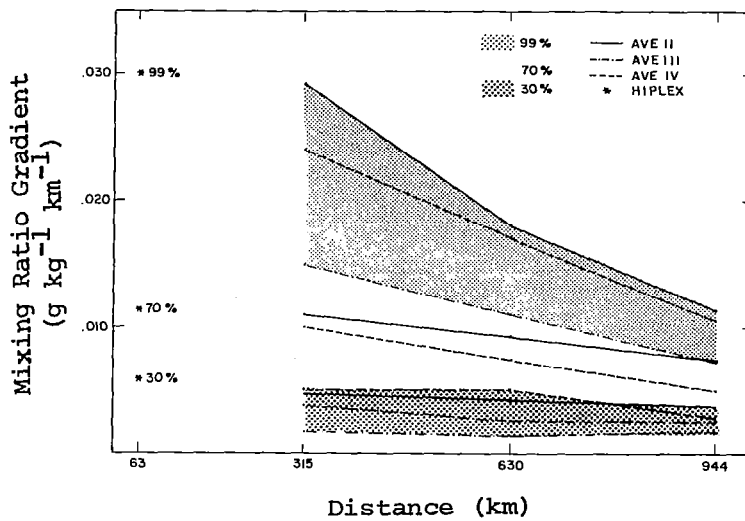
Percentile values of mixing ratio gradient versus distance are given in Fig. 5.14. Considerable overlap of the 30 and 70 percentile envelopes occurs at all levels indicating a wide variability of the gradient values in varying synoptic situations. The HIPLEX percentile values are on the upper limits of the extrapolated envelopes established by the AVE curves. This is expected since the HIPLEX region is located in an area affected by the southwest dry-line phenomena where large mixing ratio gradients occur.

In conclusion, the 30, 70, and 99 percentile envelope values established by the three AVE experiments are representative of the gradient distributions expected in the atmosphere. The fact that the percentile values were obtained from two high-gradient situations (AVE II and AVE III), and one fairly low-gradient situation (AVE IV), indicates these envelopes should be representative of most situations. Furthermore, since the HIPLEX percentile values (with the exception of height gradients) generally fall within the envelopes established by the AVE experiments, it appears that the AVE curves may be validly extended down to gradient distances of 60 km. In all cases, except for height gradients, the mean gradients tend to increase as smaller distances are considered.

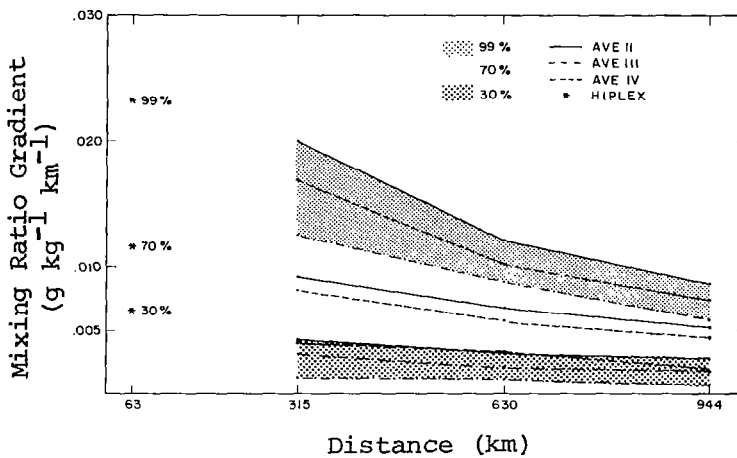
5.6 Summary and Conclusions

An analysis of the gradients of four atmospheric variables was performed using AVE III data. The procedure applied was exactly the same as was done for AVE II and AVE IV data.

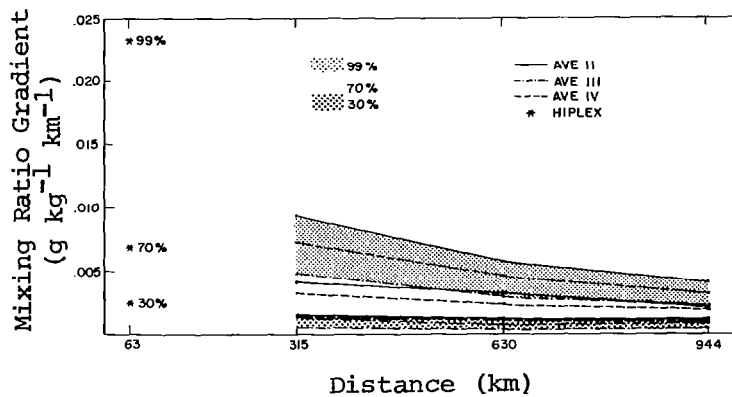
The conclusions reached using AVE III data are essentially the same as was reached by a study of AVE II and AVE IV. In general, the cumulative frequency distributions for each parameter are usually similar in shape, but not necessarily in magnitude. Mixing ratio gradients are generally largest near convective areas, and wind speed gradients at 850 mb tend to be largest



(a) 850 mb



(b) 700 mb



(c) 500 mb

Fig. 5-14. Plots of mixing ratio gradient values versus distance for different levels.

near storms. Except for wind speed gradients at 850 mb, the gradients of all parameters at 850 and 500 mb are larger following convection if the storms are frontal in nature. In the case of squall lines, the largest gradients occur during or after the storms with the exception of 850 mb height gradients, which are largest ahead of the convection.

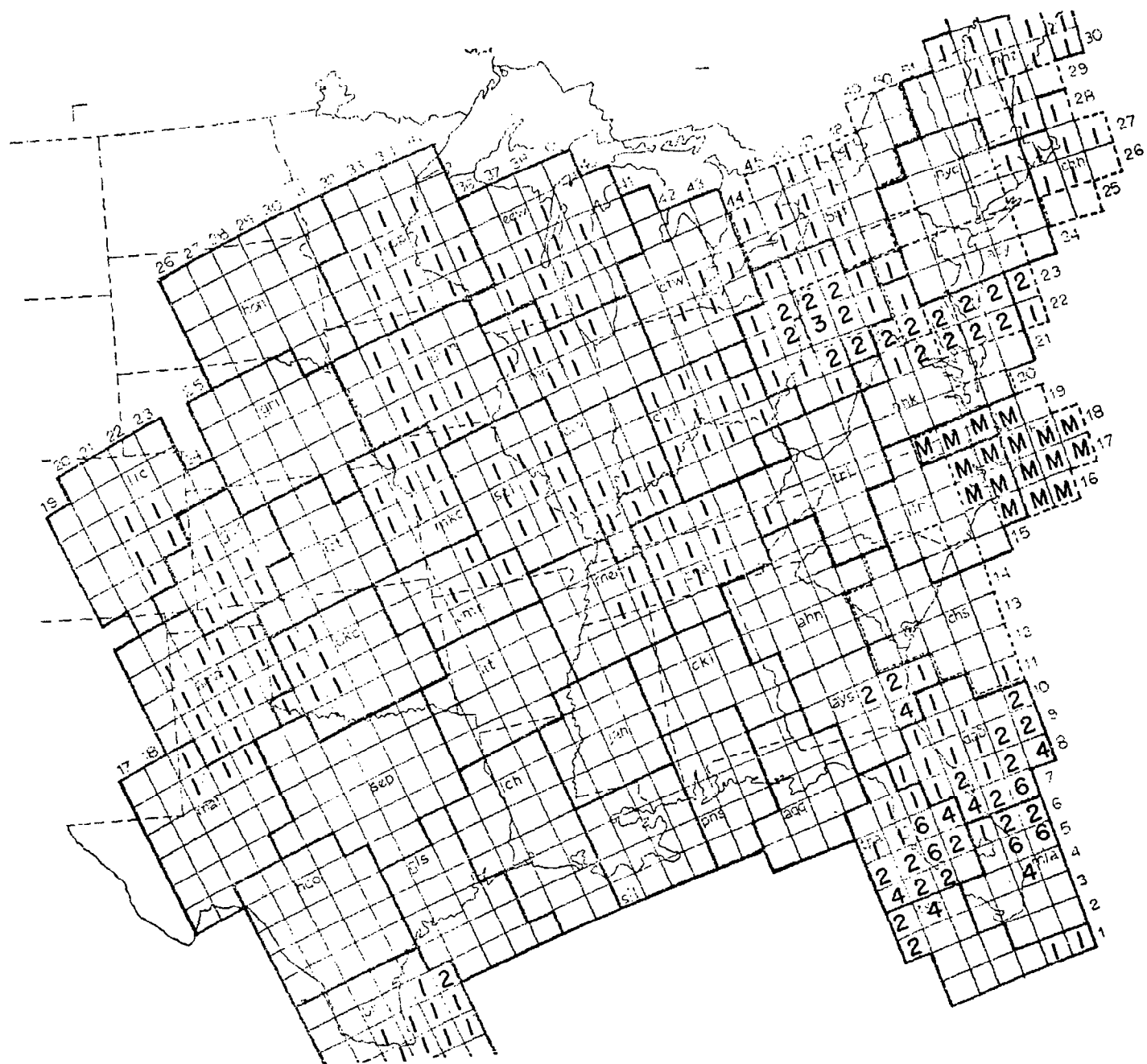
Plots of percentile frequency values versus the distance over which the gradients were measured indicate on the basis of HIPLEX data that the gradients of most parameters continue to increase down to distances of 60 km. The percentile values selected tended to overlap when long distances and upper atmospheric levels were considered.

5.7 References

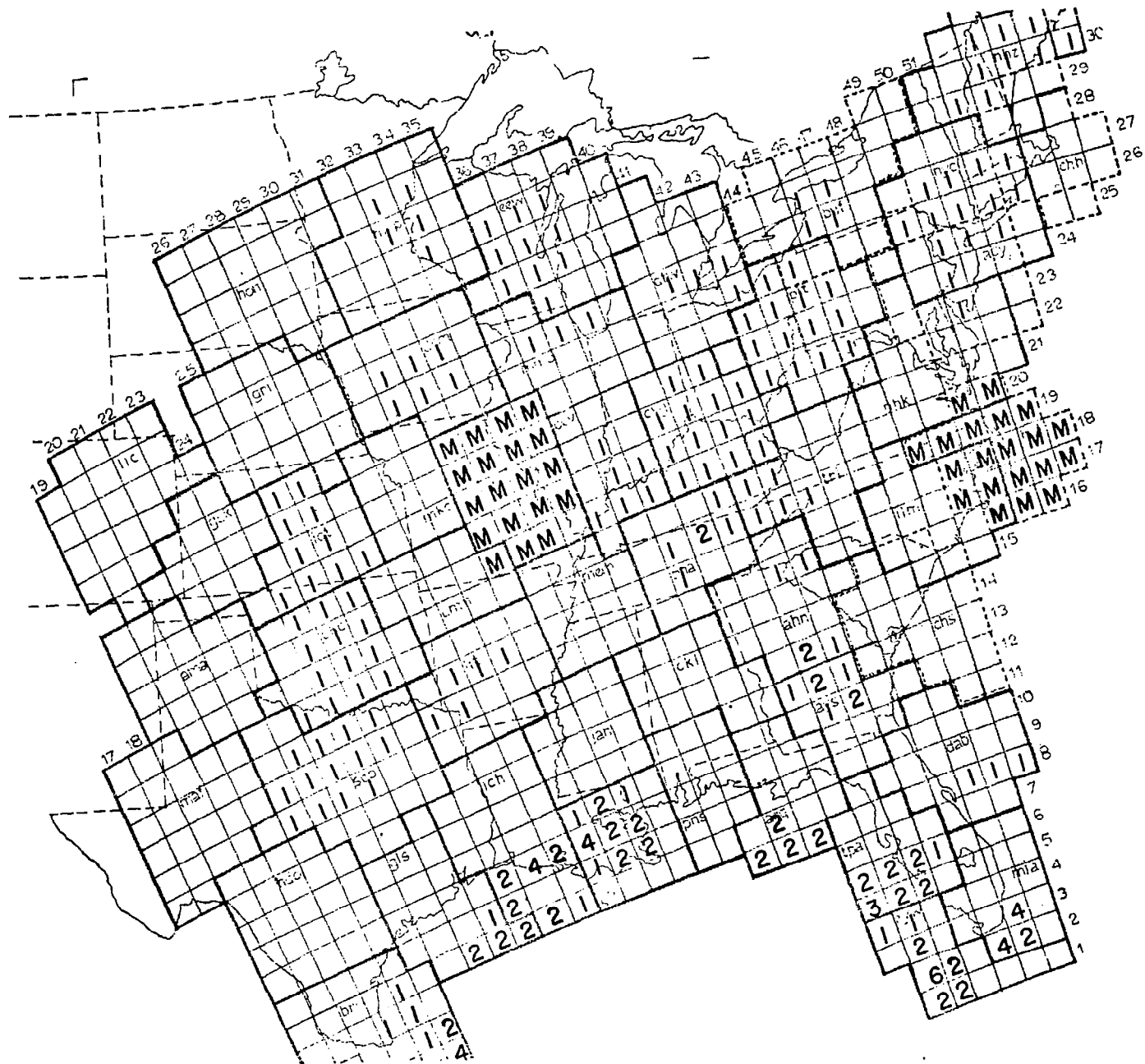
- McCown, M. S., and J. R. Scoggins, 1977: Gradients of meteorological parameters in convective and nonconvective areas. NASA CR-2818, NASA Marshall Space Flight Center, Huntsville, Alabama, 86 pp.
- Miller, R. C., 1967: Notes on analysis and severe-storm forecasting procedures of the military weather warning center. AWS Tech. Report 200, 170 pp.
- Ninomiya, K., 1971: Mesoscale modification of synoptic situations from thunderstorm development as revealed by ATS and aerological data. J. Appl. Meteor., 10, 1103-1121.
- Ostle, B., and R. W. Mensing, 1975: Statistics in Research, Ames, Iowa, The Iowa State University Press, 596 pp.
- Palmen, E., and C. W. Newton, 1969: Atmospheric Circulation Systems, New York, Academic Press, 603 pp.
- Saucier, W. J., 1955: Principles of Meteorological Analysis, Chicago, The University of Chicago Press, 438 pp.
- Scoggins, J. R., and G. S. Wilson, 1976: Texas HIPLEX Mesoscale Experiment-Summer 1976: Data Tabulation, Texas Water Development Board Contract No. 14-60025.

APPENDIX

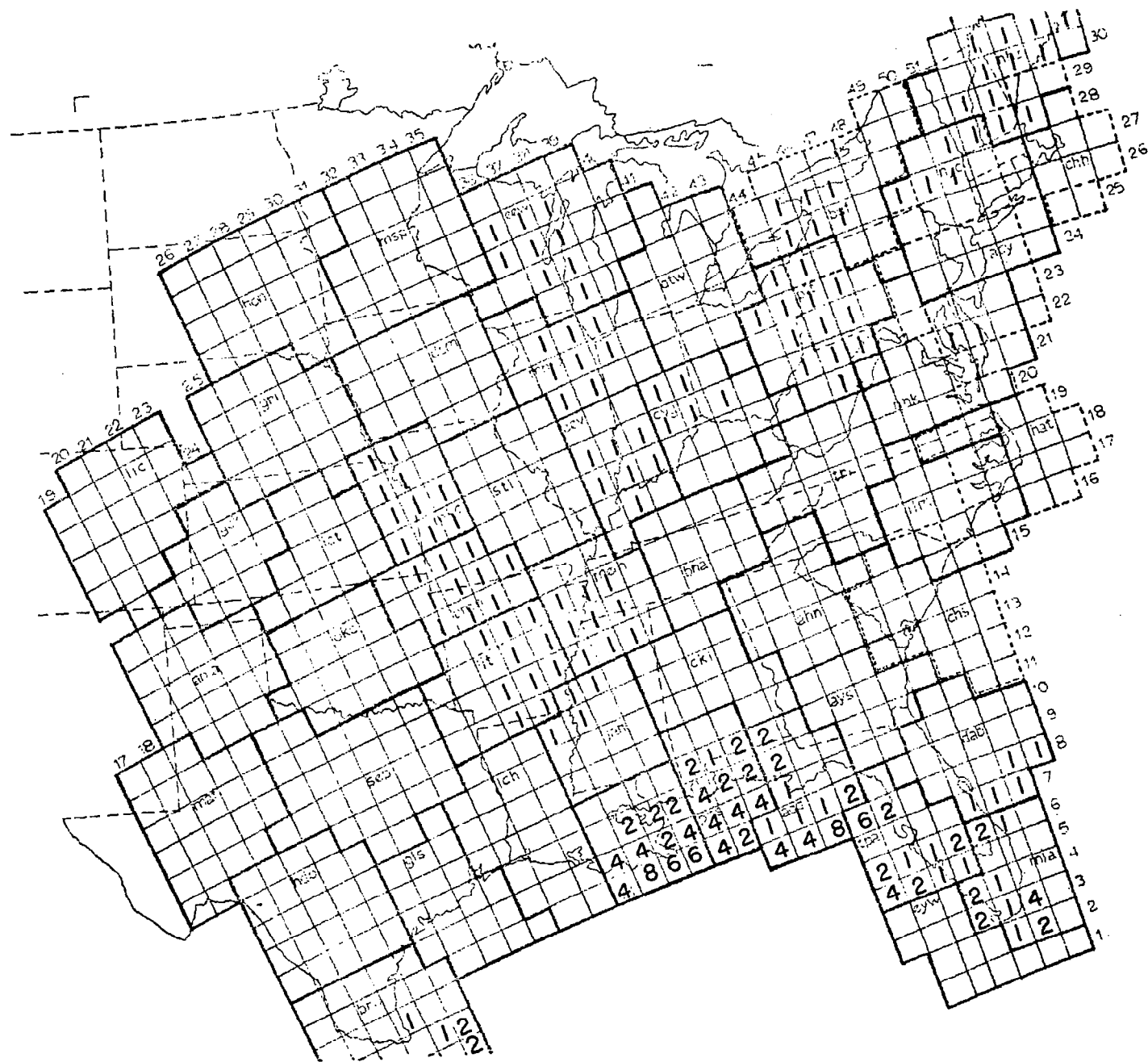
Composite MDR charts for all time periods of AVE III.



Composite MDR chart for 2300, 0000, and 0100 GMT 6 February 1975.



Composite MDR chart for 0500, 0600, and 0700 GMT 6 February 1975.



Composite MDR chart for 1100, 1200, and 1300 GMT 6 February 1975.

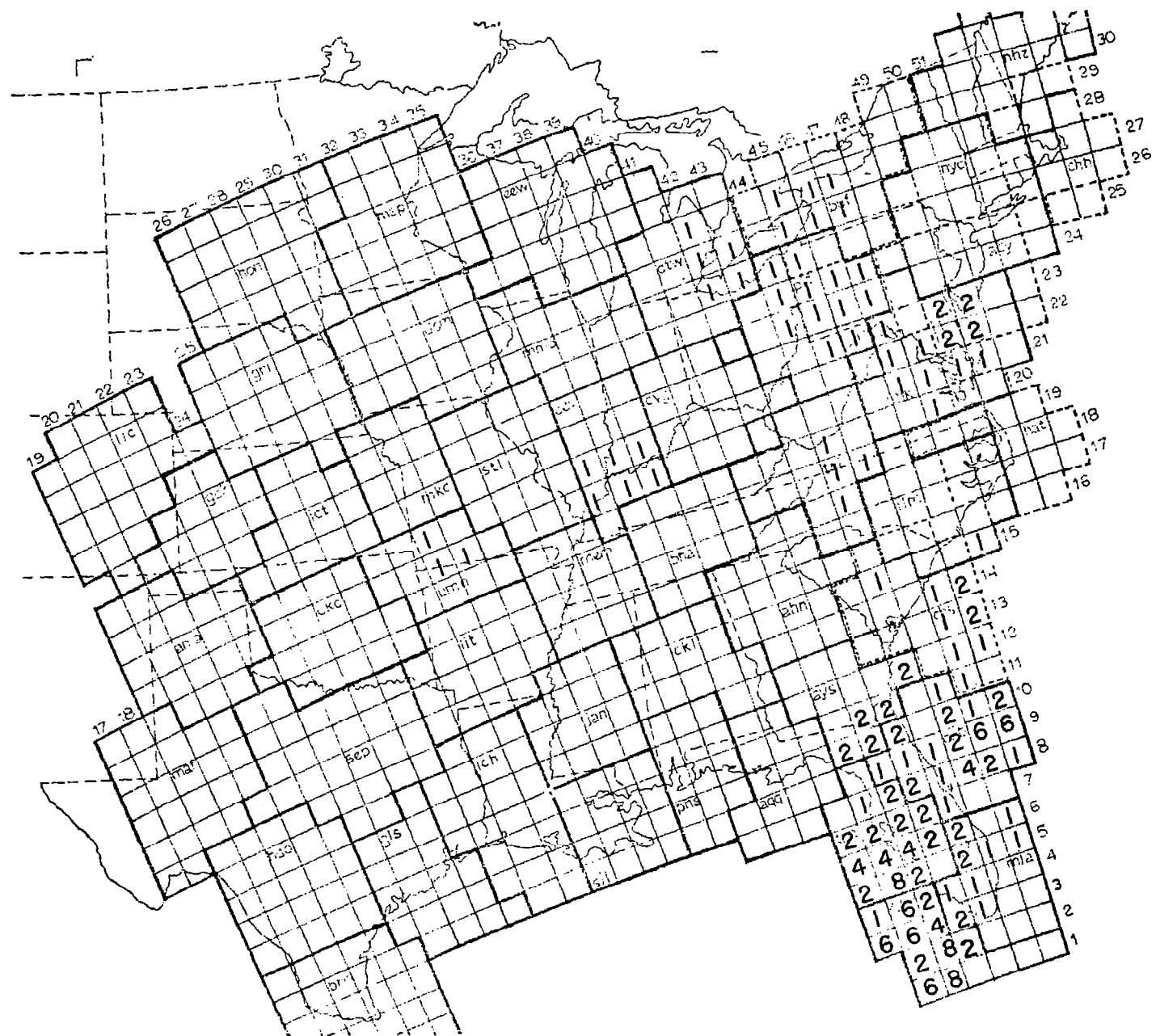
Composite MDR chart for 1400, 1500, and 1600 GMT 6 February 1975.



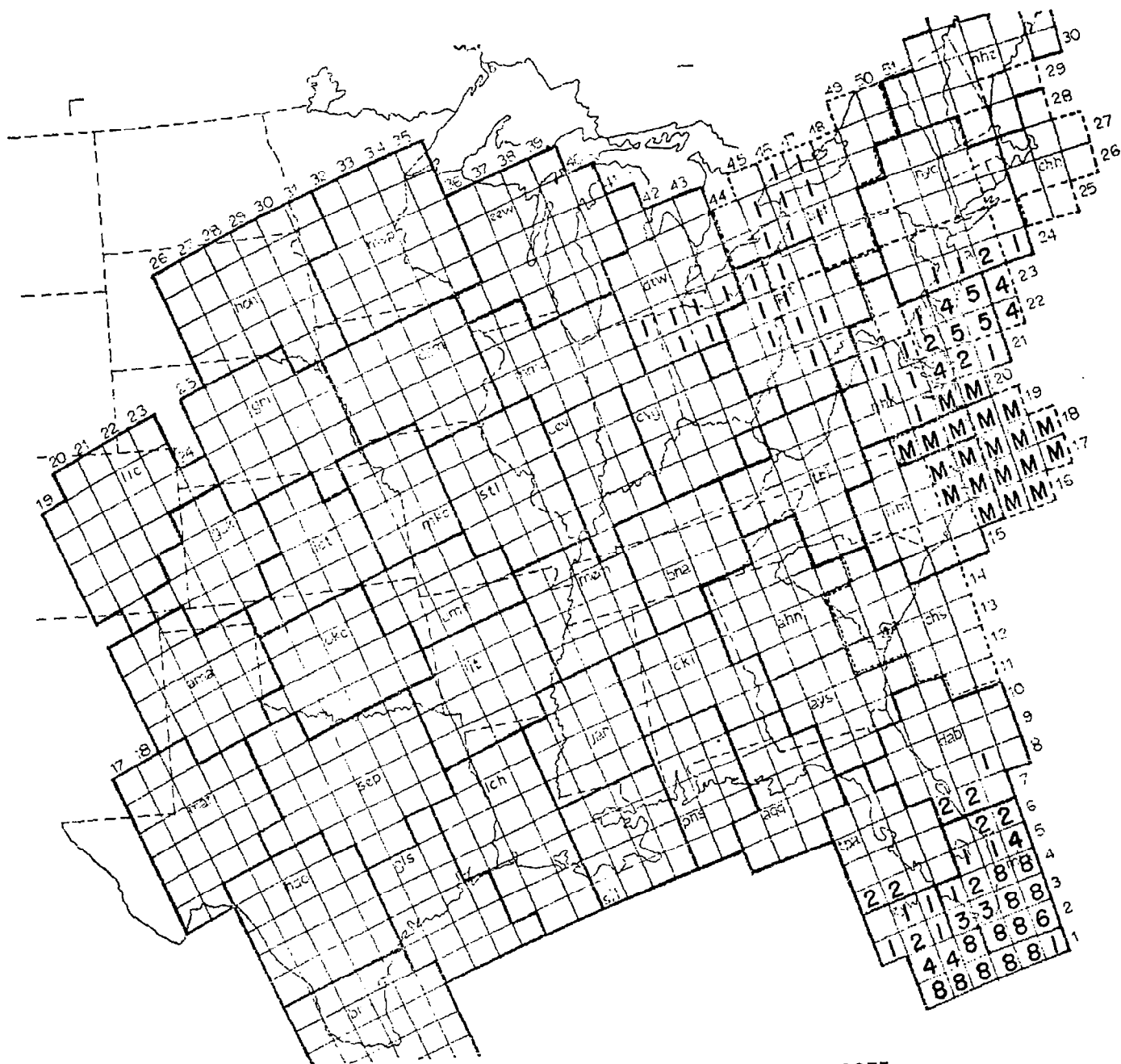
Composite MDR chart for 1700, 1800, and 1900 GMT 6 February 1975.



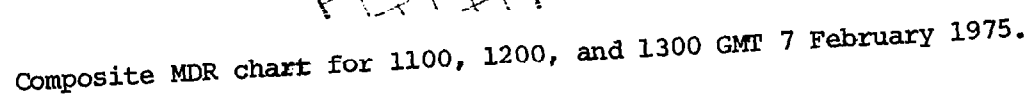
Composite MDR chart for 2000, 2100, and 2200 GMT 6 February 1975.



Composite MDR chart for 2300, 0000, and 0100 GMT 7 February 1975.



Composite MDR chart for 0500, 0600, and 0700 GMT 7 February 1975.



Composite MDR chart for 1100, 1200, and 1300 GMT 7 February 1975.

TECHNICAL REPORT STANDARD TITLE PAGE

1. REPORT NO. NASA CR-3084		2. GOVERNMENT ACCESSION NO.		3. RECIPIENT'S CATALOG NO.	
4. TITLE AND SUBTITLE Studies of Vorticity Imbalance and Stability, Moisture Budget, Atmospheric Energetics, and Gradients of Meteorological Parameters During AVE III				5. REPORT DATE December 1978	
				6. PERFORMING ORGANIZATION CODE	
7. AUTHOR(S) Edited by James R. Scoggins				8. PERFORMING ORGANIZATION REPORT #	
9. PERFORMING ORGANIZATION NAME AND ADDRESS Department of Meteorology Texas A&M University College Station, Texas 77843				10. WORK UNIT, NO. M-277	
				11. CONTRACT OR GRANT NO. NAS8-31773	
12. SPONSORING AGENCY NAME AND ADDRESS National Aeronautics and Space Administration Washington, D. C. 20546				13. TYPE OF REPORT & PERIOD COVERED Contractor	
				14. SPONSORING AGENCY CODE	
15. SUPPLEMENTARY NOTES Prepared under the technical monitorship of the Atmospheric Sciences Division, Space Sciences Laboratory, NASA Marshall Space Flight Center					
16. ABSTRACT This report contains four separate studies using the Atmospheric Variability Experiment (AVE) III data. These studies parallel similar studies for AVE IV, and the results in each study are compared with those obtained for AVE IV. AVE III represents a high wind speed wintertime situation during which relatively little convective activity occurred. By contrast, AVE IV represents a low wind speed springtime situation during which widespread convective activity occurred. Chapter 1 contains information on the AVE III data, synoptic conditions during AVE III, and analytical procedures that are common to all studies. The studies contained in this report include: Chapter 2: Vorticity Imbalance and Stability in AVE III, by William L. Read; Chapter 3: The Moisture Budget in AVE III, by Robert W. Scott; Chapter 4: Atmospheric Energetics During the AVE III Experiment, by Henry E. Fuelberg; Chapter 5: Gradients of Meteorological Parameters During AVE III, by Milton S. McCown. Each study, together with Chapter 1, is complete within itself, including conclusions and references. Each may be read independently of the others.					
17. KEY WORDS Atmospheric Variability Vorticity Atmospheric Energetics Mesoscale Systems				18. DISTRIBUTION STATEMENT Category 47	
19. SECURITY CLASSIF. (of this report) Unclassified		20. SECURITY CLASSIF. (of this page) Unclassified		21. NO. OF PAGES 140	
				22. PRICE \$7.25	

* For sale by the National Technical Information Service, Springfield, Virginia 22161

NASA-Langley, 1978